



THE HONG KONG
POLYTECHNIC UNIVERSITY

香港理工大學

Pao Yue-kong Library

包玉剛圖書館

Copyright Undertaking

This thesis is protected by copyright, with all rights reserved.

By reading and using the thesis, the reader understands and agrees to the following terms:

1. The reader will abide by the rules and legal ordinances governing copyright regarding the use of the thesis.
2. The reader will use the thesis for the purpose of research or private study only and not for distribution or further reproduction or any other purpose.
3. The reader agrees to indemnify and hold the University harmless from and against any loss, damage, cost, liability or expenses arising from copyright infringement or unauthorized usage.

IMPORTANT

If you have reasons to believe that any materials in this thesis are deemed not suitable to be distributed in this form, or a copyright owner having difficulty with the material being included in our database, please contact lbsys@polyu.edu.hk providing details. The Library will look into your claim and consider taking remedial action upon receipt of the written requests.

Pao Yue-kong Library, The Hong Kong Polytechnic University, Hung Hom, Kowloon, Hong Kong

<http://www.lib.polyu.edu.hk>

**SYNTHESIS, CHARACTERIZATION, AND CATALYTIC
PROPERTIES OF SOME TRANSITION METAL-DOPED
NICKEL PHOSPHIDE NANOPARTICLES**

MAN HO WING

PhD

The Hong Kong Polytechnic University

2018

The Hong Kong Polytechnic University
Department of Applied Biology and Chemical Technology

Synthesis, Characterization, and Catalytic Properties of
Some Transition Metal-doped Nickel Phosphide
Nanoparticles

MAN Ho Wing

A Thesis Submitted

in

Partial Fulfillment of the Requirements

for

the Degree of Doctor of Philosophy

April 2018

Certificate of Originality

I hereby declare that this thesis is my own work and that, to the best of my knowledge and belief, it reproduces no material previously published or written, nor material that has been accepted for the award of any other degree or diploma, except where due acknowledgement has been made in the text.

MAN, Ho Wing

April 2018

Abstract

Energy crisis and global warming are two most critical issues emerged in the 21st century. To cope with these problems, development of robust catalysts which can facilitate the production of renewable and sustainable alternative energy source is needed. For instance, water splitting reaction is one of the important reactions for production of hydrogen as a clean renewable energy source. In addition, the efficiency improvements in industrial processes such as ammonia synthesis can reduce the amount of energy required, thus relieves the high global energy demand.

Metal phosphide nanoparticles have recently attracted great attention owing to their potential catalytic activity in organic transformation and energy-related researches. Among them, nickel phosphide is of particular interest because of its versatile catalytic applications with considerable reactivity and high abundance, yet its catalytic performance still lags far behind the noble metal-based catalysts and demands further development. Metal doping is one of the efficient ways to improve the reactivity of catalyst, by altering the local structure and bonding environments of catalyst. However, due to the difficulties involved in synthetic procedures, studies on phosphide with two or more metal atoms are still rare.

In the study, a series of transition metal-doped nickel phosphide nanoparticles were prepared and their catalytic activities in various energy conversion reactions were explored. In Chapter 2, a systematic synthetic procedure of incorporating various transition metal ions, including cobalt, iron, manganese, and molybdenum ions, into the crystal lattice of nickel phosphide nanoparticle was described. Using different characterization techniques, including X-ray diffraction, transmission electron microscopy, X-ray photoelectron spectroscopy, and extended X-ray absorption fine structure, the morphology and crystal structure of prepared transition metal-doped nickel phosphide nanoparticles were studied.

Water splitting is an important reaction to simultaneously generate hydrogen and oxygen gases as alternative energy sources in an environmental-friendly fashion. In Chapter 3, the catalytic performance of the as-synthesized metal-doped nickel phosphide nanoparticles in both electro- and photocatalytic hydrogen evolution reaction (HER) were studied. Among all the metal-doped nickel phosphide nanoparticles investigated, molybdenum-doped nickel phosphide nanoparticle showed the highest reaction rate for both electro- and photocatalytic HER. The electrocatalytic HER performance of molybdenum-doped nickel phosphide nanoparticle in

alkaline medium was comparable to that of platinum, with an overpotential of 0.34 V (versus RHE at 10 mA cm⁻²) and Tafel slope of 163 mV dec⁻¹. In the dye-sensitized photocatalytic HER, molybdenum-doped nickel phosphide nanoparticle achieved a hydrogen production rate of 268 mmol h⁻¹ g⁻¹.

In Chapter 4, a series of as-prepared metal-doped nickel phosphide nanoparticles were investigated as potential electrocatalysts for the other half-reaction of water splitting reaction, oxygen evolution reaction (OER). Different from the HER, iron-doped nickel phosphide nanoparticle was found to be the most active catalyst with an overpotential of 0.33 V and Tafel slope of 39 mV dec⁻¹, which demonstrates a comparable catalytic activity to the benchmark OER electrocatalysts (RuO₂ and IrO₂). In addition, brief kinetic and mechanistic studies on electrochemical OER were conducted. The reaction order of hydroxide ion in electrochemical OER was estimated to be close to unity. The rate determining step in electrochemical OER was determined to be the formation of Ni=O species, as implied by the Tafel slope and reaction order of hydroxide ion.

In addition to the water splitting reaction, the study of using metal-doped nickel phosphide nanoparticles for catalytic ammonia synthesis is presented in Chapter 5. The synthesis of ammonia is an important industrial process,

since ammonia is one of the essential ingredients for making useful chemicals in daily life including polymers and fertilizers. It is the first example of using phosphide-based nanomaterial as catalysts for the synthesis of ammonia. In our studies, iron-doping was shown to play a critical role in enhancing the catalytic activity of nickel phosphide nanoparticles toward ammonia synthesis. The catalytic reaction mechanism for iron-doped nickel phosphide nanoparticle is proposed where iron plays a role of the reaction center while nickel phosphide base assists iron to produce ammonia.

Acknowledgement

I would like to express my gratitude to Professor Shik Chi Edman Tsang and Professor Kwok-Yin Wong, my chief and co-supervisor, for their professional guidance, enthusiastic encouragement, and valuable critique of this research work. I would also like to thank Dr. Lawrence Yoon Suk Lee, for his advice and assistance in keeping my progress on schedule.

My grateful thanks are also extended to Dr. C. S. Tsang for giving me useful advice and preparing photosensitizers, Dr. E. Ha for her guidance throughout the four-year study, Dr. L. S. Hu for sharing his experience especially in XPS, Dr. W. R. Zheng, Mr. Y. Li, and Ms. X. D. Zhang for their help in electrochemical measurements. I would like to show my appreciation to all the past and present people worked together who gave me a memorable life throughout the study. I would also like to thank Dr. Molly M. J. Li and Mr. Simson Wu from The University of Oxford who helped me in conducting EXAFS measurement and catalytic ammonia synthesis.

I would also like to extend my thanks to the technicians in the Department of Applied Biology and Chemical Technology of The Hong Kong Polytechnic University for their help in accessing the resources.

Finally, I would like to thank my family and girlfriend for

their unconditional and endless support and encouragement throughout my study.

Table of Contents

Certificate of Originality	i
Abstract	ii
Acknowledgement	vi
Table of Contents	viii
List of Abbreviations	xiii
List of Figures	xvi
List of Schemes and Tables	xxi
Chapter 1 Introduction	1
1.1 Overview	1
1.2 Hydrogen Evolution Reaction (HER)	4
1.2.1 Electrocatalytic Hydrogen Evolution Reaction	4
1.2.2 Photocatalytic Hydrogen Evolution Reaction	13
1.3 Electrocatalytic Oxygen Evolution Reaction (OER)	19
1.4 Catalytic Ammonia Synthesis	23
1.5 Aims and Objectives	30
Chapter 2 Synthesis and Characterization of Metal-doped Nickel	

Phosphide Nanoparticles	33
2.1 Introduction	33
2.2 Materials and Experimental Procedures.....	35
2.2.1 Materials	35
2.2.2 Synthesis of Pristine and Metal-doped Nickel Phosphide Nanoparticles	35
2.2.2.1 Synthesis of Nickel Phosphide Nanoparticle	35
2.2.2.2 Synthesis of Iron-doped Nickel Phosphide Nanoparticle	36
2.2.2.3 Synthesis of Cobalt-doped Nickel Phosphide Nanoparticle ...	36
2.2.2.4 Synthesis of Manganese-doped Nickel Phosphide Nanoparticle	36
2.2.2.5 Synthesis of Molybdenum-doped Nickel Phosphide Nanoparticle	37
2.2.3 Instrumentation	37
2.2.3.1 Powdered X-Ray Diffraction	37
2.2.3.2 Transmission Electron Microscopy.....	37
2.2.3.3 X-Ray Photoelectron Spectroscopy	38
2.2.3.4 Extended X-Ray Absorption Fine Structure	38
2.3 Synthesis and Characterization of Pristine and Metal-doped Nickel	

Phosphide Nanoparticles	40
2.4 Conclusion	81
Chapter 3 Metal-doped Nickel Phosphide Nanoparticles in	
Electrocatalytic and Photocatalytic Hydrogen Evolution	
Reaction (HER)	83
3.1 Introduction	83
3.2 Materials and Experimental Procedures.....	89
3.2.1 Materials	89
3.2.2 General Procedure for Working Electrode Preparation	89
3.2.3 General Procedure for Electrocatalytic HER.....	89
3.2.4 Synthesis of Ruthenium(II) bipyridine Complexes [Ru(bpy) ₃]X ₂	
(X = Cl, ClO ₄ , or CF ₃ SO ₃).....	90
3.2.5 General Procedure for Photocatalytic HER.....	92
3.2.6 Photostability Test	92
3.3 Results and Discussion.....	94
3.3.1 Electrocatalytic Hydrogen Evolution Reaction	94
3.3.2 Dye-sensitized Photocatalytic Hydrogen Evolution Reaction... 100	
3.3.2.1 Ru(bpy) ₃ ²⁺ -sensitized Photocatalytic Hydrogen Evolution	
Reaction.....	104

3.3.2.2	Eosin Y-sensitized Photocatalytic Hydrogen Evolution Reaction	116
3.4	Conclusion	120
Chapter 4 Metal-doped Nickel Phosphide Nanoparticles in		
	Electrocatalytic Oxygen Evolution Reaction (OER)	121
4.1	Introduction	121
4.2	Material and Experimental Procedures	124
4.2.1	Materials	124
4.2.2	General Procedure for Working Electrode Preparation	124
4.2.3	General Procedure for Electrocatalytic OER	124
4.2.4	General Procedure for Electrochemical Impedance Spectroscopy	125
4.2.5	Stability Test for Electrochemical OER	125
4.3	Results and Discussion	127
4.3.1	Effect of Metal Doping on Electrocatalytic OER	127
4.3.2	Effect of Precursor Ratio	148
4.4	Conclusion	152
Chapter 5 Catalytic Ammonia Synthesis		
5.1	Introduction	155

5.2	Material and Experimental Procedures	159
5.3	Iron-doped Nickel Phosphide Nanoparticle as Catalyst for Ammonia Synthesis	161
5.4	Conclusion	172
Chapter 6	Conclusion.....	173
6.1	Conclusion	173
6.2	Future Research Directions	176
References	179

List of Abbreviations

Ba-NiFeP	Barium-promoted iron-doped nickel phosphide
bpy	2,2'-bipyridine
CB	Conduction band
CBM	Conduction band minimum
DCM	Double crystal monochromator
DFT	Density functional theory
DMF	N, N-dimethylformamide
EDX	Energy-dispersive X-ray spectroscopy
E_F	Fermi level
EIS	Electrochemical impedance spectroscopy
ESI-MS	Electrospray ionization mass spectrometry
E_{VBM}	Energy of valence band maximum
EXAFS	Extended X-ray absorption fine structure
GC	Gas chromatograph
GCE	Glassy carbon electrode
HER	Hydrogen evolution reaction
HR	High-resolution
LC	Ligand-centered transition

LSV	Linear sweep voltammogram
M-H	Metal-hydrogen
MC	<i>d-d</i> transition
MLCT	Metal-to-ligand charge transfer
NiCoP	Cobalt-doped nickel phosphide
NiFeP	Iron-doped nickel phosphide
NiMP	Metal-doped nickel phosphide
NiMnP	Manganese-doped nickel phosphide
NiMoP	Molybdenum-doped nickel phosphide
OER	Oxygen evolution reaction
OTf	Trifluoromethanesulfonate or triflate ion
PGM	Platinum group metal
RHE	Reversible hydrogen electrode
SAED	Selected area electron diffraction
SCE	Saturated calomel electrode
TCD	Thermal conductivity detector
TEOA	Triethanolamine
TEM	Transmission electron microscopy
TOF	Turnover frequency

TON	Turnover number
TOP	Trioctylphosphine
TOPO	Trioctylphosphine oxide
UPS	Ultra-violet photoelectron spectroscopy
UV	Ultra-violet
VB	Valence band
VBM	Valence band maximum
XPS	X-ray photoelectron spectroscopy
XRD	X-ray Diffraction

List of Figures

Figure 1.1. Plot of experimentally-determined exchange current density against ΔG_H obtained from DFT calculation.	7
Figure 1.2. Schematic diagram of dye-sensitized photocatalytic hydrogen evolution.....	15
Figure 1.3. Catalytic cycle of electrocatalytic oxygen evolution.....	20
Figure 1.4. Energy profile of ammonia synthesis through dissociative mechanism.....	24
Figure 2.1. XRD pattern of NiFeP nanoparticle.....	41
Figure 2.2. (a) TEM image, (b) and its size distribution, (c) high resolution TEM image, and (d) electron diffraction pattern of NiFeP nanoparticles....	42
Figure 2.3. EDX spectrum of NiFeP nanoparticles.....	43
Figure 2.4. XPS spectra of NiFeP nanoparticle in (a) Ni 2p, (b) Fe 2p, and (c) P 2p region.	45
Figure 2.5. VB-XPS spectrum of NiFeP nanoparticle.	46
Figure 2.6. XRD pattern of Ni ₂ P nanoparticles.....	47
Figure 2.7. (a) TEM, (b) and its size distribution, (c) HR-TEM image, and (d) electron diffraction pattern of Ni ₂ P nanoparticle.	48
Figure 2.8. EDX spectrum of Ni ₂ P nanoparticles.	49
Figure 2.9. XPS spectra of Ni ₂ P nanoparticle in (a) Ni 2p and (b) P 2p energy levels.	50
Figure 2.10. EXAFS plots of (a) $k^3 \cdot \chi$ of experimental and fitted data and (b) $k^3 \cdot \chi$ phase corrected Fourier transform of experimental and fitted data for NiFeP nanoparticle with Ni K-edge transmission mode.....	53
Figure 2.11. EXAFS plots of (a) $k^3 \cdot \chi$ of experimental and fitted data and (b) $k^3 \cdot \chi$ phase corrected Fourier transform of experimental and fitted data for NiFeP nanoparticle with Fe K-edge transmission mode.....	54
Figure 2.12. EXAFS plots of (a) $k^3 \cdot \chi$ of experimental and fitted data and (b) $k^3 \cdot \chi$ phase corrected Fourier transform of experimental and fitted data for Ni ₂ P nanoparticle with Ni K-edge transmission mode.....	55

Figure 2.13. XRD pattern of nanoparticle formed in the presence of TOP only.	58
Figure 2.14. TEM images and EDX spectra of (a and b) iron oxide and (c and d) nickel oxide.	59
Figure 2.15. XRD pattern of nanoparticle synthesized in the presence of TOPO only.	60
Figure 2.16. TEM image of metal nanoparticle synthesized in the presence of TOPO. Inset shows the size distribution of metal nanoparticle.	61
Figure 2.17. EDX spectrum of nanoparticle synthesized in the presence of TOPO only.	61
Figure 2.18. XRD pattern of NiCoP nanoparticle.	62
Figure 2.19. (a) TEM, (b) and its size distribution, (c) HRTEM image, and (d) electron diffraction pattern of NiCoP nanoparticle.	63
Figure 2.20. EDX spectrum of NiCoP nanoparticle.	64
Figure 2.21. XPS spectra of NiCoP nanoparticle in (a) Ni 2p, (b) Co 2p, and (c) P 2p regions.	66
Figure 2.22. XRD patterns of various NiCoP nanoparticles prepared under different Ni:Co precursor ratios.	68
Figure 2.23. TEM images of different NiCoP nanoparticles (a) NiCoP31, (b) NiCoP21, (c) NiCoP11, and (d) NiCoP12 nanoparticles.	69
Figure 2.24. Relationship of elemental ratio between actual and loading nickel-to-cobalt ratios.	70
Figure 2.25. XRD pattern of NiMnP nanoparticle.	71
Figure 2.26. (a) TEM, (b) and its size distribution, (c) HRTEM image, and (d) electron diffraction pattern of NiMnP nanoparticle.	73
Figure 2.27. EDX spectrum of NiMnP nanoparticle.	73
Figure 2.28. XPS spectra of NiMnP nanoparticle in (a) Ni 2p, (b) Mn 2p, and (c) P 2p energy levels.	75
Figure 2.29. XRD pattern of NiMoP nanoparticle.	77
Figure 2.30. (a) TEM, (b) and its size distribution, (c) HRTEM image, and (d) electron diffraction pattern of NiMoP nanoparticle.	77
Figure 2.31. EDX spectrum of NiMoP nanoparticle.	78

Figure 2.32. XPS spectra of NiMoP nanoparticle in (a) Ni 2p, (b) Mo 3d, and (c) P 2p energy levels.	80
Figure 3.1. Schematic diagram of dye-sensitized photocatalytic generation.	87
Figure 3.2. Linear sweep voltammograms of Ni ₂ P and various NiMP nanoparticles in 1 M KOH.	95
Figure 3.3. Tafel plots of Ni ₂ P and various NiMP nanoparticles.	96
Figure 3.4. Structure of tris(2,2'-bipyridyl)ruthenium(II) perchlorate Ru(bpy) ₃ (ClO ₄) ₂	101
Figure 3.5. Chemical structure of eosin Y.	101
Figure 3.6. Typical UV-visible spectrum of [Ru(bpy) ₃](ClO ₄) ₂	103
Figure 3.7. Typical UV-visible spectrum of eosin Y.	103
Figure 3.8. Comparison of the amount of H ₂ generated in the presence of [Ru(bpy) ₃](ClO ₄) ₂ only, NiFeP nanoparticle only, and both [Ru(bpy) ₃](ClO ₄) ₂ and NiFeP.	105
Figure 3.9. Photocatalytic activity of Ni ₂ P and various NiMP nanoparticles.	107
Figure 3.10. Effect of nickel-to-cobalt precursor ratio on hydrogen production.	108
Figure 3.11. Relation between photocatalytic activity and concentration of Ru(bpy) ₃ ²⁺ using NiFeP nanoparticle as catalyst.	110
Figure 3.12. Photocatalysis in solvent with different water-to-DMF ratio using NiFeP nanoparticle as catalyst.	112
Figure 3.13. Photocatalytic HER performance of NiFeP nanoparticle using Ru(bpy) ₃ X ₂ (X = ClO ₄ ⁻ , CF ₃ SO ₃ ⁻ , Cl ⁻) as photosensitizers in a mixture of H ₂ O–DMF (1:1) using NiFeP nanoparticle as catalyst.	113
Figure 3.14. UV-Visible absorption spectra of Ru(bpy) ₃ X ₂ (X = ClO ₄ ⁻ , OTf ⁻ , Cl ⁻) in H ₂ O–DMF (1:1) solution.	114
Figure 3.15. Stability test on NiMoP nanoparticle in Ru(bpy) ₃ ²⁺ -sensitized photocatalytic HER.	115
Figure 3.16. Photocatalytic HER performance of NiFeP nanoparticle using eosin Y as the photosensitizers in the system.	117
Figure 3.17. Photocatalytic HER performance of Ni ₂ P and different NiMP	

nanoparticles using eosin Y as the photosensitizer in H ₂ O.	119
Figure 4.1. Linear sweep voltammograms of Ni ₂ P and various NiMP nanoparticles in 1 M KOH.	129
Figure 4.2. Tafel plots of Ni ₂ P and various NiMP nanoparticles.	132
Figure 4.3. (a) Cyclic voltammograms of NiFeP nanoparticle in KOH solution with different concentrations and (b) relationship between current density at 0.6 V vs. SCE and concentration of hydroxide ion.	134
Figure 4.4 A plot of activity (current density) of NiMP versus total injected <i>d</i> electrons of transition metal M (Mo= 6, Mn= 7, Fe= 8, Co= 9 and Ni= 10) into the nickel phosphide bands.	140
Figure 4.5 Correlation of the activity (current density) of composite NiMP with M-O bond energy: at (a) low applied potential of 1.5 V and (b) high applied potential of 1.8 V.	143
Figure 4.6. Equivalent circuit model used for iron-doped and pristine nickel phosphide nanoparticles.	145
Figure 4.7. Nyquist plots obtained from electrochemical impedance spectroscopy of iron-doped and pristine nickel phosphide nanoparticles recorded in 1 M KOH solution.....	145
Figure 4.8. (a) Stability test of NiFeP nanoparticle at current density approximately 20 mA cm ⁻² for 10 h and (b) oxygen evolution during stability test.	147
Figure 4.9. (a) Linear sweep voltammograms NiCoP nanoparticles synthesized under different nickel-to-cobalt ratio and (b) the magnified region of oxidation peaks.	150
Figure 4.10. Tafel plots of NiCoP nanoparticles synthesized with various nickel-to-cobalt ratio.	151
Figure 5.1. Potential energy diagram for conversion of adsorbed nitrogen molecule to atomic nitrogen.....	156
Figure 5.2. Schematic diagram of reactor for catalytic ammonia synthesis.	159
Figure 5.3. Comparison of catalytic activity towards ammonia synthesis between NiFeP nanoparticle, non-Fe and Ru-based catalysts, and typical Ru-based catalyst.	163
Figure 5.4. A 4-hour ammonia production by NiFeP nanoparticle without	

addition of promoters. 165

Figure 5.5. Crystal structure of Ni₂P with a space group of P $\bar{6}$ 2m. Blue and red atoms are nickel and phosphorus, respectively. 168

Figure 5.6. Terminal planes of Ni₂P along (0001) lattice plane: (a) Ni₃P₂ and (b) Ni₃P. Blue and red atoms are nickel and phosphorus, respectively. 168

Figure 5.7. Proposed reaction mechanism of catalytic ammonia synthesis. 169

List of Schemes and Tables

TABLES

Table 2.1. EXAFS of NiFeP nanoparticle.	56
Table 2.2. EXAFS of Ni ₂ P nanoparticle.	56
Table 2.3. Normalized elemental ratios of different NiCoP nanoparticles prepared under different nickel-to-cobalt precursor ratios.....	70
Table 2.4. Summary of composition ratios of different transition metal-doped nickel phosphide nanoparticles.	82
Table 3.1. Summary of electrochemical parameters of Ni ₂ P and various NiMP nanoparticles	97
Table 4.1. Summary of electrochemical parameters of Ni ₂ P and various NiMP nanoparticles.	132

SCHEMES

Scheme 1.1. Schematic diagram of HER mechanism in alkaline medium. ..	5
Scheme 4.1. Schematic diagram of proposed mechanism for electrochemical OER.....	136

Chapter 1 Introduction

1.1 Overview

With rapid economic growth, total world energy consumption is growing in a fast rate, from 549 quadrillion BTU in 2012 to 815 quadrillion BTU in 2040.¹ In particular, fossil fuels, including petroleum, coal, and natural gases, are predicted to share 78% of energy consumed in 2040 although technology for renewable energy source is rapidly developing at the same time. Development of sustainable and renewable energy production is one of the most important issues in 21st century. This would not only reduce the needs for fossil fuels, but also relieve the environmental crises caused by the excessive use of fossil fuels. Research efforts have been devoted to developing robust catalysts and improving efficiencies in different energy-related catalytic reactions, such as hydrogen evolution reaction (HER), oxygen evolution reaction (OER), and carbon dioxide reduction, etc. These reactions can produce substitutes of fossil fuels or lead to the development of alternative energy sources. In such a way, demand of fossil fuels and global warming can be relieved and alternative energy sources are provided as a solution to facilitate economic growth.

HER and OER, two reactions of water splitting, are of particular interest

among the energy conversion reactions.² Water splitting involves only water as reactant while producing valuable products, hydrogen and oxygen gases, upon concerted redox reactions. Hydrogen gas produced upon proton reduction can be used as an alternative fuel to fossil fuels which provides energy for daily use. In addition, it is regarded as a zero-emission fuel which releases water as the only product of combustion. Oxygen, as a by-product of water splitting, is evolved by water oxidation to complete the whole cycle of water splitting.

Highly efficient catalysts can also contribute to the cutback of energy crisis by reducing the energy consumption in various industrial processes. Industrial sector consumes a huge amount of energy annually than the other two important sectors (building and transportation) in the society.¹ It comprises numerous industrial processes synthesizing essential chemicals in daily life. Example includes Haber-Bosch process which produces ammonia, the second most produced inorganic compound by industrial chemical plant. In the industrial process, catalyst is often employed to facilitate the reactions under milder conditions (lower pressure and temperature). Improvement in efficiency of catalysts used in industrial processes can greatly reduce energy consumed for maintaining reaction conditions while sustaining the

production rate.

With advances in nanotechnology, nanoscale materials of a large surface area-to-volume ratio and unique catalytic property are developed to fit in not only the production of renewable and sustainable energy sources, but also various industrial processes.³ Development of novel catalysts can reduce the cost for making desired chemicals and lower the required energy for production of target products. HER, OER, and ammonia synthesis are three of the important reactions chosen for further investigation since they produce renewable energy sources and vital chemicals. A brief introduction would be given on these three important reactions in the latter part of this chapter.

1.2 Hydrogen Evolution Reaction (HER)

Hydrogen gas can be generated through electro- and photocatalytic proton reduction of water, steam reforming of methane, or decomposition of formic acid, hydrazine, and ammonia-borane complex.⁴ Among these methods, electro- and photocatalytic HERs from water draw much attention in development of hydrogen production. Water is used to provide protons for reduction to generate hydrogen gas which is the most environmental-friendly substrate among various methods for HER.

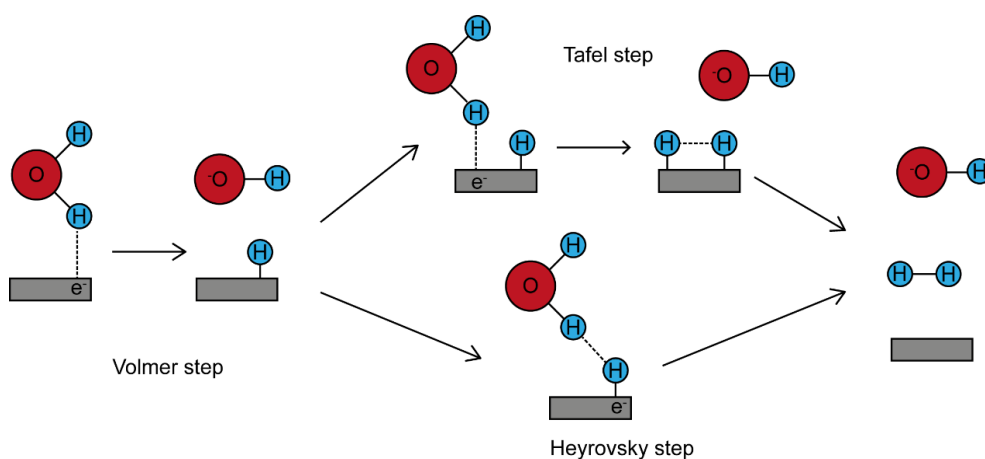
1.2.1 Electrocatalytic Hydrogen Evolution Reaction

Hydrogen generation follows equation (1) in acidic solution or equation (2) in alkaline medium.



Providing adequate amount of energy and electrons, proton or water molecule can be reduced to form gaseous hydrogen via a multiple-step mechanism.⁵ A schematic diagram for HER mechanism is shown in Scheme 1.1. Hydrogen is first adsorbed on active surface with supplying proton or water molecule, and electron. This step is called Volmer step where the hydrogen comes from proton in acidic medium or water molecule in alkaline medium.⁵ The

hydrogen adsorbed on catalyst surface goes through one of the two possible steps, namely Tafel and Heyrovsky step. Tafel step involves the combination of two adsorbed hydrogen atoms and stays the same regardless to pH of the environment. The Heyrovsky step involves the combination of second proton (in acidic medium) or water molecule (in alkaline medium) and electron directly on surface-adsorbed hydrogen.⁵



Scheme 1.1. Schematic diagram of HER mechanism in alkaline medium.

In general, hydrogen can be generated via either Volmer-Tafel or Volmer-Heyrovsky pathway. The hydrogen production mechanism and kinetics can be elucidated experimentally. Tafel plot can be constructed from the polarization plot and the obtained Tafel slope can be used to examine rate determining step for various catalysts used in electrochemical HER. Fletcher has established Tafel slopes from first principle for different reaction

mechanisms which would have different rate determining steps.⁶ The Tafel slope is estimated to be 120, 30, or 40 mV dec⁻¹ when the rate determining step is Volmer, Tafel, or Heyrovsky step, respectively.⁶⁻⁷ Metals in platinum group, such as platinum and palladium, are being widely used as electrocatalysts to generate hydrogen gas from water. Trasatti showed the dependence of exchange current density on the respective metal-hydrogen (M-H) bond strength.⁸ The dependence yields a volcano plot where platinum group metals (PGMs) fall at the summit of volcano. Those metals have moderate M-H bond strength, making them favorable for HER. With this pioneering work, modifications were made by Nørskov and co-workers in which the heat of hydrogen adsorption (ΔH_H) obtained by density functional theory (DFT) was used to correlate the Gibbs free energy of hydrogen adsorption (ΔG_H) with experimental result.⁹ ΔG_H is calculated with its definition:

$$\Delta G_H = \Delta H_H - T\Delta S_H \quad (3)$$

With assumptions made on entropy term, ΔG_H is linearly related to ΔH_H . By that, plot showing relationship between experimentally-determined exchange current density and DFT-calculated ΔG_H is constructed as in Figure 1.1.

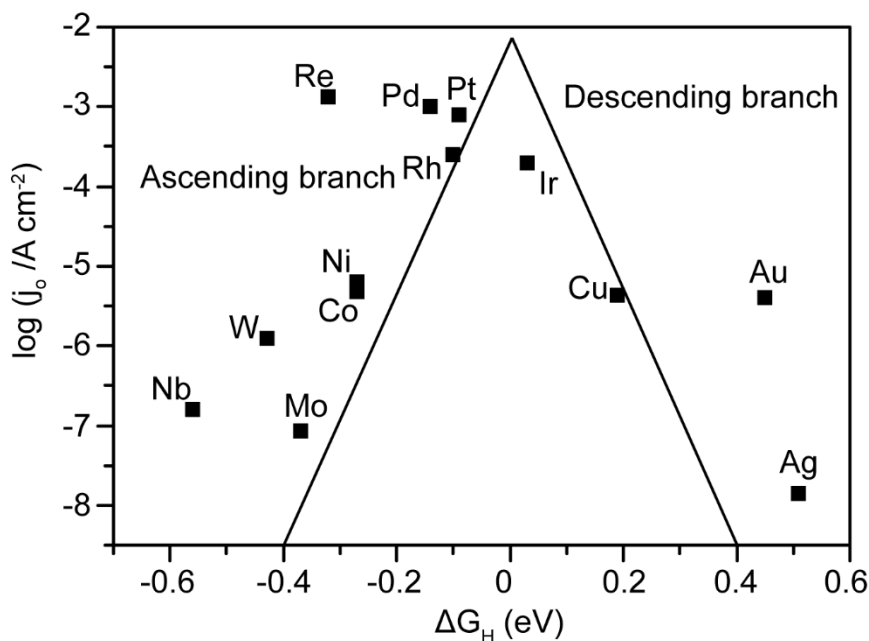


Figure 1.1. Plot of experimentally-determined exchange current density against ΔG_H obtained from DFT calculation. The figure is adapted from reference 9.

A volcano plot, similar to Trasatti one, is obtained where PGMs sit at the summit of volcano. Differences between two volcano plots are arisen due to the considerations of surface oxide or hydroxide formation and inaccuracy in using M-H bond strength to correlate with experimental exchange current density. Nevertheless, the volcano plot agrees with each other and Sabatier principle which states that catalyst and substrate should have intermediate strength of interaction to afford maximum catalytic activity.¹⁰ With moderate ΔH_H , PGMs favor on both formation of adsorbed hydrogen species and desorption of dihydrogen as product. ΔG_H is related to the formation of key intermediate (adsorbed hydrogen) and acts as a descriptor for HER. With the

volcano relationship between hydrogen adsorption energy and catalytic activity, potent catalysts can be designed by adjustment of affinity towards hydrogen adsorption.

Although PGMs are proved to be the best HER electrocatalysts possessing optimal ΔG_H , their use is limited to the laboratory scale because of their high cost and scarcity. Preparation of alloys containing PGMs is a strategy to be used to lower noble metal loading and improve catalytic performance. Nørskov and co-workers use DFT calculation to estimate ΔG_H for different transition metals, noble metals, and their combinations.¹¹ Among combinations, bismuth alloying with platinum (BiPt) shows promising activity with only 0.04 eV difference in DFT-calculated ΔG_H against Pt. In addition to theoretical calculation, BiPt alloy is prepared and tested with its catalytic activity. The alloy offers a higher current density than Pt which improved catalytic activity with minimum use of noble metals.

The use of PGM-containing alloys is still facing the problem of high cost and scarcity. Nevertheless, the researches on noble metals provide a platform for development of non-precious substances as hydrogen-evolving electrocatalysts to substitute PGMs. Efforts are put on more Earth-abundant, non-precious first-row transition metals such as nickel, iron, and cobalt.

Nickel-based substances are conventional electrode materials for alkaline water electrolyzers because of its low cost and corrosion resistance.¹²

Improvement of nickel-based electrocatalysts is made by preparing different nickel-containing alloys. Various nickel-based alloys are prepared by electrodeposition including Ni-Mo, Ni-Zn, Ni-Co, Ni-W, Ni-Fe, and Ni-Cr.

Catalytic activities of those nickel-based alloys are tested towards electrocatalytic HER in electrolyzer.¹³ Among various alloys, Ni-Mo shows a

promising catalytic activity over other alloys. Gray and co-workers

synthesized Ni-Mo nanopowder that further proved excellent activity of Ni-

Mo alloy towards electrochemical HER.¹⁴

With the pioneering investigations of nickel and molybdenum-based

materials as HER electrocatalysts, various materials containing these two

elements are fabricated by combining different anions. One of the most well-

known examples is molybdenum disulfide (MoS_2). MoS_2 is employed as a

catalyst conventionally for hydrodesulfurization.¹⁵⁻¹⁷ Nørskov and

co-workers calculated ΔG_{H} by DFT calculation which showed MoS_2 is a good

catalyst for electrocatalytic HER.¹⁸ The calculation predicted MoS_2 has active

edges (S-Mo-S) which facilitate hydrogen adsorption while the basal plane is

electrochemically inactive. ΔG_{H} of edges of MoS_2 is comparable to that of Pt

which makes MoS₂ a potential candidate to substitute PGMs. The prediction from DFT calculation was verified where the exchange current density is related to edge length of MoS₂.¹⁹ After the verification of catalytic property of MoS₂, various modifications are made to improve its activity towards electrochemical HER. Structural engineering^{7, 20-22} and foreign metal incorporation²³ are two common strategies used for developing more robust MoS₂-based HER electrocatalysts.

Apart from MoS₂, nickel phosphide is another attractive candidate to be a hydrogen-evolving catalyst, which is conventionally employed in hydrodesulfurization processes.²⁴⁻²⁶ Catalytic activities of various nickel-containing compounds are compared by DFT calculations.²⁷ Nickel phosphide with (001) surface is shown to have better activity than platinum, nickel, and analogue of [NiFe] hydrogenase ([Ni(PS3*)(CO)]¹⁻). After this theoretical estimation, Schaak and co-worker synthesized and employed nickel phosphide (Ni₂P) nanoparticles in electrocatalytic HER.²⁸ The reaction is carried out in acidic medium (0.5 M H₂SO₄) and the obtained overpotential to produce 20 mA cm⁻² is 130 mV and Tafel slope is 46 mV dec⁻¹. Although it performs less active than platinum, it shows excellent activity in electrocatalytic HER compared to other non-noble metal-containing

electrocatalysts such as Mo₂C, MoB, and MoS₂. Numerous investigations are carried out after this initial study to improve catalytic performance based on nickel phosphide nanoparticles.²⁹⁻³⁰

There are common strategies used on nickel phosphides which lead to the improvement in their catalytic performance on HER: (1) alteration of nickel-to-phosphorus ratio through the synthesis of different phases including Ni₁₂P₅, Ni₅P₄, Ni₂P, and NiP₂,³¹⁻³³ and (2) incorporation of carbonaceous materials such as carbon nanotube, graphene, and reduced graphene oxide.³⁴⁻³⁶ These methods are in general altering the catalyst dispersion and electrical conductivity, and ultimately lead to the improvement in catalytic activity. In addition to these two methods, synthesis of bimetallic phosphide nanoparticle has demonstrated to enhance catalytic activity over monometallic ones.³⁷ The ΔG_H and current density for HER of metal phosphides are determined theoretically and experimentally, respectively.³⁷ A volcano plot is obtained similar to the case for metals. Cobalt iron phosphide with a formula of Co_{0.5}Fe_{0.5}P is theoretically determined to be the most active HER electrocatalyst among the series of materials being studied, having ΔG_H of 0.004 eV. With this initial study, bimetallic phosphides are prepared and employed as HER electrocatalysts. Typical method for synthesizing

bimetallic phosphide material is by phosphorization of bimetallic precursors such as hydroxide and oxyhydroxide of respective metals. Phosphorization is carried out in furnace in the presence of metal precursors and hypophosphite salt. With elevated temperature, respective bimetallic phosphides are obtained and then employed as HER electrocatalysts. Transition metals are often to be chosen to construct metal part in bimetallic phosphide including Ni-Co,³⁸⁻⁴³ Fe-Co,^{37, 44-45} Ni-Fe,⁴⁶⁻⁴⁹ Fe-Mn,⁵⁰⁻⁵¹ Ni-Mn,⁵² Co-Mn,⁵³⁻⁵⁴ Co-Cu,⁵⁵ Co-Mo,⁵⁶ Fe-Mo,⁵⁷ and Mo-W.⁵⁸ These bimetallic phosphides show enhancement in catalytic activity towards HER. Although the improvement mechanism by using bimetallic phosphide is not yet clearly elucidated, the attempts of combining metals to form phosphides are shown to be one of the promising ways to improve their catalytic property.

1.2.2 Photocatalytic Hydrogen Evolution Reaction

Generation of hydrogen from electrocatalysis requires the input of electrical energy. Without such requirement, photocatalytic hydrogen evolution reaction would be a greener solution than electrocatalytic HER. Photocatalytic HER utilizes virtually unlimited supply of solar energy to produce hydrogen. Initial studies of using solar energy to produce hydrogen involved the use of titanium dioxide (TiO_2) as a material in photoelectrochemical HER.⁵⁹ TiO_2 is a semiconductor which possesses a discrete band gap between its valence band (VB) and conduction band (CB). Upon illumination, electrons in VB are excited to CB if the incoming photons possess energy larger than the band gap. The excited electrons are available to be used in water reduction reaction. However, TiO_2 can only use ultra-violet radiation, which is only 5% in solar spectrum, due to its large band gap energy of 3.2 eV. Despite the large band gap energy which is not favorable for an efficient HER photocatalyst, it opened a new era for the development of semiconductor-based systems for photocatalytic HER.

In order to efficiently carry out photocatalytic HER, semiconductors have to absorb as much radiation to generate photo-excited electrons and possess a proper band position. The first criterion is governed by the band gap

energy of semiconductor. The smaller the band gap energy, semiconductor is allowed to absorb light with less energy and thus broaden the utilization of solar spectrum. The second criterion requires a suitable band position. The conduction band minimum (CBM) has to lie above the thermodynamic proton reduction potential (0 V vs. reversible hydrogen electrode, RHE) while the valence band maximum (VBM) lies below the thermodynamic proton reduction potential. This allows the reduction of proton occur sequentially upon photo-excited electron generation. In order to maximize the usage of solar spectrum, researchers are looking for semiconductors with smaller band gap energy. One of the popular semiconductors possessing smaller band gap is cadmium sulfide (CdS).⁶⁰ CdS possesses a direct band gap with band gap energy of 2.4 eV which can absorb light with wavelength shorter than 520 nm. However, CdS is vulnerable to photo-corrosion, making it less favorable to be used as HER photocatalyst.⁶¹⁻⁶² Nevertheless, these two criteria limit the diversity of available materials for photocatalytic HER.

To broaden the scope for HER photocatalysts, a dye-sensitized system can be constructed. A dye-sensitized system requires a dye molecule with a high molar absorptivity in solar spectrum and a catalyst which is active to produce hydrogen. This does not require the active catalyst to possess

light-absorbing ability and thus allows various potential materials to be used in HER photocatalysis (Figure 1.2). For a complete cycle of sensitized-photocatalytic hydrogen evolution reaction, there are generally four steps: (1) generation of photo-excited electron, (2) injection of photo-excited electron to active catalyst, (3) formation and release of hydrogen molecule, and (4) regeneration of ground state light absorber by corresponding oxidation reaction.⁶³

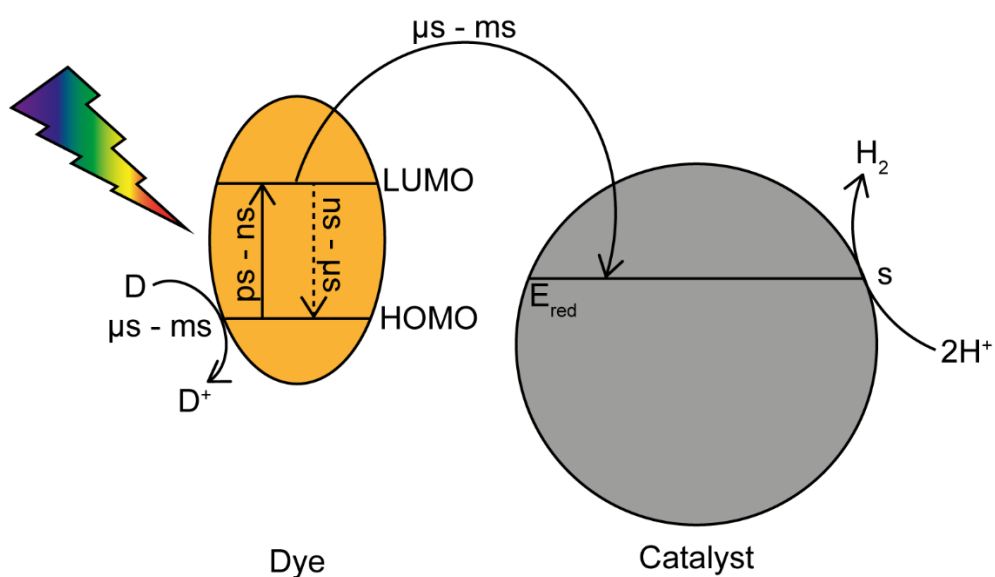


Figure 1.2. Schematic diagram of dye-sensitized photocatalytic hydrogen evolution.

To carry out photocatalytic HER, photo-generated electron is formed upon illumination. The photo-generated electron is transferred from dye molecule to catalyst, and finally to protons on catalyst surface. The lifetime

of elementary steps occurring in photocatalytic system is an indicator for efficiency in carrying out reaction. Although sensitized photocatalytic system comprises of multiple components which is more complicated than conventional semiconductor-based photocatalysis, it provides diversity in combination of different components and mimics natural photosystem II with electron transfer cascade.⁶⁴ In dye-sensitized photocatalytic system, lifetimes of elementary steps increase sequentially, from photo-excitation in picoseconds to nanoseconds time scale, electron transfer from dye molecule to catalyst and regeneration of dye molecule in timescale of microseconds to milliseconds, and hydrogen generation in second timescale.⁶⁴ In contrast, the conventional semiconductor-based photocatalytic systems only involve photo-excitation and proton reduction which have drastic difference in lifetimes. In addition, charges are separated spatially in dye-sensitized systems which inhibit detrimental recombination process. Therefore, despite its complexity, sensitized-photocatalytic system is one of the potential systems for the production of hydrogen using solar energy.

MoS₂ has shown its excellent catalytic activity in electrochemical HER as discussed in the previous section. However, it is not attractive as an photocatalyst due to the indirect band gap of bulk MoS₂.⁶⁵⁻⁶⁷ To make use of

the activity of MoS₂ towards HER, dye-sensitized systems are constructed.^{65,67} Ruthenium complexes and eosin Y are used to sensitize MoS₂ to produce hydrogen in the presence of sacrificial agents. With these studies, the availability of materials for the photocatalytic system is broadened since active HER electrocatalysts without light-absorbing ability can be also employed in photocatalytic HER.

Nickel phosphide is also another active HER electrocatalyst. With numerous studies on nickel phosphides as HER electrocatalysts, researches are moving on to employ nickel phosphides in photocatalytic HER. Nickel phosphide nanoparticle was first employed as co-catalyst with CdS. The performance of nickel phosphide-cadmium sulfide system is excellent to yield a turnover number (TON) of 26,300.⁶⁸ Du and co-workers synthesized the nanocomposite of cadmium sulfide and nickel phosphide by sequential hydrothermal and solvothermal reactions. The nanocomposite is used in photocatalytic HER using sodium sulfide and sodium sulfite solution as sacrificial agent. Hydrogen production rate from the CdS/Ni₂P nanocomposite goes up to 1.2 mmol g⁻¹ h⁻¹.⁶⁹ In addition to CdS, carbon nitride (C₃N₄) is used as photocatalyst together with nickel phosphide which provides an alternative light-absorber apart from typical semiconductors.⁷⁰⁻⁷⁷

Nickel phosphide can be also combined with dye to carry out photocatalytic hydrogen generation. Nickel phosphide and fluorescein sodium are used together to carry out photocatalytic HER with a rate of $10.76 \text{ mmol h}^{-1} \text{ g}^{-1}$.⁷⁸

Nickel phosphide combined with a light absorber has an excellent catalytic activity towards photocatalytic HER.

1.3 Electrocatalytic Oxygen Evolution Reaction (OER)

The splitting of water into hydrogen and oxygen is one of the most promising reactions for development of renewable energy. Water splitting can be separated into two half reactions, hydrogen and oxygen evolution reactions (HER and OER). To complete the water splitting reaction, it is necessary to put effort in development of not only HER catalysts, but also robust oxygen-evolving catalyst so OER catalyst can couple with HER catalyst to carry out the overall water splitting efficiently.



OER involves multiple steps and transfer of four electrons (Figure 1.3). There are numerous proposed mechanisms and the first step of those mechanisms usually involves the formation of metal-hydroxide species (M-OH). The metal-hydroxide species is sequentially oxidized to metal oxide (M-O), which is the key intermediate among all proposed mechanisms. Metal oxide formed on catalyst surface is either converted into peroxide (M-OOH) subsequently and produce oxygen, or leads to oxygen evolution directly by combining two neighbor M-O species.⁷⁹

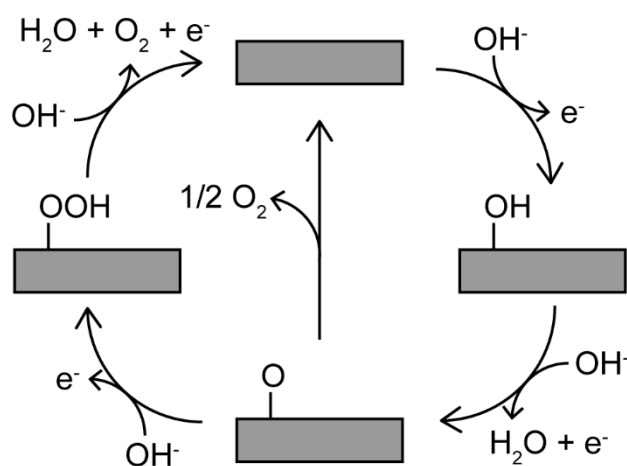


Figure 1.3. Catalytic cycle of electrocatalytic oxygen evolution.

Benchmark OER electrocatalysts are ruthenium dioxide (RuO_2) and iridium dioxide (IrO_2).⁸⁰⁻⁸¹ Using a variety of preparation methods, both IrO_2 and RuO_2 have been prepared to offer a low overpotential at around 300 mV. In addition, they offer good stability in both acidic and alkaline media for electrocatalytic OER. However, RuO_2 and IrO_2 compose of precious metals and are not stable under high current density for practical use. It is necessary to find alternatives for RuO_2 and IrO_2 as OER electrocatalysts.

Numerous materials are employed as OER electrocatalysts including perovskites,⁸²⁻⁸⁴ spinel family,⁸⁵⁻⁸⁸ layered double hydroxides,⁸⁹⁻⁹³ and metal chalcogenides.⁹⁴⁻⁹⁶ In addition to these materials, nickel phosphides have drawn much attention in their bifunctional catalytic activity on both HER and OER. The capability of electrochemical oxygen evolution using nickel phosphides is first demonstrated by Hu and co-workers.⁹⁷ The activity of

nickel phosphide towards OER is originated from *in situ* formation of nickel oxide/hydroxide coating on the surface of nickel phosphide. Nickel oxide formed on catalyst surface is regarded as the key intermediate that facilitates facile OER, as in catalytic cycle previously mentioned. Nickel phosphide nanoparticle requires a low overpotential of 290 mV to produce current density of 10 mA cm^{-2} in 1 M KOH. This catalytic property is better than the benchmark OER electrocatalyst, IrO_2 , which requires an overpotential of 330 mV to produce 10 mA cm^{-2} current density.

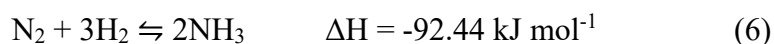
Similar strategies as in HER electrocatalysts are employed on metal phosphides to enhance the OER performance including structural engineering and the incorporation of carbonaceous materials and supports.⁹⁸⁻⁹⁹ Nickel phosphides with different morphologies are prepared, which provide larger surface area and expose more active sites for catalysis. Du and co-workers synthesized nickel phosphide nanowire and compared its OER activity against nanoparticle. The overpotential decreases from around 500 to 400 mV which shows enhanced activity for nanowire.⁹⁸ Apart from structural engineering, incorporation of carbonaceous materials and support is another common strategy to improve OER electrocatalysis. Carbon coating on nickel phosphide nanoplate is prepared from Ni-Ni Prussian blue analogue

precursors. The catalytic activity is enhanced compared to nickel oxide and nickel hydroxide.⁹⁹

Ternary metal phosphides, including Ni-Co,¹⁰⁰⁻¹⁰¹ Co-Fe,¹⁰² and Co-Mn¹⁰³ phosphides, are prepared for improved electrocatalytic OER. They are efficient OER electrocatalysts and require overpotentials ranging from 310 to 370 mV. In combination of excellent HER activity, nickel phosphide is an attractive candidate for alkaline electrolyzer as both cathode and anode materials composed of non-noble metals.

1.4 Catalytic Ammonia Synthesis

Ammonia is one of the most useful chemicals which can be used to produce useful substances such as fertilizers, polymers and explosives. The diverse usage of ammonia makes its production as the second largest industrial process for chemical production where it uses more than 1% of the total energy in the entire world. Ammonia synthesis was started by Fritz Haber who found ammonia synthesis from nitrogen and hydrogen is an exothermic reaction.¹⁰⁴



It is desirable to carry out this exothermic reaction at low temperatures to make the equilibrium shift to favorable side. However, the rate of reaction will be suppressed at low temperatures which makes it unfavorable to an industrial process. Therefore, an optimal environment with low temperature and high pressure is used to obtain the largest yield.¹⁰⁴ With the effort from Carl Bosch for reactor engineering, Haber-Bosch process can successfully produce ammonia in a considerable rate and yield in industrial scale in early 1900s using osmium and uranium-uranium carbide as catalyst. Further improvement was made by Alwin Mittasch by conducting tests for over 2,500 different catalysts. The best catalyst in his study is an iron-based catalyst, with

aluminum oxide and calcium oxide as structural promoters, and potassium as electronic promoter.¹⁰⁴

The mechanism of Haber-Bosch process was proposed to follow a dissociative pathway where it begins with the dissociative adsorption of nitrogen.¹⁰⁵ Hydrogen adsorption and sequential addition of adsorbed hydrogen to nitrogen are carried out and eventually lead to the formation of ammonia. The energy profile of ammonia synthesis is constructed (Figure 1.4). The addition of first hydrogen atom on nitrogen is the rate determining step as it has the largest activation energy. However, it is believed that the rate determining step of overall ammonia synthesis in industrial scale is nitrogen adsorption at elevated temperature since it is a highly exothermic reaction which is not favorable in high temperature.¹⁰⁶

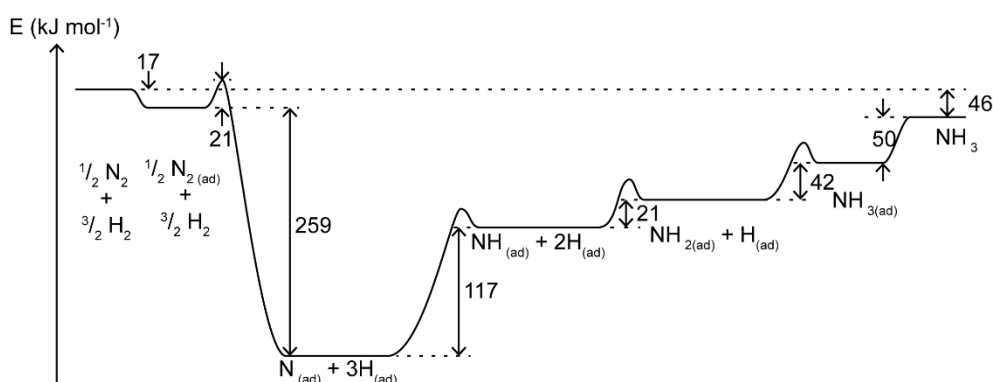


Figure 1.4. Energy profile of ammonia synthesis through dissociative mechanism. The figure is adapted from reference 104 and 106. Numerical values are in unit of kJ mol^{-1} .

Iron-based catalysts are conventionally used in catalytic ammonia synthesis because of its low cost. Numerous studies are carried out to improve their catalytic property.¹⁰⁷⁻¹⁰⁹ In addition to iron, ruthenium and osmium show promising catalytic activities on ammonia synthesis. Fe, Ru, and Os having excellent catalytic activity towards ammonia synthesis can be attributed to number of electrons in *d* orbital.¹¹⁰ All three metals are from the same group (Group VIII) and they have seven electrons in *d* orbital. They provide moderate bond strength for nitrogen chemisorption.¹¹¹ Among the three Group VIII metals, ruthenium drew much attention from researchers to investigate catalysts with improved catalytic activity over traditional fused iron catalysts. Numerous studies have been carried out to prepare ruthenium-based catalysts for ammonia synthesis. Incorporation of second metal in ruthenium is done to prepare a bimetallic system including iron, cobalt, nickel and molybdenum.¹¹² The study shows that Ru-Co system offers the best catalytic activity towards ammonia synthesis so as to decrease the loading of ruthenium.

Promoter is another component in catalytic ammonia synthesis which is used to assist catalytic reaction in high pressure and temperature conditions. There are generally two types of promoters usually being employed in

catalytic ammonia synthesis, structural and electronic promoters. Structural promoter is used to stabilize catalyst and prevent sintering of catalyst possessing large surface area. Typical examples of structural promoters are aluminum oxide and calcium oxide.¹¹³ Structural promoter acts as a physical barrier to maintain the small size of catalyst and has no direct effect on the rate of catalysis. This will help preserving the structures of catalyst under high temperature and pressure in practical Haber-Bosch process. In contrast, electronic promoter can enhance catalytic activity in ammonia synthesis. Alkali metals, including potassium and cesium, are commonly used as electronic promoters.¹¹⁴⁻¹¹⁵ Catalyst surface modified by alkali metal interacts with adsorbing nitrogen molecules. Electrostatic force between the active site and adsorbing nitrogen molecule drives the formation of adsorption of nitrogen atoms on catalyst surface. This facilitates dissociation of nitrogen into adsorbed nitrogen atoms by stabilizing transition state of nitrogen dissociation (lower activation energy).¹¹⁶

Although ruthenium-based catalysts for ammonia synthesis attract much attention from researchers as alternatives of iron-based catalysts, they are far from commercialization in industry because of the scarcity of ruthenium. Therefore, it is desirable to develop a catalyst composed of non-precious,

Earth-abundant elements. With the demand for novel catalysts, ternary nitrides are demonstrated to be a potential candidate for catalytic ammonia synthesis.¹¹⁷ Various ternary nitrides are synthesized and tested for their catalytic activity towards ammonia synthesis including $\text{Fe}_3\text{Mo}_3\text{N}$, $\text{Co}_3\text{Mo}_3\text{N}$, and $\text{Ni}_2\text{Mo}_3\text{N}$. These ternary nitrides show catalytic activity towards ammonia synthesis with applied pressure and elevated temperature. Among the three different ternary nitrides, $\text{Co}_3\text{Mo}_3\text{N}$ shows the highest rate of ammonia production ($120 \text{ mL h}^{-1} \text{ g}^{-1}$). Further improvement of $\text{Co}_3\text{Mo}_3\text{N}$ is achieved by the addition of electronic promoter (Cs) and the rate of ammonia production is increased nearly by 10-fold, from 120 to $1,040 \text{ mL h}^{-1} \text{ g}^{-1}$. In addition, this ternary nitride affords a better catalytic activity over commercial iron-based catalyst which shows the possibility of substituting iron-based catalyst by ternary nitride family in industrial production of ammonia.

DFT calculation is applied on ammonia synthesis similar to hydrogen evolution reaction.¹¹⁷⁻¹¹⁸ A volcano plot is obtained with turnover frequency (TOF) against adsorption energy of nitrogen. Since the rate determining step in ammonia synthesis is believed to be nitrogen adsorption, ruthenium, osmium, and iron are shown to be the best three metals for nitrogen adsorption where they are at the summit of volcano plot. Meanwhile, nickel and cobalt

have a higher adsorption energy of nitrogen than ruthenium which have a weak interaction with nitrogen. In contrast, molybdenum has too strong binding with nitrogen, making it unfavorable to be a catalyst for ammonia synthesis. A combination of strongly and weakly nitrogen-binding metals is used to prepare their respective nitride for moderate binding of nitrogen. DFT calculation shows the combination of cobalt and molybdenum has a better nitrogen-adsorbing energy than ruthenium (closer to the summit of volcano plot).¹¹⁸ The theoretical estimation of catalytic activity from adsorption energy of nitrogen fits with experimental results from various groups.¹¹⁷⁻¹¹⁹ Apart from $\text{Co}_3\text{Mo}_3\text{N}$, Co-Mo alloy supported by CeO_2 is fabricated by co-reduction of cobalt and molybdenum chloride by sodium naphthalenide and used for ammonia synthesis.¹²⁰ Co-Mo alloy has a comparable activity to $\text{Co}_3\text{Mo}_3\text{N}$ and an excellent stability for 120 h reaction. With high surface area provided by small Co-Mo nanoparticle, it affords a much higher activity per surface area. Apart from combination of cobalt and molybdenum, cobalt and iron are combined and employed as an ammonia-producing catalyst.¹²¹ The eluent gas contains 6.04 mol% of ammonia which is produced by Co-Fe catalyst promoted by potassium and supported by carbon at 470 °C and 90 bar. These combinations share the same idea that employ strongly and weakly

nitrogen-binding metals together to produce ammonia. Alloying components possessing strongly, and weakly nitrogen-binding ability can be combined to fabricate new materials for not only ammonia synthesis, but also other types of catalytic reactions having the formation of key intermediate as rate determining step.

1.5 Aims and Objectives

Nickel phosphide nanoparticles possess metallic property which resembles metal nanoparticles as well as excellent physical property as ceramics. Through the incorporation of guest metal, bimetallic phosphide nanoparticles can be prepared, and their catalytic activity might be changed through ensemble effect and/or electronic effect.

Hydrogen evolution reaction can be carried out using bimetallic phosphides electrocatalytically and photocatalytically. With the addition of guest metals, hydrogen binding affinity can be altered which may affect the rate of reaction. In addition to hydrogen evolution reaction, oxygen evolution reaction, as another half reaction of water splitting, is going to be studied using bimetallic phosphides as electrocatalysts. With capability to conduct hydrogen and oxygen evolution reaction, an overall water splitting might be achieved.

In addition to application in renewable energy source-related catalysis, bimetallic phosphides, as an analogue of ternary nitrides, are employed as a catalyst for ammonia synthesis which can be a novel class of ammonia-producing catalysts. Alternative catalyst composed of non-noble, earth-abundant elements is desirable to be used in industrial ammonia synthesis.

In this project, modification of nickel phosphide is made by incorporation of foreign transition metals, including iron, cobalt, manganese and molybdenum, to form different transition metal-doped nickel phosphide nanoparticles. Through the modification of foreign metals, the surface and electronic structure of nickel phosphide will be altered. With the preparation of different transition metal-doped nickel phosphide nanoparticles, catalytic activity on different reactions will be analyzed, including (1) electro- and photocatalytic hydrogen evolution reactions, (2) electrocatalytic oxygen evolution reaction, and (3) ammonia synthesis.

Chapter 2 Synthesis and Characterization of Metal-doped

Nickel Phosphide Nanoparticles

2.1 Introduction

Transition metal phosphides are generally synthesized by thermal decomposition of phosphorus-containing substances. Examples of typical phosphorus-containing substances for phosphide formation includes elemental phosphorus, phosphorus-containing inorganic salt hypophosphite salt (H_2PO_2^-), and organophosphorus compounds such as trioctylphosphine (TOP).¹²²⁻¹²³ With elevated temperature, decomposition of phosphorus source is resulted, and phosphine gas is *in situ* released and reacts with metal precursors where metal phosphide is subsequently formed. With these facile and simple bottom-up synthetic methods, nickel phosphides, with different phases and morphologies, have been prepared with different nickel precursors and subjected to different applications.

Here, metal-doped nickel phosphide nanoparticles are prepared by thermal decomposition of trioctylphosphine (TOP). The employment of TOP in the synthesis of metal phosphide nanoparticles provides a facile and diverse way to convert various kind of precursors to the respective phosphide nanoparticles.¹²⁴⁻¹²⁵ In addition, the role of TOP and its respective oxide,

trioctylphosphine oxide (TOPO) was elucidated by carrying out systematic analysis.

2.2 Materials and Experimental Procedures

2.2.1 Materials

Nickel(II) acetate tetrahydrate was purchased from Panreac. Iron(II) acetate ($\geq 99.99\%$), manganese(III) acetate dihydrate (97%), cobalt(II) acetate (99.995%), oleylamine (technical grade, 70%), trioctylphosphine (technical grade, 90%), and trioctylphosphine oxide (technical grade, 90%) were purchased from Aldrich. Molybdenum(II) acetate dimer (99%) was purchased from Strem. All chemicals were used as received.

2.2.2 Synthesis of Pristine and Metal-doped Nickel Phosphide Nanoparticles

2.2.2.1 Synthesis of Nickel Phosphide Nanoparticle

Typically, 1 mmol nickel(II) acetate tetrahydrate was used as metal precursor and mixed in 5 mL of oleylamine in a 100 mL three-necked round-bottomed flask. The mixture was put under vacuum to remove adventitious oxygen and moisture. 11.2 mmol of trioctylphosphine (TOP) and equimolar of trioctylphosphine oxide (TOPO) were added to the flask sequentially. The reaction mixture was heated at 300 °C for 2 h under N₂ protection. After 2 h reaction, the reaction mixture was cooled down naturally by removal of heat

source. 30 mL absolute ethanol was added, and the precipitate was collected by centrifugation at 9000 rpm for 5 min. Supernatant was discarded and precipitate was purified by redispersion/precipitation process using chloroform and ethanol. The process was repeated for three times and purified product was dried and kept under vacuum.

2.2.2.2 Synthesis of Iron-doped Nickel Phosphide Nanoparticle

Iron-doped nickel phosphide nanoparticle was synthesized with similar procedures as nickel phosphide nanoparticle. 0.5 mmol of nickel(II) acetate tetrahydrate and 0.5 mmol of iron(II) acetate were used to keep the metal ion concentration constant.

2.2.2.3 Synthesis of Cobalt-doped Nickel Phosphide Nanoparticle

Nickel phosphide nanoparticle was synthesized with similar procedures as iron-doped nickel phosphide nanoparticle. 0.5 mmol cobalt(II) acetate was used as metal precursor instead of iron(II) acetate.

2.2.2.4 Synthesis of Manganese-doped Nickel Phosphide Nanoparticle

Nickel phosphide nanoparticle was synthesized with similar procedures

as iron-doped nickel phosphide nanoparticle. 0.5 mmol manganese(III) acetate dihydrate was used as metal precursor instead of iron(II) acetate.

2.2.2.5 Synthesis of Molybdenum-doped Nickel Phosphide Nanoparticle

Nickel phosphide nanoparticle was synthesized with similar procedures as iron-doped nickel phosphide nanoparticle. 0.25 mmol molybdenum(II) acetate dimer was used as metal precursor instead of iron(II) acetate.

2.2.3 Instrumentation

2.2.3.1 Powdered X-Ray Diffraction

Powdered X-Ray diffraction pattern was obtained using Rigaku SmartLab with scan rate of 1° min^{-1} . Powdered sample was placed on a silicon wafer and pressed using a glass slide. Diffraction pattern from $2\theta = 35^\circ$ to 60° was obtained for pristine and various metal-doped nickel phosphide nanoparticles.

2.2.3.2 Transmission Electron Microscopy

As-prepared powder samples were dispersed and sonicated in chloroform to obtain well-dispersed suspension. 20-40 μL of suspension was

added on a 400-mesh copper grid with holey carbon coating and dried naturally. Images from transmission electron microscopy was obtained using a scanning transmission electron microscope (JOEL JEM-2100F). Selected area electron diffraction (SAED) and energy-dispersive X-ray spectroscopy (EDX) were carried out in tandem in transmission electron microscopy.

2.2.3.3 X-Ray Photoelectron Spectroscopy

Approximately 20 mg of powder sample was used in analysis. X-Ray photoelectron spectra of pristine and various metal-doped nickel phosphide nanoparticles were obtained using X-Ray photoelectron spectrophotometer (ESCALAB 250 Xi). Calibration was done using binding energy of C 1s energy level at 284.8 eV as reference.

2.2.3.4 Extended X-Ray Absorption Fine Structure

Local structures surrounding Ni and Fe atoms were probed using extended X-ray absorption fine structure (EXAFS) technique at beamline BL17C of Taiwan Light Source at National Synchrotron Radiation Research Center (NSRRC) in Taiwan. A Si(111) Double Crystal Monochromator

(DCM) was used to scan the photon energy. The energy resolution ($\Delta E/E$) for the incident X-ray photons was estimated to be 2×10^{-4} . Transmission mode was adopted for Ni K-edge and Fe K-edge EXAFS measurements. To ascertain the reproducibility of the experimental data, at least two scan sets were collected and compared for each sample. The EXAFS data analysis was performed using IFEFFIT 1 with Horae packages 2 (Athena and Artemis). The spectra were calibrated with Ni and Fe metal foils as the references to avoid energy shifts of the samples. The amplitude reduction factors were obtained from EXAFS data analysis of the references, which were used as the fixed input parameters in the data fitting to allow the refinement in the coordination number of the absorption element. In this work, the first shell data analyses under the assumption of single scattering were performed with the errors estimated by R-factor.

2.3 Synthesis and Characterization of Pristine and Metal-doped Nickel Phosphide Nanoparticles

Iron-doped nickel phosphide (NiFeP) nanoparticle was first synthesized to investigate the feasibility of metal doping in nickel phosphide crystal lattice. Nickel and iron metal salts were mixed in the presence of oleylamine, trioctylphosphine (TOP), and trioctylphosphine oxide (TOPO).

X-Ray diffraction (XRD) pattern of NiFeP nanoparticles is shown below (Figure 2.1). The as-synthesized NiFeP nanoparticle has diffraction pattern consisting of four peaks at $2\theta = 40.7^\circ$, 44.7° , 47.4° , and 54.4° . This diffraction pattern resembles Ni₂P hexagonal crystal structure (PDF#-65-1989). The former three peaks from XRD pattern of NiFeP at $2\theta = 40.7^\circ$, 44.7° , and 47.4° are corresponding to (111), (201), and (210) lattice planes, respectively. Meanwhile, the two peaks at 54.2° and 55° in Ni₂P reference pattern, corresponding to (300) and (211) lattice planes, respectively, merge together to have a broad peak at 54.4° in XRD pattern of NiFeP nanoparticle due to small crystalline size in nanoparticles.

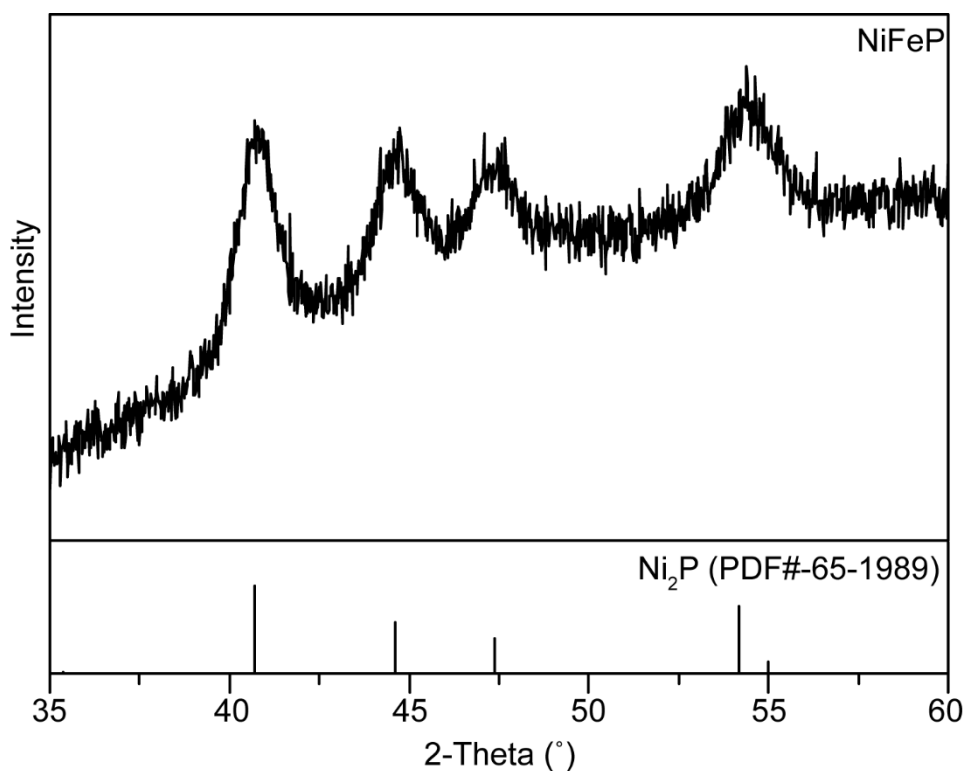


Figure 2.1. XRD pattern of NiFeP nanoparticle.

Detailed morphology and elemental composition of NiFeP nanoparticle are investigated by transmission electron microscopy (TEM) and energy dispersive X-ray spectroscopy (EDX) equipped in TEM. The TEM image shows the as-synthesized NiFeP nanoparticle is monodispersed and spherical with an average diameter of 7.5 ± 0.9 nm (Figure 2.2 (a) and (b)). The small size of nanoparticle is coherent with the large full width at half maximum (broad peaks) and small crystalline size in XRD pattern. TEM image taken under high resolution is shown in Figure 2.2 (c). The predominant (111) lattice fringe shows a d -spacing of 0.22 nm. The selected area electron

diffraction (SAED) pattern shows the rings of diffraction (Figure 2.2 (d)), where the innermost ring is indexed as (111) lattice plane and the outermost ring corresponds to (300) lattice plane. The measurement of d -spacing and electron diffraction pattern is in good agreements with XRD pattern mentioned previously. The elemental composition is determined by EDX (Figure 2.3). The normalized ratio of elements in NiFeP nanoparticle (nickel-to-iron-to-phosphorus) is 1:0.1:0.7. An overall 6% of iron is successfully doped into the nickel phosphide crystal lattice.

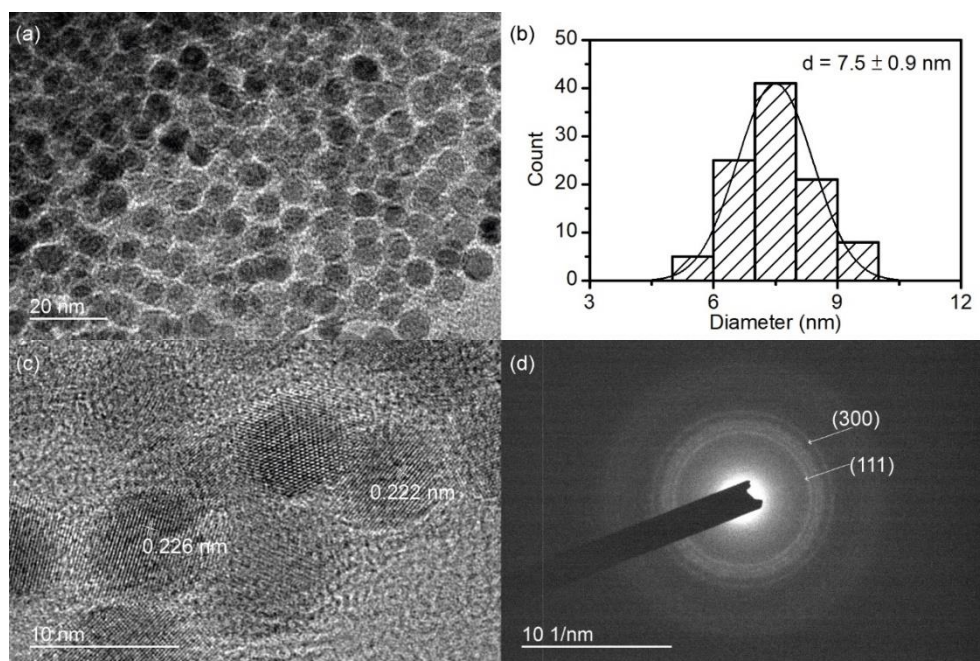


Figure 2.2. (a) TEM image, (b) and its size distribution, (c) high resolution TEM image, and (d) electron diffraction pattern of NiFeP nanoparticles.

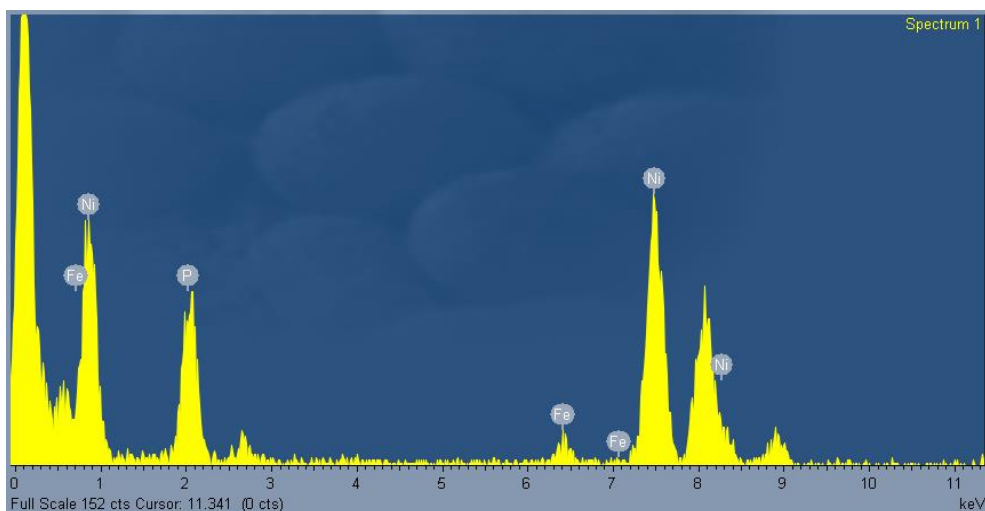


Figure 2.3. EDX spectrum of NiFeP nanoparticles.

X-ray photoelectron spectroscopy (XPS) is used to determine the oxidation state and bonding environment of various elements in NiFeP nanoparticle (Figure 2.4). XPS spectra of Ni 2p and P 2p regions have the peaks similar to typical nickel phosphides (Figure 2.4 (a) and (c)).³³ Peaks at 853.0 eV correspond to nickel in nickel-phosphorus bond in Ni 2p_{3/2} level. The binding energy is close to zero-valent nickel (852.8 eV)¹²⁶ which indicates nickel in nickel-phosphorus bond only bear a small positive charge (Ni^{δ+}).³¹ The peaks at 856.1 and 861.5 eV are assigned to the oxidized nickel species (NiO) and its satellite peak in Ni 2p_{3/2} level, respectively. Similarly, the peaks at 869.9, 874.1, and 880.1 eV correspond to nickel in nickel-phosphorus bond, oxidized Ni species, and its satellite peak in the Ni 2p_{1/2} energy level. In XPS spectrum of P 2p region, the peak at 129.4 eV originates from the phosphorus in nickel-phosphorus bond, while the peak at 133.1 eV

corresponds to the surface oxidized phosphorus species such as phosphate. The binding energy of phosphorus in phosphide slightly deviates from elemental phosphorus (130.2 eV) which shows phosphorus in nickel-phosphorus bond bears a small negative charge ($P^{\delta-}$).¹²⁷⁻¹²⁸ In addition, the embedded peak at 130.4 eV can be assigned to the phosphorus in iron phosphide domain.¹²⁹ For Fe 2p XPS spectrum, the peaks at 711.8 and 713.5 eV correspond to the surface oxidized iron in iron oxide and phosphate in Fe $2p_{3/2}$ energy level, respectively, meanwhile the peaks at 723.5 and 727.9 eV are the counterpart peaks in Fe $2p_{1/2}$ energy level.¹³⁰⁻¹³¹ The peaks at 706.8 and 719.5 eV can be assigned to the iron in iron phosphide in Fe $2p_{3/2}$ and $2p_{1/2}$ energy level, respectively (Figure 2.4 (b)).

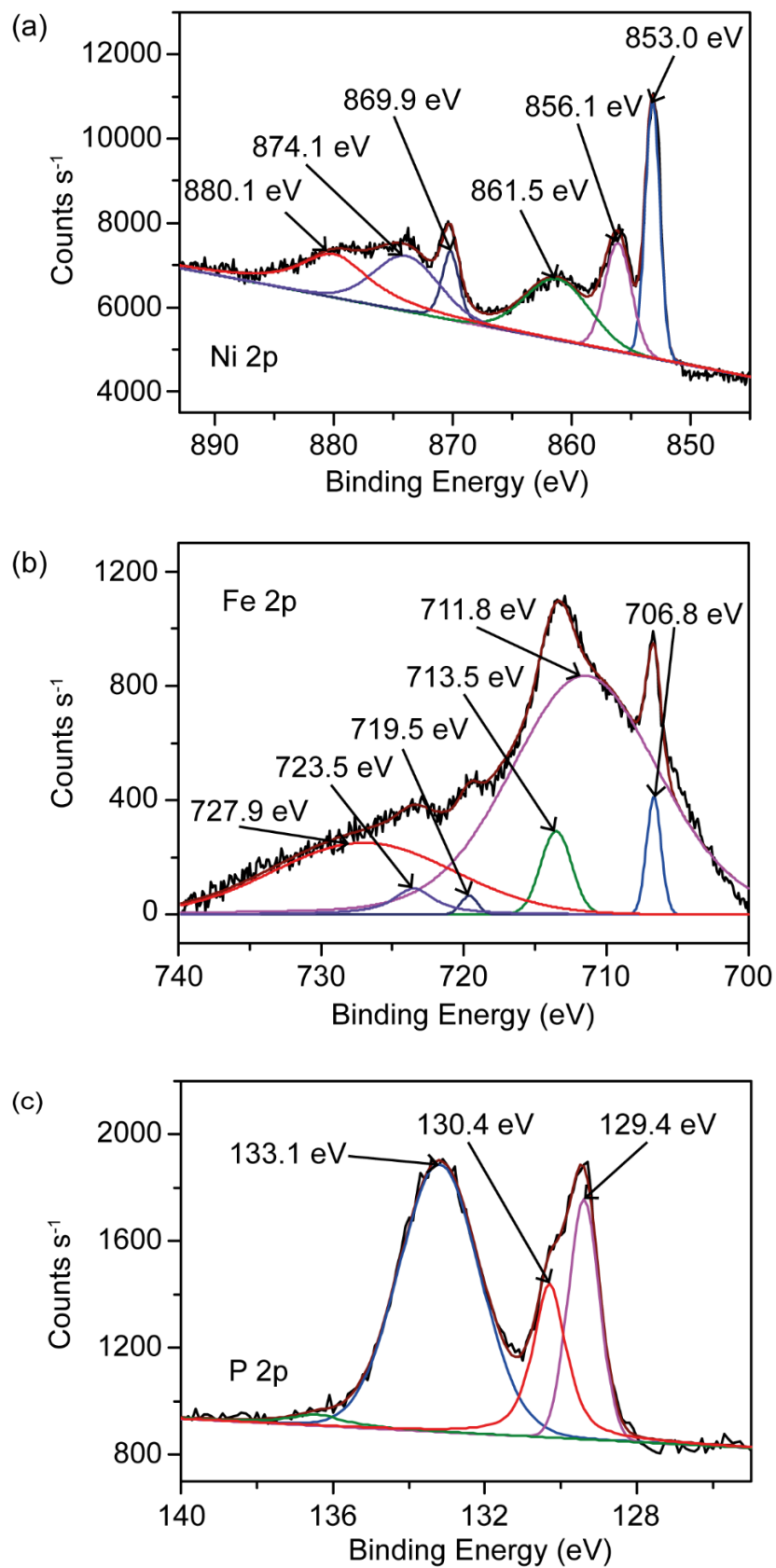


Figure 2.4. XPS spectra of NiFeP nanoparticle in (a) Ni 2p, (b) Fe 2p, and (c) P 2p region.

Valence band X-ray photoelectron spectroscopy (VB-XPS) is carried out for NiFeP nanoparticle to determine the energy of valence band maximum against Fermi level (Figure 2.5). The energy difference between Fermi level (E_F) and valence band maximum (E_{VBM}) can be found from the interception on abscissa by extrapolating the right-side slope of the peak. The energy difference is estimated as -0.37 eV that implies a higher energy of valence band maximum (VBM) than Fermi level and proves NiFeP nanoparticle possesses a metallic property.

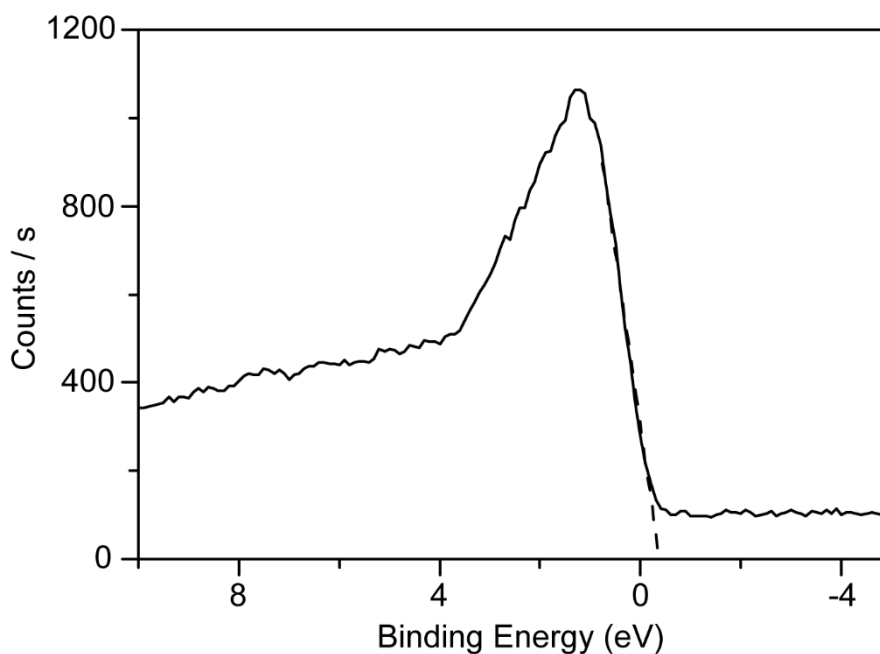


Figure 2.5. VB-XPS spectrum of NiFeP nanoparticle.

To investigate the effect of presence of iron ion in synthesis, a control experiment is carried out by conducting the same experimental procedures without iron. The XRD pattern of nickel phosphide nanoparticle is similar to that of NiFeP nanoparticles both of which match well with Ni₂P reference pattern (PDF#-65-1989) (Figure 2.6).

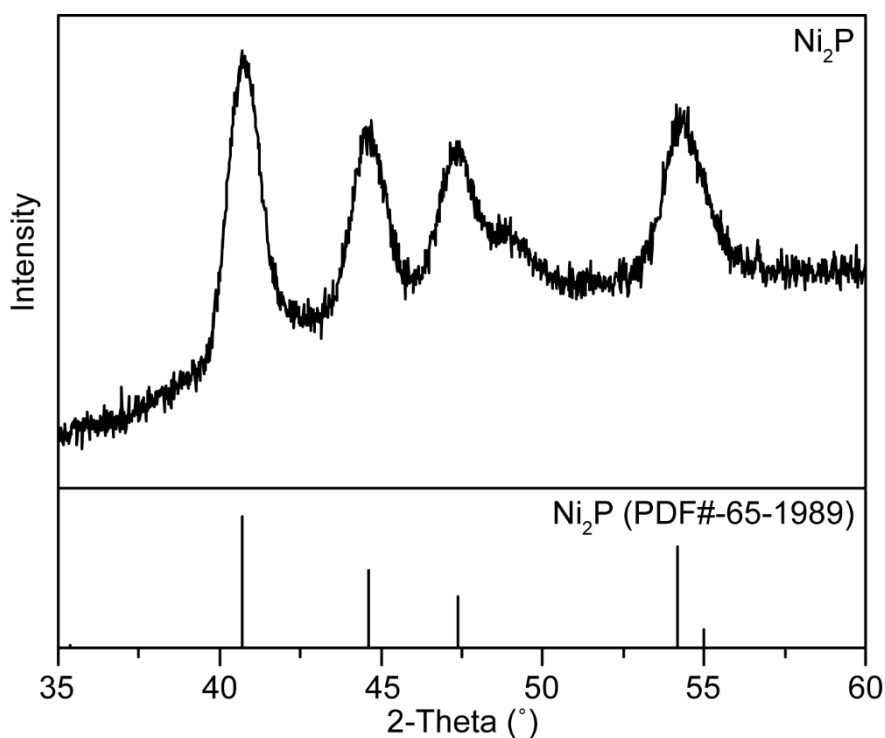


Figure 2.6. XRD pattern of Ni₂P nanoparticles.

TEM images show the nickel phosphide nanoparticle formed has spherical shape with an average diameter of 7.3 ± 1.2 nm which is similar to NiFeP nanoparticles (Figure 2.7 (a) and (b)). High-resolution TEM (HR-TEM) image shows the fringes with *d*-spacing of 0.2 and 0.23 nm which correspond

to (111) and (201) lattice planes, respectively (Figure 2.7 (c)). Electron diffraction pattern shows the rings of diffraction of (111) and (300) planes as the innermost and outermost rings, respectively (Figure 2.7(d)). The elemental composition by EDX indicated the nickel-to-phosphorus ratio is 2:1 which confirms the formation of Ni₂P crystal phase (Figure 2.8).

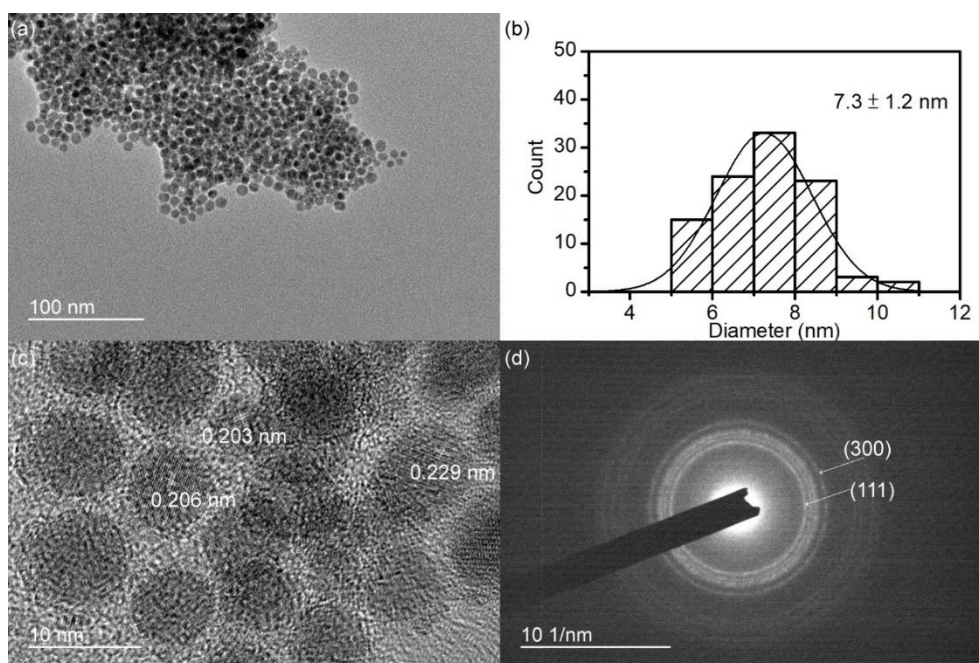


Figure 2.7. (a) TEM, (b) and its size distribution, (c) HR-TEM images, and (d) electron diffraction pattern of Ni₂P nanoparticles.

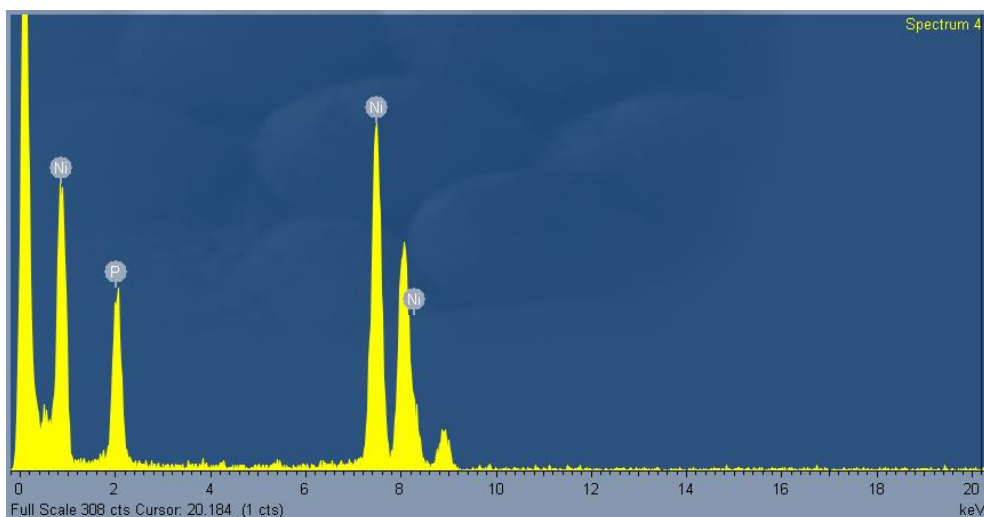


Figure 2.8. EDX spectrum of Ni₂P nanoparticles.

XPS spectra of Ni 2p and P 2p regions have similar peaks as typical nickel phosphide (Figure 2.9 (a) and (b)).³³ The peak at 852.7 eV correspond to 2p_{3/2} level of nickel in nickel-phosphorus bond. The peaks at 856.1 and 861.5 eV correspond to 2p_{3/2} level of oxidized Ni species (NiO) and its satellite peak, respectively. Similarly, the peaks at 869.9, 874.1, and 880.1 eV correspond to nickel in nickel-phosphorus bond, oxidized Ni species, and its satellite in the Ni 2p_{1/2} energy level, respectively. In XPS spectrum of P 2p region, the peak at 129.4 eV originates from the phosphorus in nickel-phosphide bond, while the peak at 133.1 eV corresponds to surface oxidized P species.

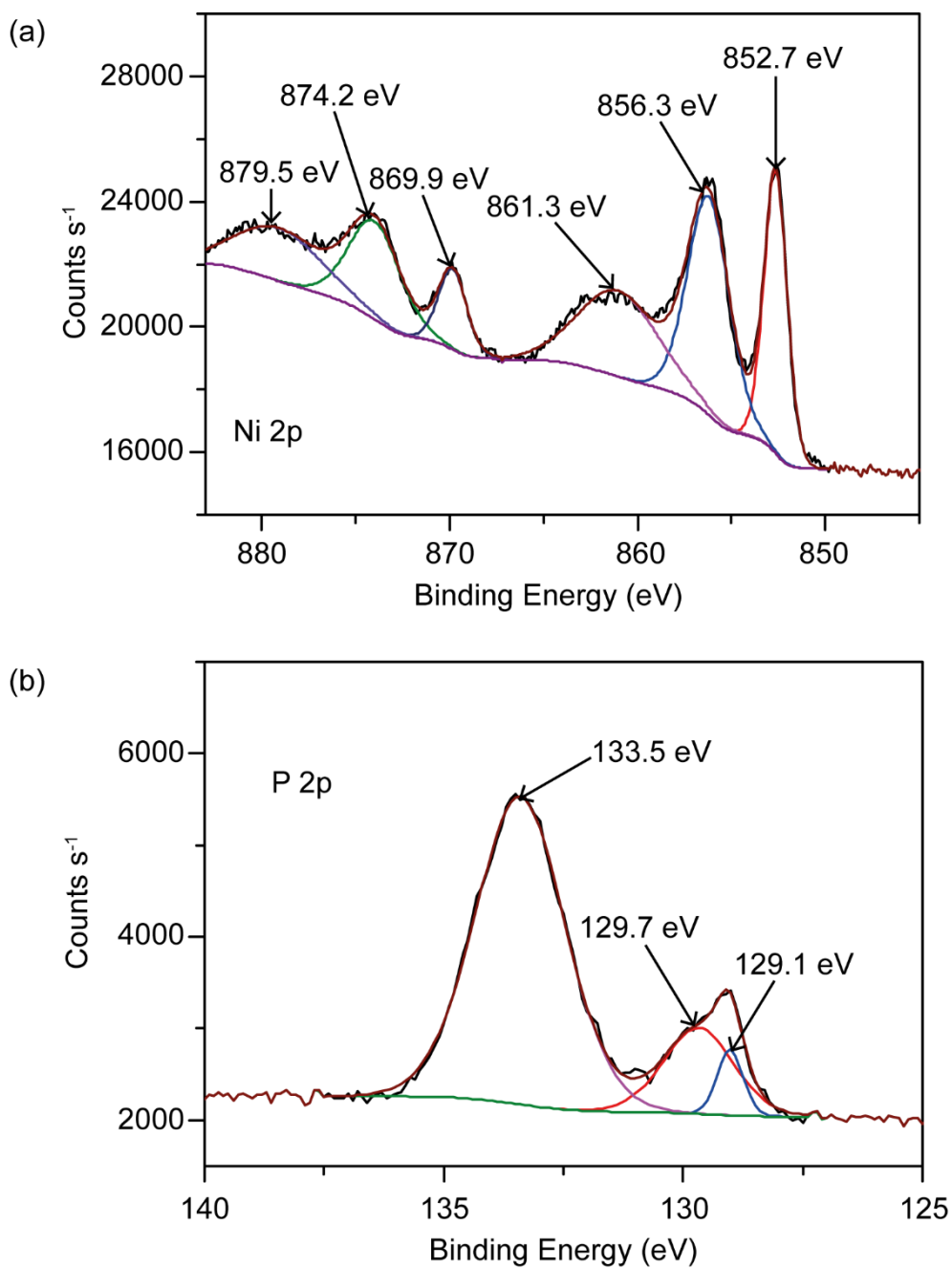


Figure 2.9. XPS spectra of Ni₂P nanoparticle in (a) Ni 2p and (b) P 2p energy levels.

Based on the structural analyses of NiFeP and Ni₂P nanoparticles, NiFeP nanoparticle is proved to be synthesized without a significant change in nickel phosphide crystal structure. However, it is difficult to determine the exact localized bonding environments of iron in the crystal lattice by the aforementioned characterizations. In order to have further information on the structure, the extended X-ray absorption fine structure (EXAFS) measurement is carried out. It measures the average coordination number of surface atoms and estimates bond lengths, and thus helps getting a better picture on the bonding environment and local structure of each element in NiFeP nanoparticle. The data for NiFeP nanoparticle were recorded and the fittings were carried out with satisfaction (Figure 2.10, Figure 2.11, and Table 2.1). The bond lengths of various combinations of elements are estimated, including nickel-phosphorus (Ni-P), nickel-nickel (Ni-Ni), iron-nickel (Fe-Ni), and iron-phosphorus (Fe-P) bonds. Ni-Ni and Ni-P bonds are 2.59 and 2.24 Å, respectively. Meanwhile, Fe-Ni and Fe-P bonds are 2.63 and 2.21 Å, respectively. The EXAFS data confirmed the existence of iron incorporation in nickel phosphide and iron is bonded to both nickel and phosphorus in the crystal lattice. The fitted data from EXAFS measurement of Ni₂P nanoparticle show the Ni-Ni and Ni-P bond lengths in Ni₂P

nanoparticle are 2.59 and 2.25 Å, respectively (Figure 2.12 and Table 2.2). The bond lengths in iron-doped and pristine nickel phosphide nanoparticle are comparable which shows the incorporation of iron in nickel phosphide crystal lattice do not induce significant changes in bond strengths of existing Ni-Ni and Ni-P bonds. Typical coordination numbers in Ni-Ni and Ni-P for Ni₂P are 4 and 2, respectively, which are close to the fittings shown in Table 2.2, having coordination numbers for Ni-Ni and Ni-P as 3.3 and 2.9, respectively.¹³² There is, however, a decrease in the coordination numbers when Fe is introduced into the crystal lattice. The coordination numbers for Ni-Ni and Ni-P in NiFeP nanoparticles are 2.5 and 2.3, respectively, whereas those for Fe-Ni and Fe-P are determined to be 3.6 and 3.7, respectively. The decreased coordination numbers of Ni-Ni and Ni-P indicate successful substitution of Ni with Fe. In addition, the change in coordination number does not reveal a perfect substitution since there is a mismatch between the added coordination numbers of Ni-P and Fe-P in NiFeP nanoparticle and that of Ni-P in Ni₂P nanoparticle.

From the above control experiments for NiFeP nanoparticle synthesis, it was confirmed that iron present in the reaction environment can be incorporated into nickel phosphide crystal lattice without making significant

effect on the morphology, crystal structure, and bonding environment of the resulting nanoparticles.

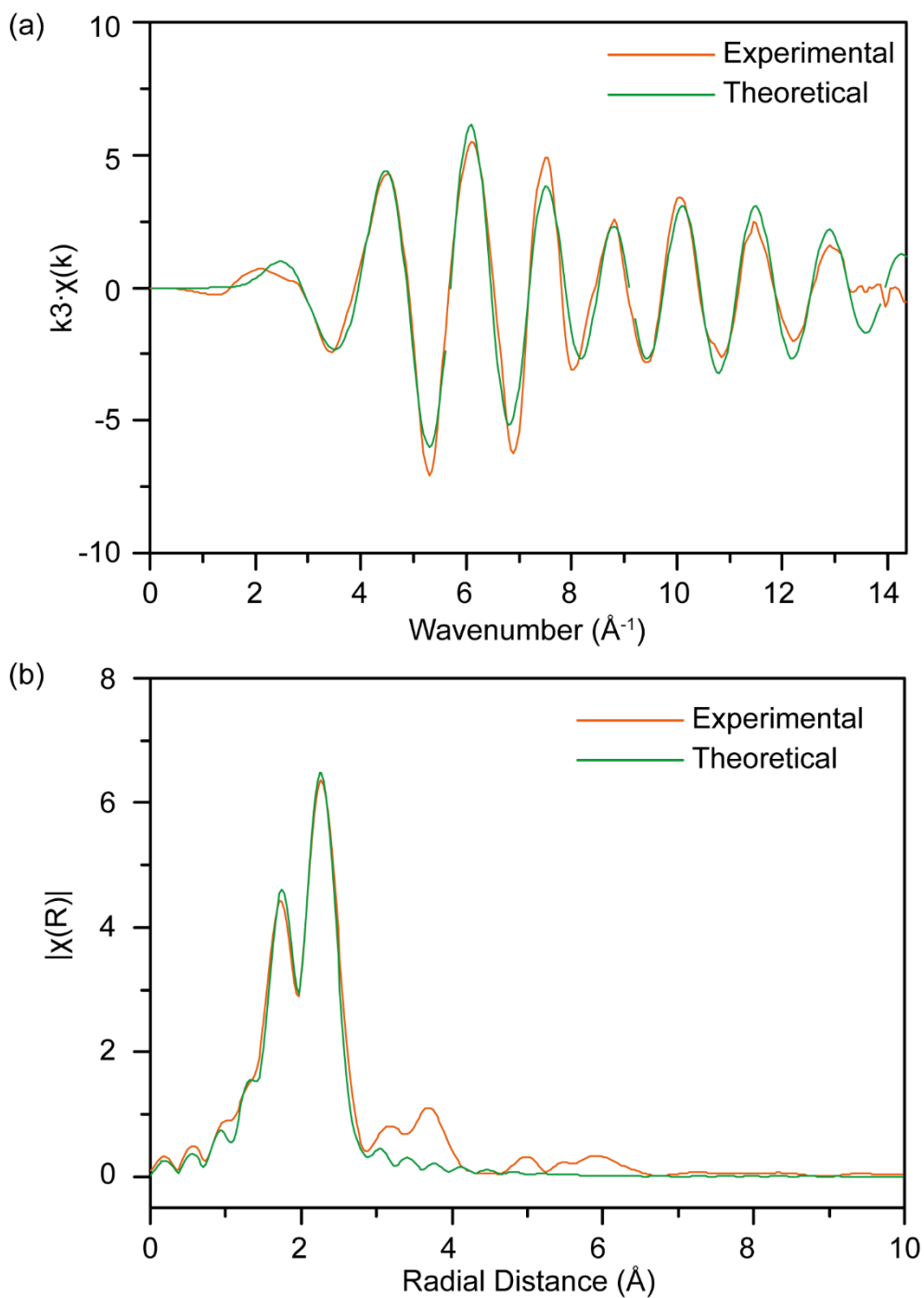


Figure 2.10. EXAFS plots of (a) $k^3 \cdot \chi$ of experimental and fitted data and (b) $k^3 \cdot \chi$ phase corrected Fourier transform of experimental and fitted data for NiFeP nanoparticle with Ni K-edge transmission mode.

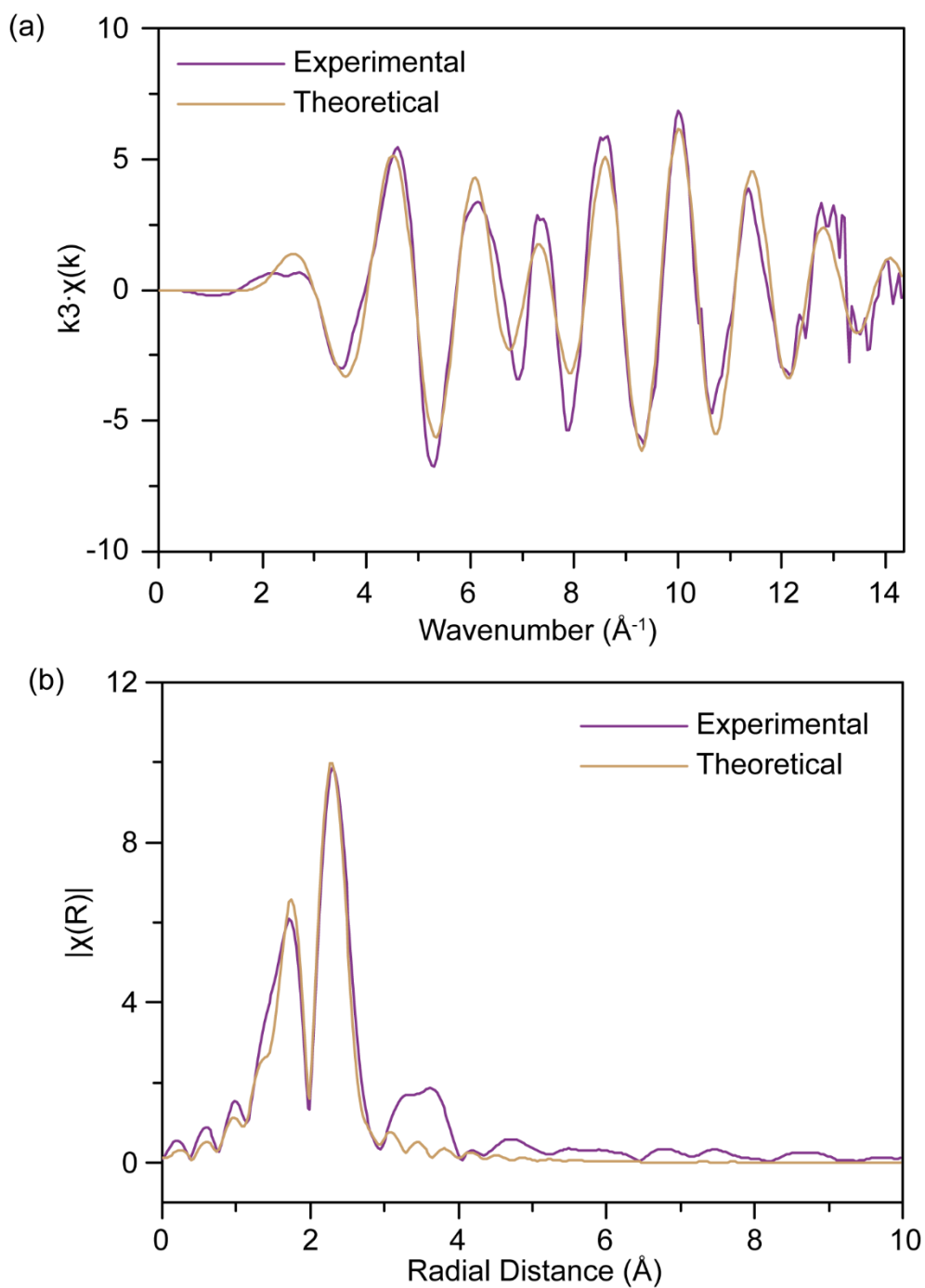


Figure 2.11. EXAFS plots of (a) $k^3 \cdot \chi$ of experimental and fitted data and (b) $k^3 \cdot \chi$ phase corrected Fourier transform of experimental and fitted data for NiFeP nanoparticle with Fe K-edge transmission mode.

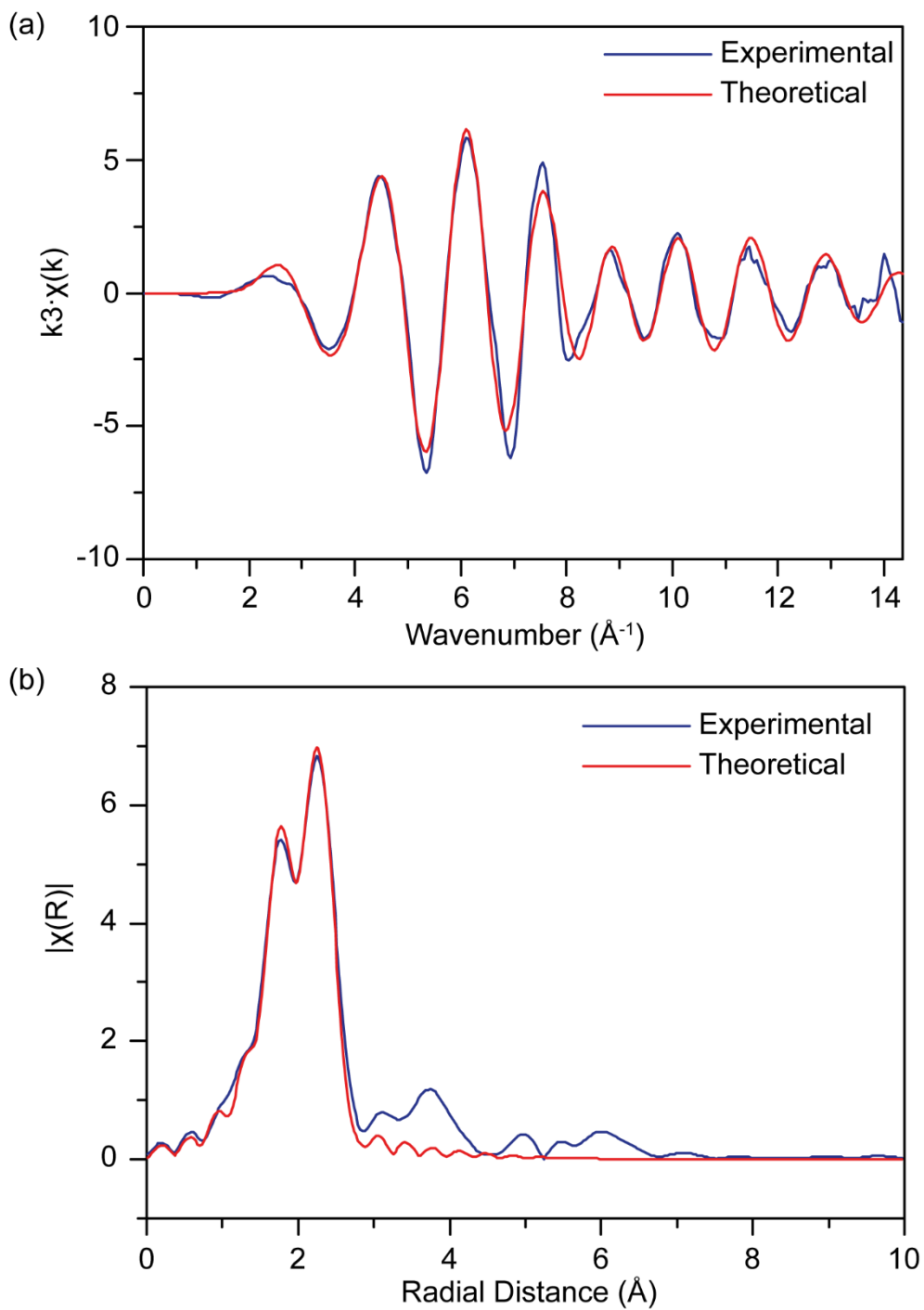


Figure 2.12. EXAFS plots of (a) $k^3 \cdot \chi$ of experimental and fitted data and (b) $k^3 \cdot \chi$ phase corrected Fourier transform of experimental and fitted data for Ni₂P nanoparticle with Ni K-edge transmission mode.

Table 2.1. EXAFS of NiFeP nanoparticle.

Bond	Enot*	Coordination number	ss	Bond length (Å)	R-factor
Ni-P	4.3	2.3(3)	0.008(2)	2.24(1)	1.3%
Ni-Ni		2.5(3)	0.006(1)	2.59(1)	
Fe-P	5.5	3.7(3)	0.007(1)	2.21(1)	2.0%
Fe-Ni		3.6(3)	0.005(1)	2.63(1)	

*Enot is the energy difference of absorption energy in experimental value and calculated value.

Table 2.2. EXAFS of Ni₂P nanoparticle.

Bond	Enot*	Coordination number	ss	Bond length (Å)	R-factor
Ni-P	2.7	2.9(2)	0.008(1)	2.25(1)	0.6%
Ni-Ni		3.3(3)	0.008(1)	2.59(1)	

*Enot is the energy different of absorption energy in experimental value and calculated value.

Numerous literatures have reported that the synthesis of transition metal phosphide nanoparticles involves the use of phosphorus source such as TOP, solvents, and a capping ligand such as oleylamine and octylether only.¹³³⁻¹³⁹ Oleylamine is a common capping ligand widely used in nanoparticle synthesis. It can also play a role as a solvent to dissolve metal precursors. The combined use of TOP and its phosphine oxide (TOPO) is also reported to be crucial for successful formation of NiFeP nanoparticle. However, the role and interaction between each component in synthetic environment are not clearly demonstrated. In particular, how the presence of both TOP and TOPO affects the nanoparticle synthesis need a systematic study.

Control experiments are conducted to investigate the effect of the presence of TOP and/or TOPO on the synthesis of NiFeP nanoparticle. Reactions were carried out in the presence of either TOP or TOPO. In the presence of TOP only, nickel oxide and iron oxide are formed as shown by analysis of XRD, TEM, and EDX in TEM on different regions (Figure 2.13 and Figure 2.14). Through selection of area for elemental analysis, different ratios of each element are obtained. The nickel-to-iron-to-phosphorus ratio in Figure 2.14 (a) is 8.7:1:3.6 where nickel oxide is the predominant phase. Meanwhile in Figure 2.14 (c), the elemental ratio of nickel, iron, and

phosphorus equals 1.2:5.9:1 which indicates iron oxide is predominant in this area. In both areas, detectable phosphorus in EDX spectra is believed to be originated from some surface-bound TOP. Combining the characterizations from XRD and TEM, it is believed that formation of oxide is attributed by partial decomposition of metal acetate that occurs in the presence of TOP. Phosphorization cannot be carried out successfully from partially decomposed precursors, leading to formation of oxides.

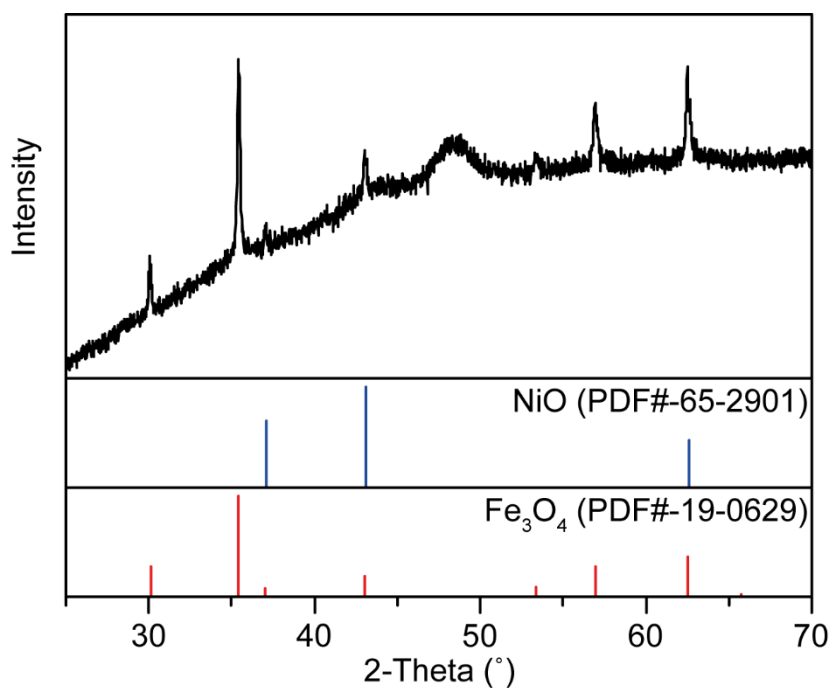


Figure 2.13. XRD pattern of nanoparticle formed in the presence of TOP only.

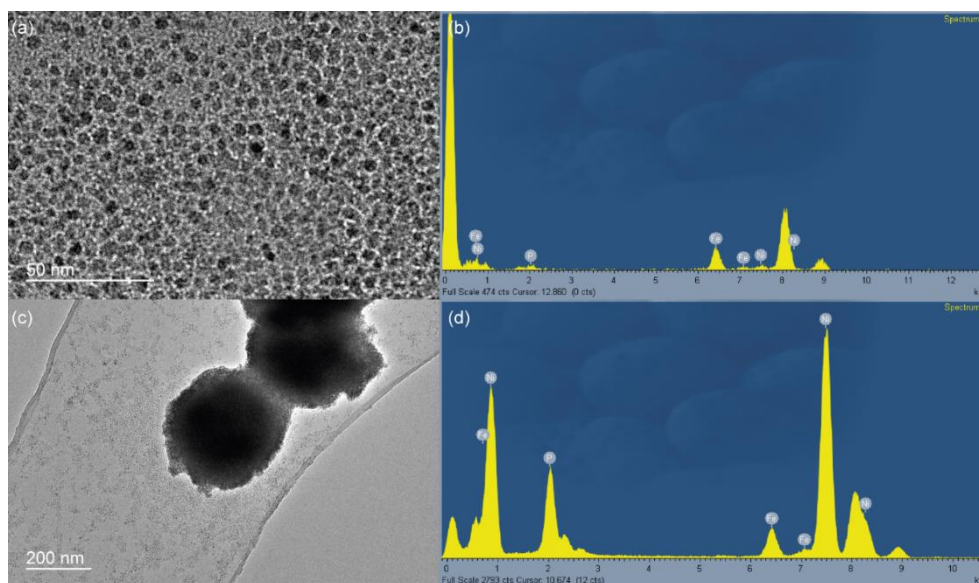


Figure 2.14. TEM images and EDX spectra of (a and b) iron oxide and (c and d) nickel oxide.

In contrast, the synthesis carried out in the presence of TOPO only leads to the formation of nickel metal nanoparticles as revealed from its XRD pattern (Figure 2.15). The peak shift from reference nickel XRD pattern (PDF#-04-0850) is possibly due to the incorporation of iron in nickel hexagonal close pack crystal structure. The TEM image shows highly monodispersed nickel nanoparticles with narrow size distribution (Figure 2.16), attributed to the presence of TOPO, a better capping ligand than TOP. EDX spectrum shows nickel as major component and iron as minor component (Figure 2.17). Although there is a trace amount of phosphorus detected, it is believed to be originated from the surface-bound TOPO on the nanoparticle because the XRD pattern of as-synthesized nanoparticle

suggested no phosphide formation. Since the phosphorus source (TOP) is not added in reaction environment and the phosphorus in TOPO is believed to be not readily available, thus the phosphorization cannot be successfully carried out and quenched in the stage of metal nanoparticle.

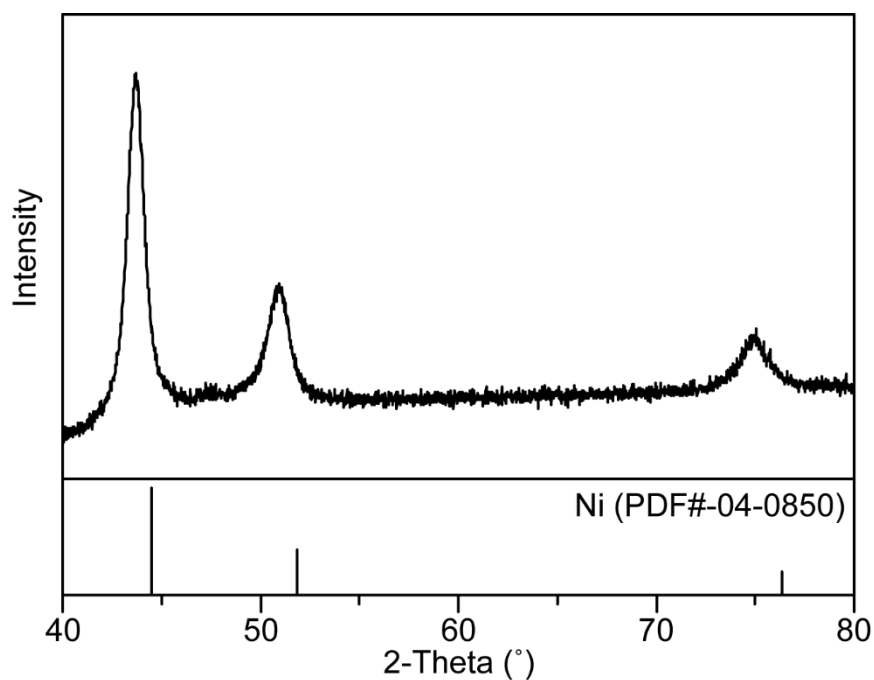


Figure 2.15. XRD pattern of nanoparticle synthesized in the presence of TOPO only.

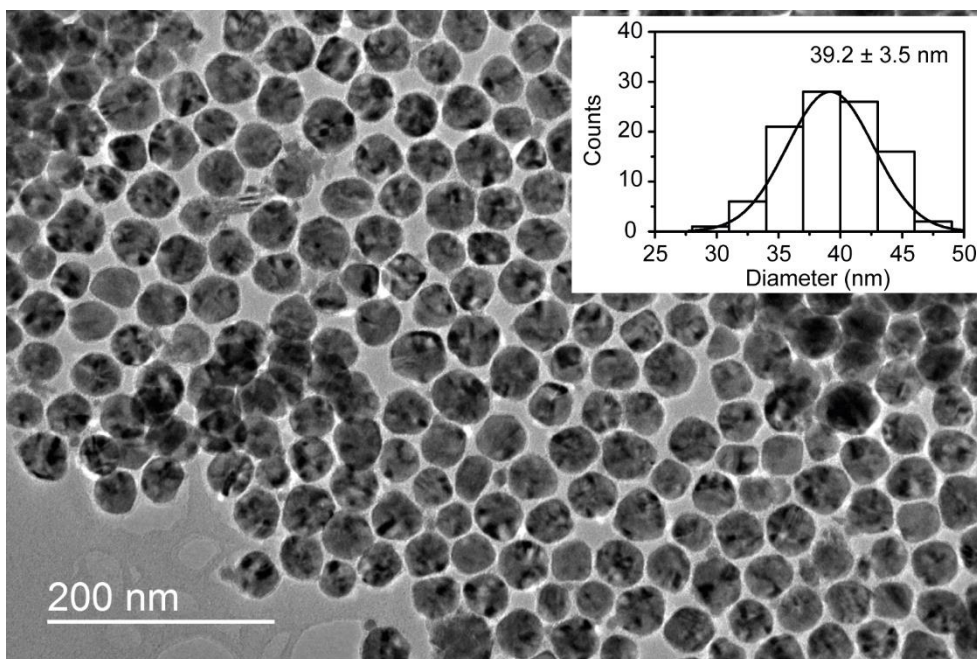


Figure 2.16. TEM image of metal nanoparticle synthesized in the presence of TOPO. Inset shows the size distribution of metal nanoparticle.

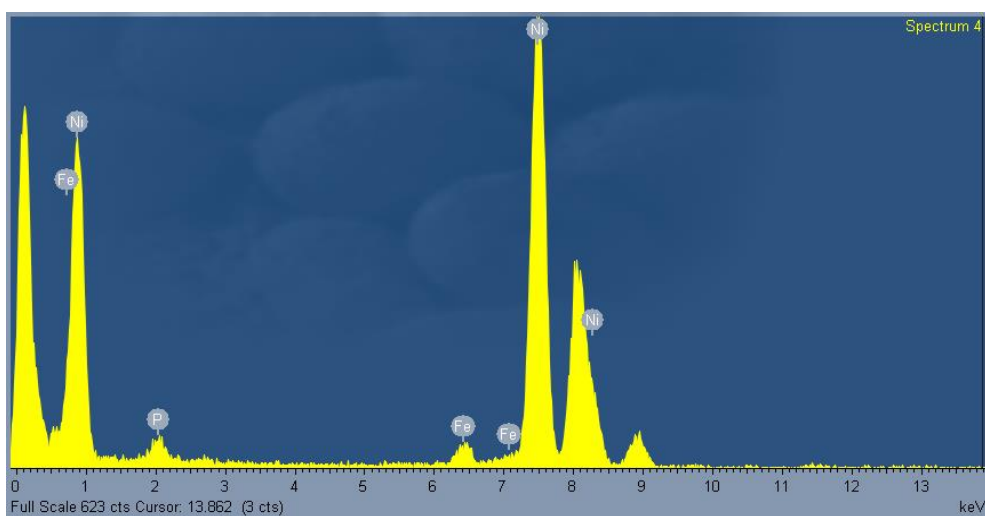


Figure 2.17. EDX spectrum of nanoparticle synthesized in the presence of TOPO only.

The scope of metal doping is extended to other transition metal ions including cobalt, manganese, and molybdenum ions. Cobalt(II) acetate is used instead of iron(II) acetate as a precursor in synthesis to prepare cobalt-doped nickel phosphide (NiCoP) nanoparticle.

XRD pattern of NiCoP nanoparticle resembles the Ni₂P reference pattern (PDF#-65-1989, Figure 2.18). Due to the similarity of nickel(II) and cobalt(II) ions, a larger extent of incorporation occurs. This leads to a significant distortion of crystal structure which leads to a symmetric peak shift towards higher angles. The first three peaks in XRD pattern of NiCoP nanoparticle clearly show this effect.

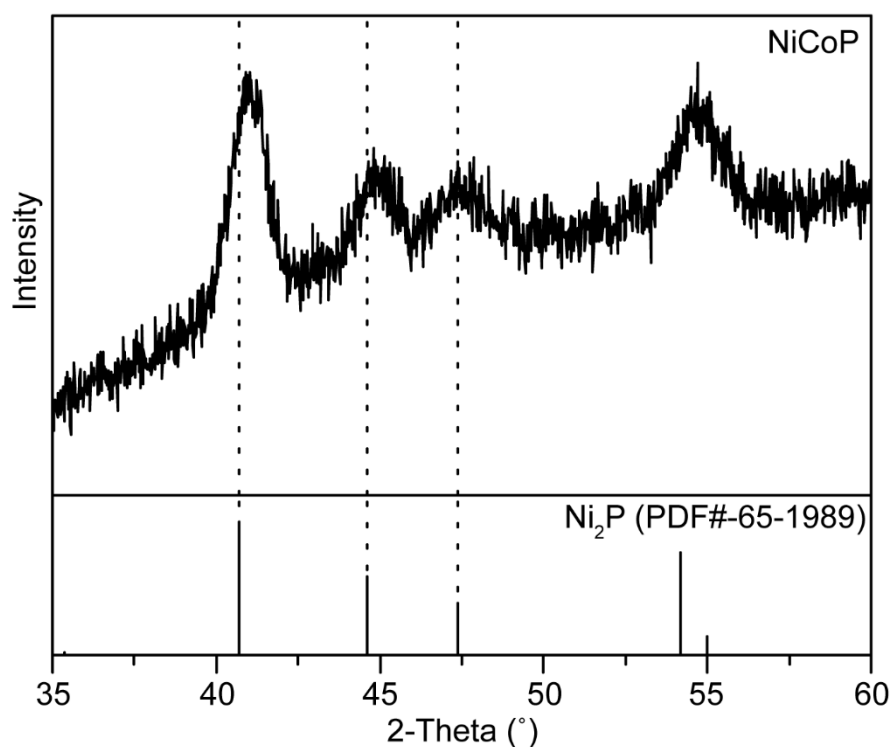


Figure 2.18. XRD pattern of NiCoP nanoparticle.

TEM image shows NiCoP nanoparticle is spherical with an average diameter of 7.7 ± 0.9 nm (Figure 2.19 (a) and (b)). The HR-TEM further reveals the lattice fringe of (111) and (201) plane with their characteristic d -spacings of 0.223 and 0.205 nm, respectively (Figure 2.19 (c)). Electron diffraction pattern shows four distinct rings of diffraction which correspond to (111), (201), (210) and (300) lattice planes, respectively (Figure 2.19 (d)). Element composition confirms a significant degree of Co incorporation which agrees well with XRD peak shifting (Figure 2.20). The normalized elemental ratio of nickel-to-cobalt-to-phosphorus determined from EDX is 1:0.55:1.2.

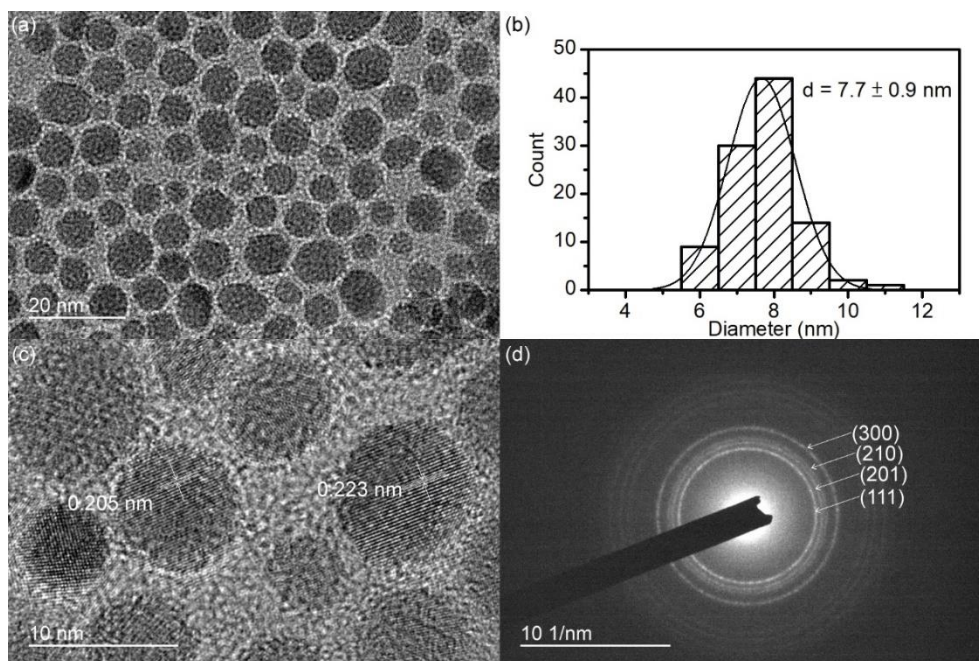


Figure 2.19. (a) TEM, (b) and its size distribution, (c) HRTEM images, and (d) electron diffraction pattern of NiCoP nanoparticles.

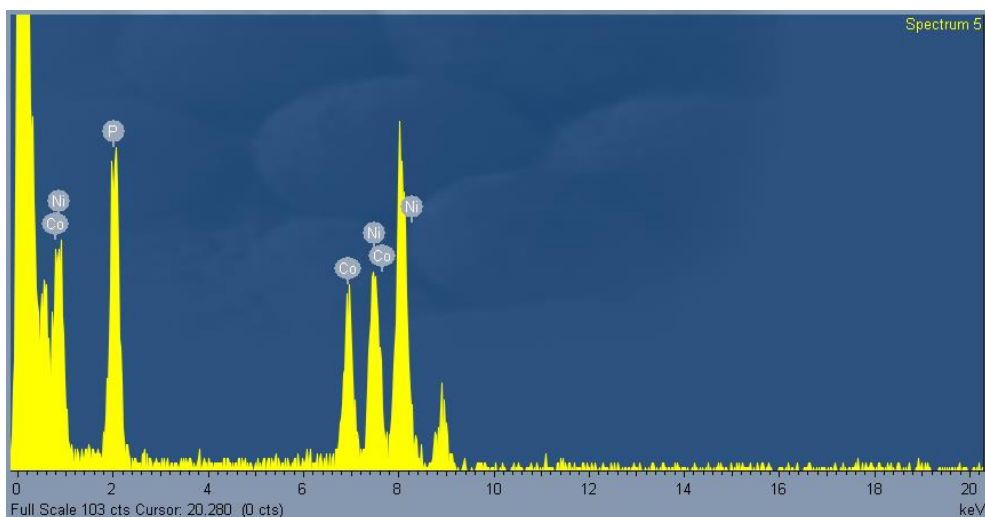


Figure 2.20. EDX spectrum of NiCoP nanoparticle.

In order to obtain information on chemical states of different elements in NiCoP nanoparticle, XPS was carried out for nickel, cobalt, and phosphorus in 2p region. In Ni 2p XPS spectrum (Figure 2.21 (a)), the peaks at 852.9, 856.2, and 861.3 eV correspond to nickel in nickel-phosphorus bond, oxidized nickel species and its satellite peak in Ni 2p_{3/2} energy level, respectively. Meanwhile, the peaks at 870.1, 874.1, and 877.5 eV correspond to nickel in nickel-phosphorus bond, oxidized nickel species and its satellite peak in Ni 2p_{1/2} energy level, respectively. In Co 2p XPS spectrum (Figure 2.21 (b)), the peak at 778.2 eV originates from cobalt in cobalt-phosphorus bond in Co 2p_{3/2} energy level while the peak at 793.1 eV for the bond in Co 2p_{1/2} energy level.¹⁴⁰ Binding energy of cobalt in cobalt-phosphorus bond is close to that of elemental cobalt, which indicates it has a

small positive charge.¹⁴¹ The peaks at 781.5 and 784.8 eV correspond to oxidized cobalt species (cobalt oxide and cobalt phosphate) and its satellite peak, respectively. In P 2p XPS spectrum, three peaks can be observed at 129.2, 129.8, and 133.5 eV. The peak at 133.5 eV originates from phosphate ion formed from oxidation of phosphide ion. The peaks at 129.2 and 129.8 eV are attributed to cobalt-phosphorus and nickel-phosphorus bonds, respectively (Figure 2.21 (c)).

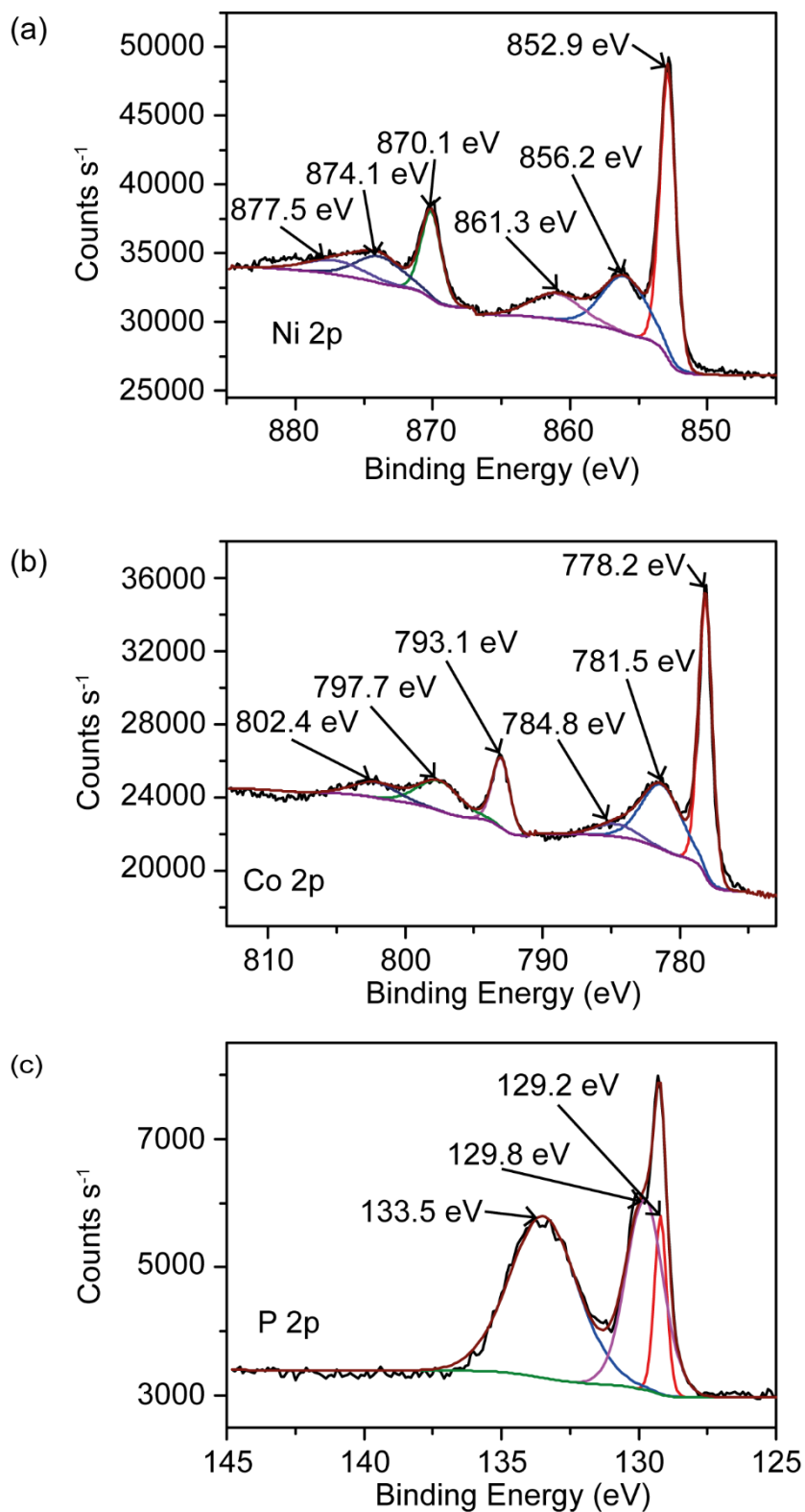


Figure 2.21. XPS spectra of NiCoP nanoparticle in (a) Ni 2p, (b) Co 2p, and (c) P 2p regions.

Because of the high similarity of cobalt and nickel ion, cobalt can be easily incorporated into the nickel phosphide crystal lattice. The degree of incorporation can be tuned by simply changing the ratio of nickel and cobalt precursors. NiCoP nanoparticles were prepared under different nickel-to-cobalt ratio, from 3:1, 2:1, 1:1, to 1:2 (abbreviated as NiCoP31, NiCoP21, NiCoP11, and NiCoP12, respectively).

XRD patterns were obtained from different NiCoP nanoparticles and shown in Figure 2.22. In general, similar patterns were observed but the intensity decreases with the amount of cobalt precursor used. This indicates the increase in cobalt incorporation decreases the crystallinity from pristine nickel phosphide crystal.

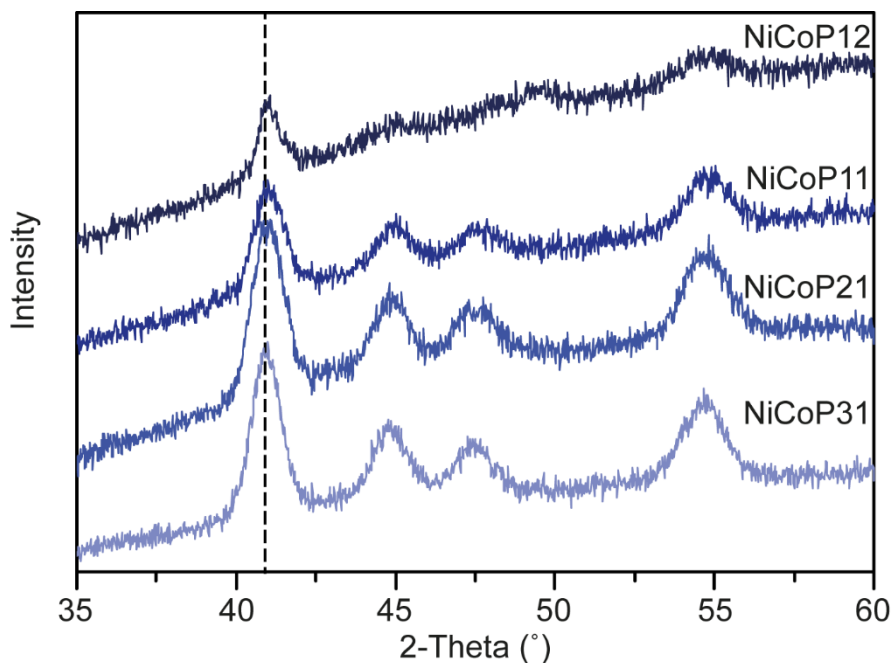


Figure 2.22. XRD patterns of various NiCoP nanoparticles prepared under different Ni:Co precursor ratios.

TEM images were taken for different NiCoP nanoparticles (Figure 2.23).

The as-synthesized nanoparticles show no significant difference with varying nickel-to-cobalt precursor ratio. However, the composition ratio determined by EDX changes with the precursor ratio. The normalized composition ratios of different NiCoP nanoparticles are shown in Table 2.3. Ratios between nickel and cobalt increase linearly with the respective precursor ratios (Figure 2.24). This result shows that the property of NiCoP nanoparticle can be easily tuned by adjusting the relative composition ratio between nickel and cobalt.

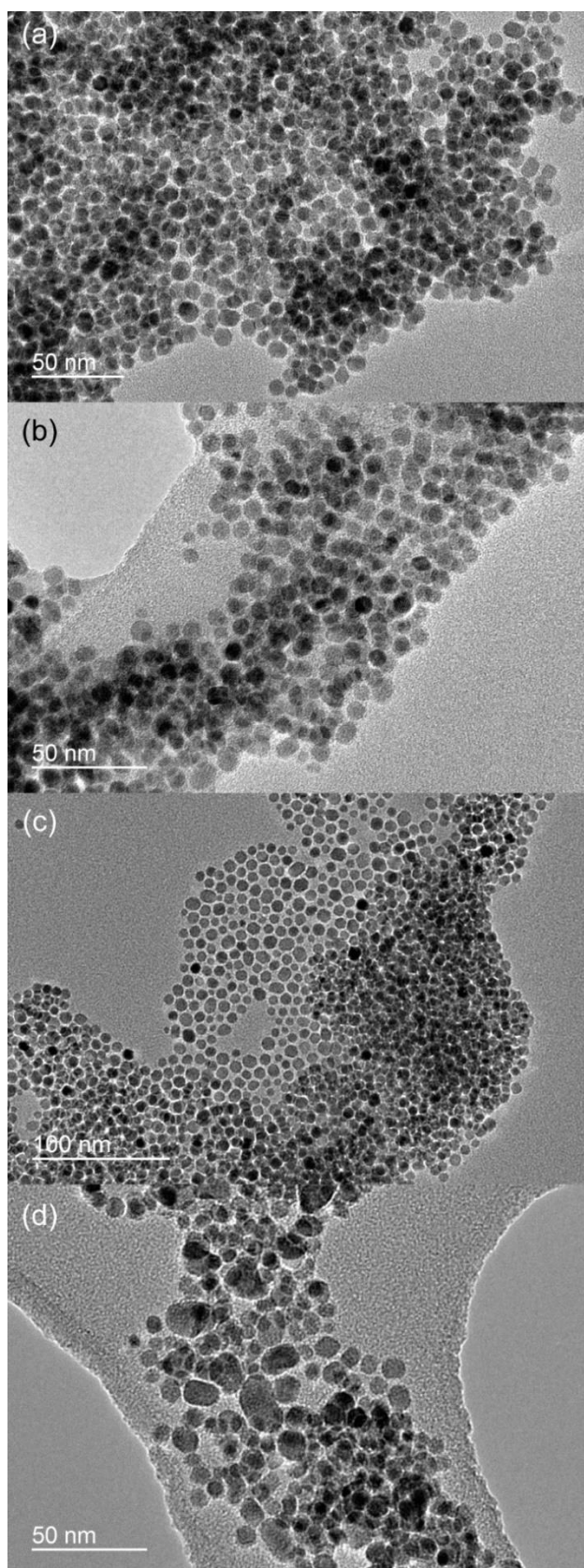


Figure 2.23. TEM images of different NiCoP nanoparticles (a) NiCoP31, (b) NiCoP21, (c) NiCoP11, and (d) NiCoP12 nanoparticles.

Table 2.3. Normalized elemental ratios of different NiCoP nanoparticles prepared under different nickel-to-cobalt precursor ratios.

	Ni	Co	P
NiCoP31	1.3(3)	0.33(7)	1
NiCoP21	1.1(2)	0.37(5)	1
NiCoP11	0.83(7)	0.46(1)	1
NiCoP12	0.74(4)	1.02(3)	1

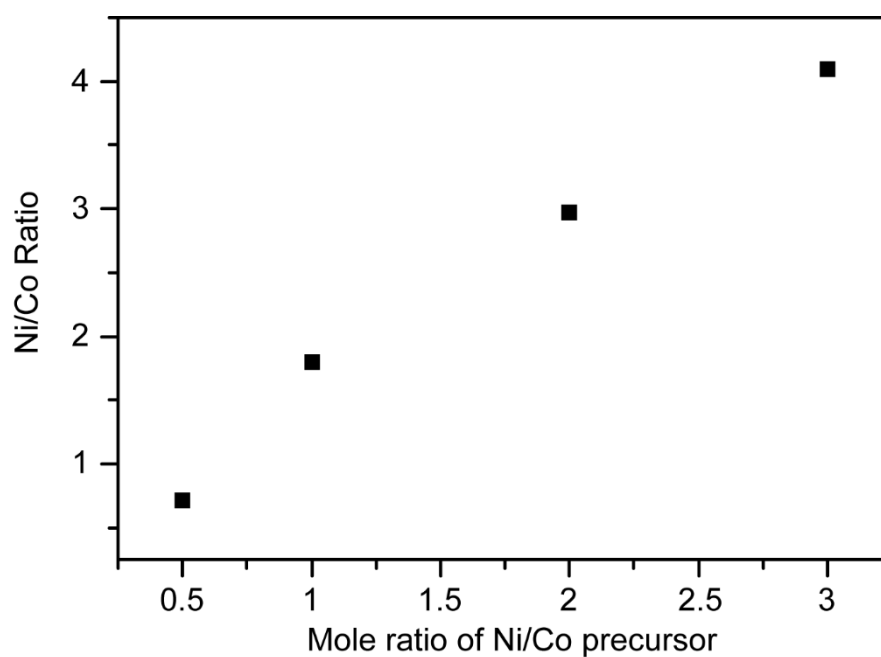


Figure 2.24. Relationship of elemental ratio between actual and loading nickel-to-cobalt ratios.

Manganese-doped nickel phosphide (NiMnP) nanoparticle is synthesized in the presence of manganese(III) acetate dihydrate following similar experiment procedures as NiFeP nanoparticle. The XRD pattern of NiMnP nanoparticle resembles the reference Ni₂P diffraction pattern (PDF#-65-1989, Figure 2.25).

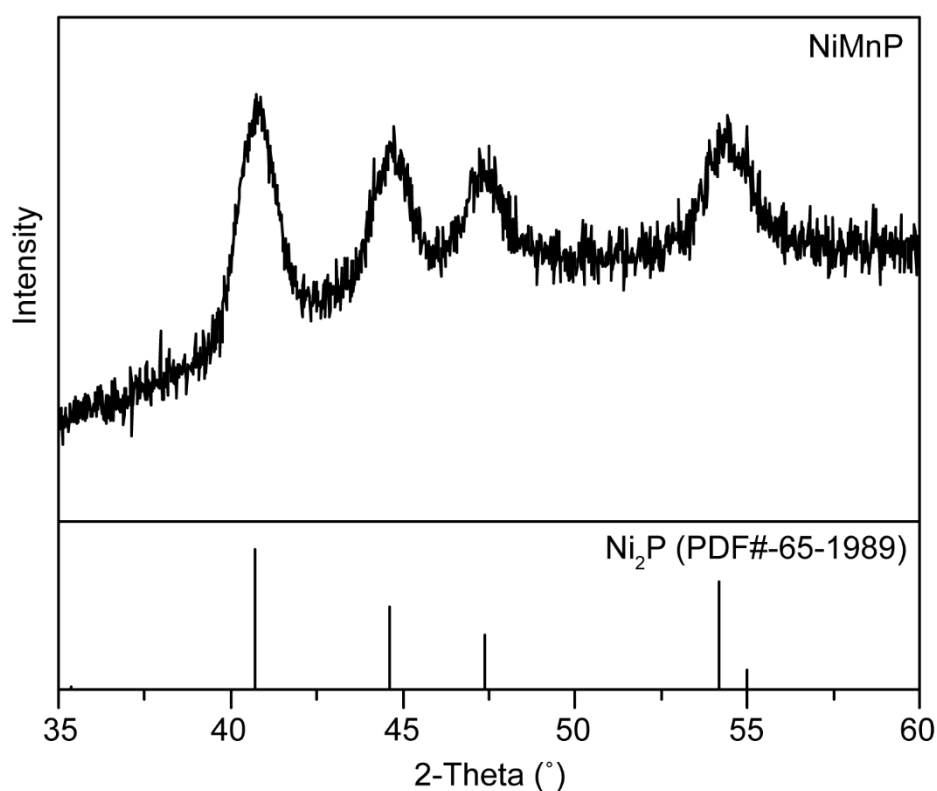


Figure 2.25. XRD pattern of NiMnP nanoparticle.

TEM image shows the as-synthesized NiMnP nanoparticle is spherical with an average diameter of 7.6 ± 1 nm (Figure 2.26 (a) and (b)). HR-TEM image shows the lattice fringes of (111) and (201) lattice planes, having *d*-spacings of 0.228 and 0.203 nm, respectively (Figure 2.26 (c)). Electron

diffraction pattern shows the rings of diffraction for (111), (201), (210), and an indistinguishable ring for (300) and (211) lattice planes (Figure 2.26 (d)).

The elemental analysis by EDX shows nickel-to-manganese-to-phosphorus ratio of the as-synthesized NiMnP nanoparticle is 1:0.05:0.7 (Figure 2.27).

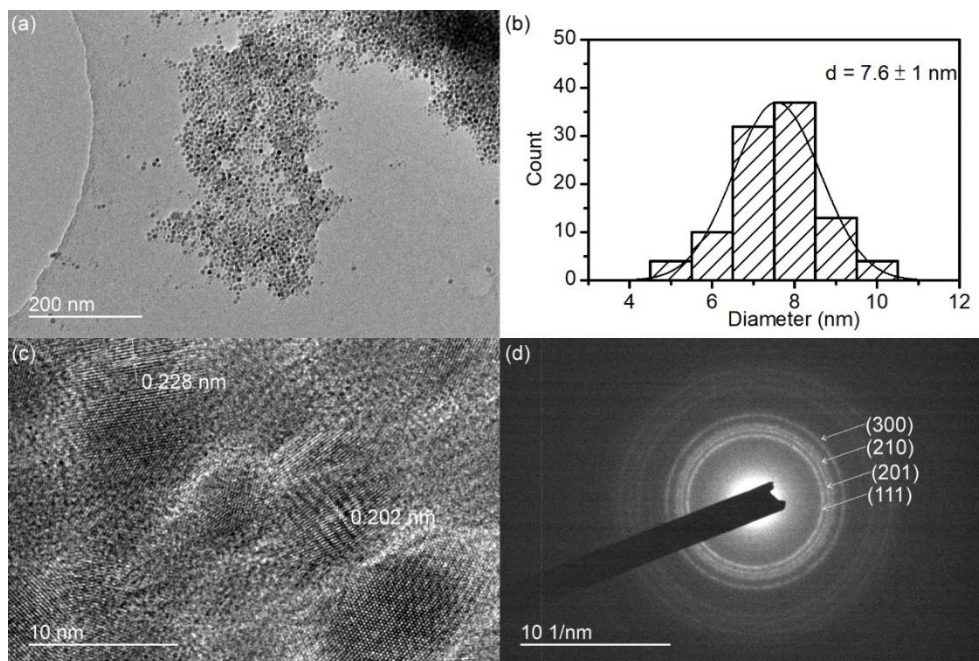


Figure 2.26. (a) TEM, (b) and its size distribution, (c) HRTEM images, and (d) electron diffraction pattern of NiMnP nanoparticles.

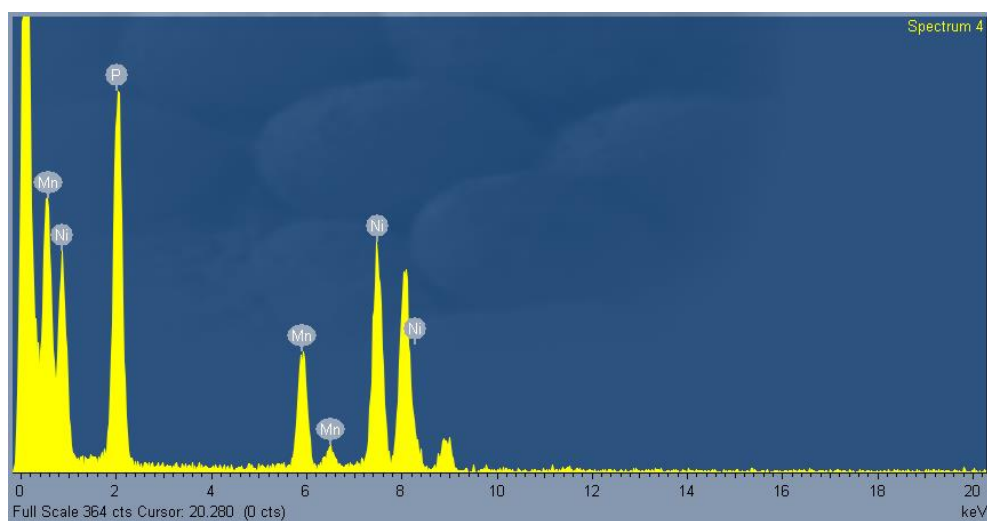


Figure 2.27. EDX spectrum of NiMnP nanoparticle.

XPS measurement was carried out for Ni 2p, Mn 2p, and P 2p energy levels (Figure 2.28). In Ni 2p XPS spectrum, the peaks at 852.9 and 870.1 eV correspond to nickel-phosphorus bond in Ni 2p_{3/2} and 2p_{1/2} energy levels, respectively. The peaks at 856.2 and 874.1 eV correspond to oxidized nickel species while peaks at 861.3 and 877.5 eV is the satellite peaks in Ni 2p_{3/2} and 2p_{1/2} energy levels, respectively (Figure 2.28 (a)).³³ In Mn 2p XPS spectrum, the small peak at 638.7 eV originates from manganese in manganese-phosphorus bond in 2p_{3/2} energy level. The peaks at 641.8 and 653.7 eV comes from oxidized manganese species, such as Mn₂O₃ and MnO, while the peaks at 645.1 and 655.0 eV are the satellite peaks of oxidized manganese species in Mn 2p_{3/2} and 2p_{1/2} energy levels, respectively (Figure 2.28 (b)).¹²⁹ In XPS spectrum of P 2p region, the peaks at 129.3 and 130.1 eV correspond to phosphorus in metal-phosphorus bond. Meanwhile, oxidized phosphorus species such as phosphate comprises peaks at 132.8 and 134.3 eV in P 2p region (Figure 2.28 (c)).³³

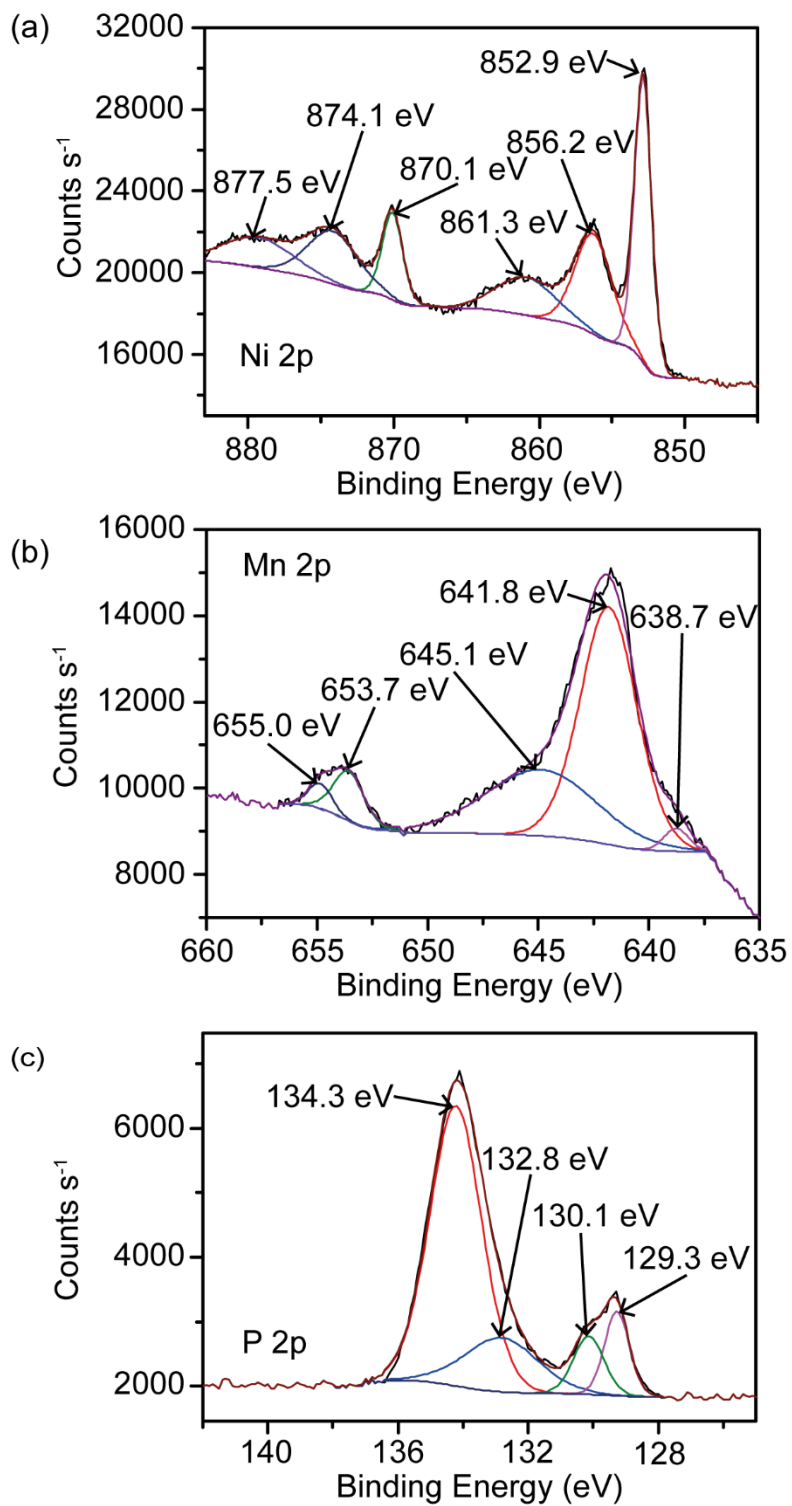


Figure 2.28. XPS spectra of NiMnP nanoparticle in (a) Ni 2p, (b) Mn 2p, and (c) P 2p energy levels.

Molybdenum-doped nickel phosphide (NiMoP) nanoparticle is prepared using molybdenum(II) acetate dimer. NiMoP nanoparticle has a hexagonal structure which exhibits a XRD pattern that matches the Ni₂P reference pattern (PDF#-65-1989, Figure 2.29). The as-synthesized NiMoP nanoparticle is spherical with an average diameter of 5.3 ± 1 nm, which is about 2 nm smaller in diameter than the previous metal-doped and pristine nickel phosphide nanoparticles (Figure 2.30 (a) and (b)). The HR-TEM image shows lattice fringes with *d*-spacings of 0.22 nm and 0.209 nm which are (111) and (201) lattice planes, respectively (Figure 2.30 (c)). The selected area electron diffraction pattern shows diffraction rings of (111) and (300) as the innermost and outermost distinctive rings, respectively (Figure 2.30 (d)). The elemental analysis by EDX shows the elemental ratio between nickel, molybdenum, and phosphorus is 1.6:0.08:1 (Figure 2.31).

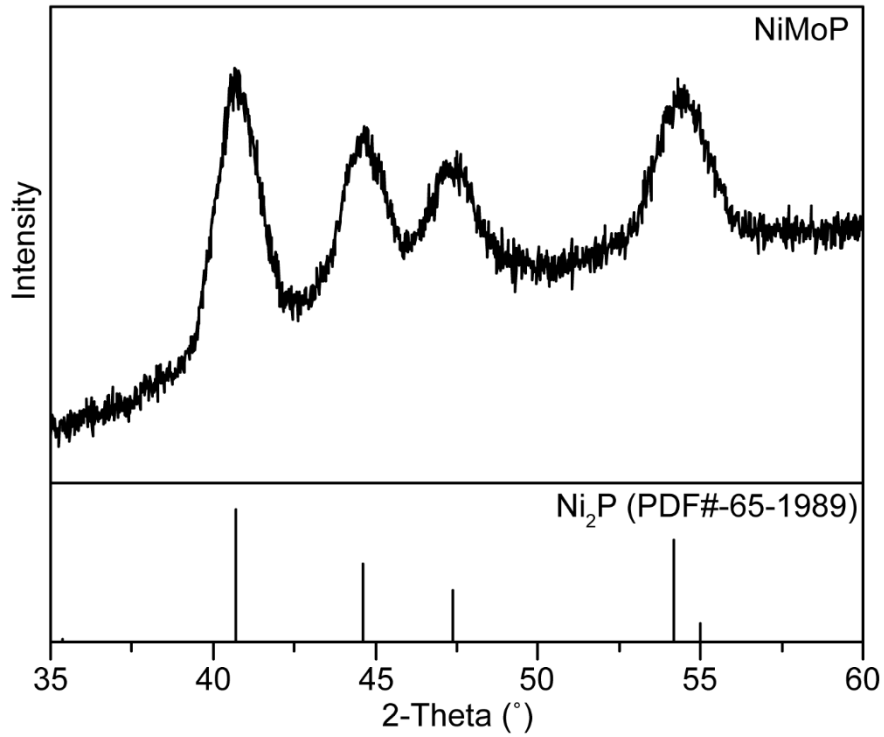


Figure 2.29. XRD pattern of NiMoP nanoparticle.

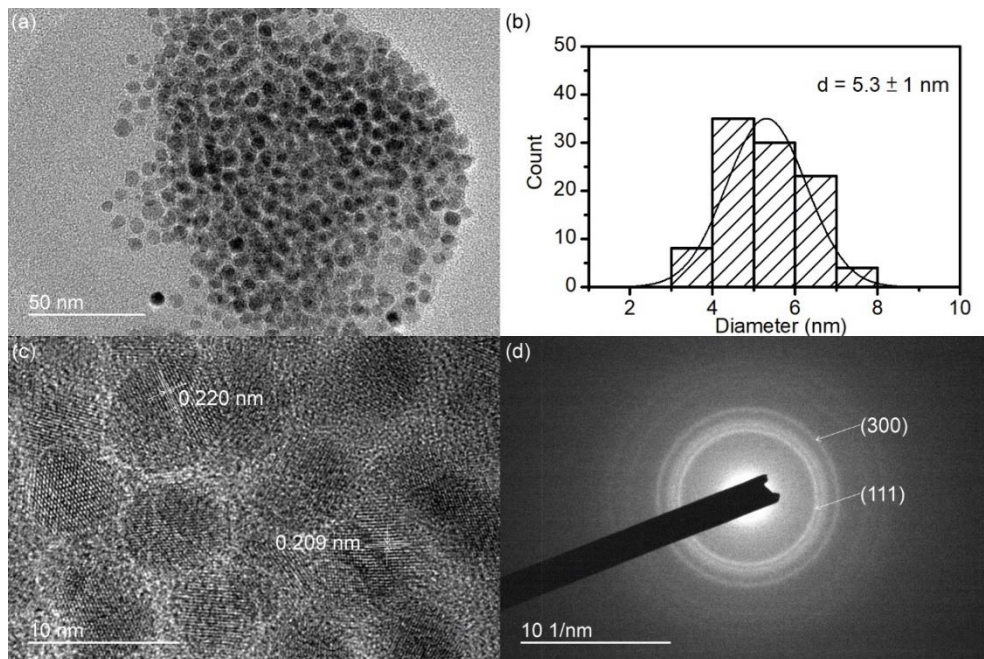


Figure 2.30. (a) TEM, (b) and its size distribution, (c) HRTEM image, and (d) electron diffraction pattern of NiMoP nanoparticle.

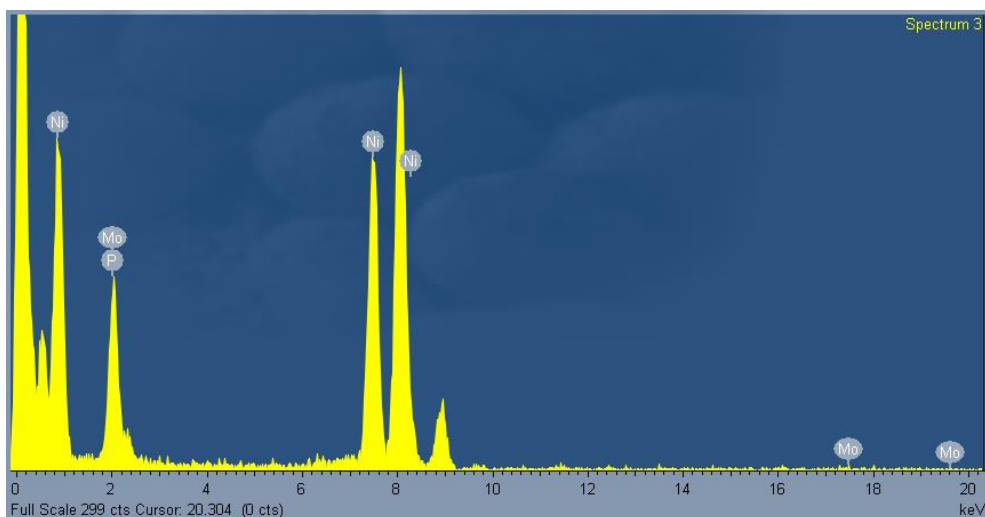


Figure 2.31. EDX spectrum of NiMoP nanoparticle.

XPS spectra are obtained for Ni 2p, Mo 3d and P 2p region from NiMoP nanoparticle (Figure 2.32). In Ni 2p region, similar spectrum is obtained as other metal-doped nickel phosphide nanoparticles. The peaks at 853.0 and 870.2 eV originate from nickel in nickel-phosphorus bond in $2p_{3/2}$ and $2p_{1/2}$ energy levels, respectively (Figure 2.32 (a)). The small deviation from binding energy of elemental nickel indicates a small positive charge on nickel ion. The peaks at 856.4 and 874.4 eV originate from oxidized nickel species, such as NiO, in Ni $2p_{3/2}$ and $2p_{1/2}$ energy levels, respectively. Meanwhile the peaks at 861.0 and 879.3 eV are the satellite peaks from oxidized nickel species in Ni $2p_{3/2}$ and $2p_{1/2}$ energy levels, respectively.³³ The XPS spectrum in Mo 3d region is measured with a comparatively small signal-to-noise ratio because the incorporation of molybdenum in nickel phosphide crystal lattice

is small. Nevertheless, deconvolution of peaks in Mo 3d XPS spectrum is carried out (Figure 2.32 (b)). Peaks at 227.9 and 231.0 eV correspond to molybdenum in molybdenum-phosphorus bond in Mo 3d_{5/2} and Mo 3d_{3/2} energy levels, respectively. Other peaks in spectrum correspond to molybdenum oxide formation including MoO₂ (228.6 and 233.4 eV in Mo 3d_{5/2} and Mo 3d_{3/2} energy levels, respectively) and MoO₃ (232.2 and 236.0 eV in Mo 3d_{5/2} and Mo 3d_{3/2} energy levels, respectively).¹⁴²⁻¹⁴³ In P 2p region, the peaks at 129.3 and 130.0 eV correspond to phosphorus in metal-phosphorus bond while the peak at 133.5 eV comes from oxidation of phosphide to phosphate (Figure 2.32 (c)).

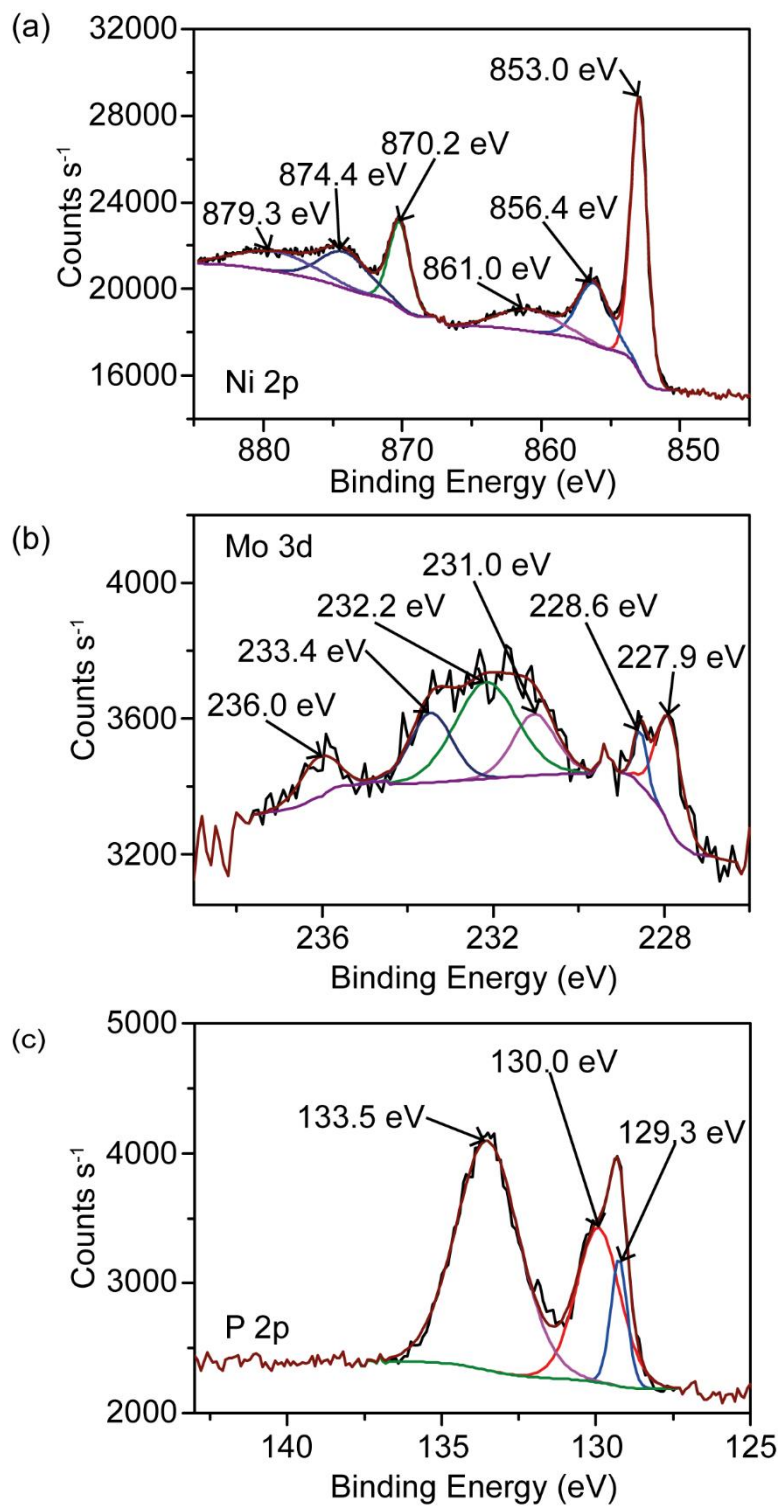


Figure 2.32. XPS spectra of NiMoP nanoparticle in (a) Ni 2p, (b) Mo 3d, and (c) P 2p energy levels.

2.4 Conclusion

Various transition metals, including cobalt, iron, manganese, and molybdenum, has been successfully doped into the nickel phosphide crystal lattice. The as-synthesized metal-doped nickel phosphide nanoparticles are spherical with an average diameter of approximately 7 nm except for molybdenum-doped nickel phosphide nanoparticle (diameter = 5.3 ± 1 nm). The crystal structures of all metal-doped nickel phosphide nanoparticles are hexagonal which matched well with the Ni_2P reference pattern (PDF#-65-1989). The elemental compositions of different metal-doped nickel phosphide nanoparticles were summarized in Table 2.4. With VB-XPS measurement, metal-doped and pristine nickel phosphide nanoparticles are believed to possess metallic property. XPS measurement further confirms the metallic property since the binding energies of different metal-phosphorus bonds in all metal 2p regions (except for Mo in 3d region) are close to their zero-valent state (M^0) which indicate small positive charge on metal ions. In particular, EXAFS measurement was carried out on iron-doped nickel phosphide nanoparticle which showed iron has neighboring nickel and phosphorus which indicates successful incorporation in iron-doped nickel phosphide nanoparticle.

Amount of metal doping is highly dependent on the similarity between nickel and target metal. Cobalt, as a neighbor atom of nickel, allows tuning on degree of incorporation by simply varying loading of Co precursor ratio. The variation in amount of cobalt incorporation leads to a slight shift in XRD pattern but no significant change in crystal structure and morphology.

Based on the characterizations presented in this chapter, different metal-doped nickel phosphide nanoparticles are successfully synthesized using simple wet-chemistry method. The as-prepared nanoparticles are employed in different catalytic reactions which will be described in the following chapters.

Table 2.4. Summary of composition ratios of different transition metal-doped nickel phosphide nanoparticles.

	Ni	M	P
Ni ₂ P	1.8(2)	-	1
NiCoP	0.83(7)	0.46(1)	1
NiFeP	1.4(1)	0.14(1)	1
NiMnP	1.4(3)	0.07(2)	1
NiMoP	1.6(2)	0.08(2)	1

Chapter 3 Metal-doped Nickel Phosphide Nanoparticles in

Electrocatalytic and Photocatalytic Hydrogen Evolution

Reaction (HER)

3.1 Introduction

Hydrogen is considered as one of the most promising next-generation energy sources as its combustion can generate a large amount of energy (120 kJ/g) with water as the only product of combustion.¹⁴² Therefore, hydrogen is regarded as a zero-emission fuel of which combustion product causes no harm to the environment. Currently, hydrogen gas is commonly produced by two methods: (1) steam reforming of methane and (2) alkaline water electrolysis. Steam reforming of methane requires a huge amount of energy input. High reaction temperature (700-1000 °C) and elevated pressure (3-25 bar) are typically required in industrial steam reforming, which makes this method neither economic nor environmental friendly.¹⁴⁵ Alkaline water electrolysis uses electricity to generate hydrogen gas using nickel-based electrodes.¹⁴⁶ The efficiency of alkaline water electrolyzer is largely dependent on the catalyst employed as an electrode material. Its activity and efficiency are limited by energy barrier, which leads to energy loss and increase in the cost of operation, in alkaline water electrolysis. In order to produce large-scaled

hydrogen cost-effectively, it is desired to develop a highly efficient and robust catalyst.

As a green and economic alternative, electrocatalytic and photocatalytic hydrogen evolution reactions (HERs) offer attractive pathways for the generation of hydrogen.¹⁴⁷ Platinum is known to as an excellent catalyst for electrochemical hydrogen generation with its large catalytic current with small overpotential.¹⁴⁸ However, wide and practical applications of Pt in HER is limited by the scarcity and high price. Researchers have devoted much efforts in the development of HER catalysts based on non-toxic, cheap, and earth abundant transition metals to substitute noble metal catalysts. Titanium dioxide (TiO₂) is the most widely studied materials for HER. Photoelectrochemical HER using TiO₂ was first demonstrated by Fujishima and Honda in 1972.⁵⁹ After that, numerous studies were conducted to investigate the feasibility in electrocatalytic and photocatalytic HER.¹⁴⁹⁻¹⁵⁴ Platinum was employed as co-catalyst to yield a hydrogen production rate of 5 $\mu\text{mol h}^{-1} \text{g}^{-1}$ in 1981.¹⁵⁵ With on-going development, Pt-loaded TiO₂ was prepared and employed as HER photocatalyst with a good hydrogen production rate of 1.9 $\text{mmol h}^{-1} \text{g}^{-1}$.¹⁵⁶ Another example is molybdenum disulfide (MoS₂) which shows excellent catalytic activity for the

electrochemical HER.¹⁵⁷ MoS₂ nanoparticle on reduced graphene oxide showed a low overpotential (~100 mV) and small Tafel slope (41 mV dec⁻¹) which is comparable to Pt.⁷ Nickel-based catalysts are also one of the best candidates for electrochemical HER. Nickel is more abundant than noble metals as well as molybdenum. Several studies have demonstrated catalytic activity of nickel-based catalysts in HER such as nickel-containing alloys and complexes, and nickel phosphide.^{13, 27-28, 158-162} Nickel-molybdenum alloy was found as an active HER electrocatalyst in 1984 which has a low overpotential of 89 mV at 1 A cm⁻².¹⁵⁸ Nickel complex was used to construct an efficient photocatalytic system for HER with cadmium selenide quantum dot as photosensitizer, yielding a turnover number over 13000.¹⁶² In addition to nickel alloy and complexes, nickel phosphide was shown, both theoretically and experimentally, to be a good HER catalyst.²⁷⁻²⁸ Nickel phosphide possesses a low overpotential (130 mV at 20 mA cm⁻²) and small Tafel slope (46 mV dec⁻¹).²⁸ This makes it comparable to the conventional HER electrocatalysts such as Pt and MoS₂.

Comparing with electrocatalytic HER, photo-driven HER is an attractive alternative to produce hydrogen gas because of the practically unlimited supply of solar energy. Solar spectrum composes of 5% ultra-violet radiation

and over 40% visible radiation, sharing large proportion of solar spectrum. Ultra-violet and visible radiations contains large amount of energy available which match to absorption energy of different light-absorbing substances to successfully catalyze HER. In order to utilize these radiations to drive HER, a photocatalytic system must be able to interact with radiation.¹⁶³ The captured photons in the semiconductors are used for the generation of electron-hole pairs for subsequent redox reactions. The types of radiation that can be absorbed are governed by the intrinsic band gap energy. Typical oxide semiconductors, such as zinc oxide (ZnO) and titanium dioxide (TiO₂), possess a large band gap (≥ 3 eV), thus can only absorb ultra-violet light.⁶⁴ Meanwhile, most of the metal chalcogenides, which have a narrower band gap energy (1-2.5 eV), are capable of absorbing visible light.¹⁶⁴ In addition, it is also crucial for the semiconductors to possess a proper band position.

The diversity of semiconducting material available for photocatalytic hydrogen evolution is limited by the band gap energy and band edge positions of semiconductors. To override this limitation, dye-sensitized photocatalytic system has been developed where organic or inorganic dyes are used as photosensitizers. By separating the roles of light absorption and catalytic center, a more diverse photocatalytic system can be constructed (Figure 3.1).

In this system, the only requirement for the catalyst is the activity toward HER. With less requirement on catalysts, there are more possible candidates to be employed. However, dye-sensitized system is less beneficial than single-component system since the stability of dye-sensitized system is related not only catalyst itself, but also dyes. A robust catalyst is needed to withdraw electron from the dye in excited state and prevents the bleaching of dye.

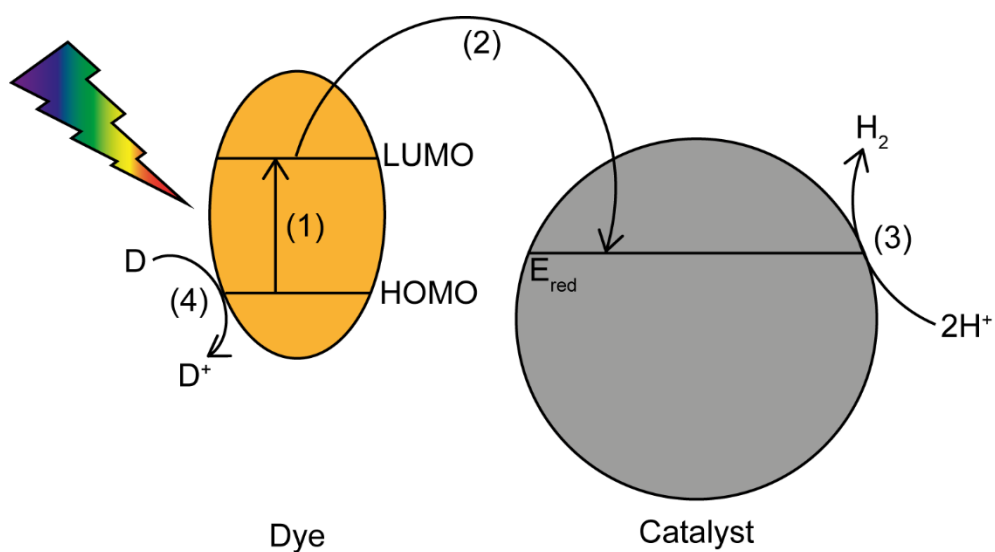


Figure 3.1. Schematic diagram of dye-sensitized photocatalytic generation. It possesses four sequential steps: (1) excitation of dye molecule upon illumination, (2) electron transfer from dye to catalyst, (3) generation of hydrogen gas from catalyst, and (4) restoring ground state of dye by oxidation of sacrificial agent.

Recently, nickel phosphide nanoparticle has demonstrated its excellent reactivity in electrocatalytic HER.²⁷⁻²⁸ The incorporation of foreign metal ions is known to induce a subtle alternation in the crystal and electronic structures of a nanoparticle. Platinum, as the most active catalyst for HER, is mixed with other metals to form alloys which showed enhancement in their activity. Bismuth-platinum alloy shows enhancement in activity of electrochemical HER both theoretically and experimentally.¹¹ Bismuth-platinum alloy has 50% larger current density than platinum under the same overpotential. Apart from Pt, nickel is subject to incorporate with different metals, including iron, molybdenum, and tungsten, to form the respective alloys. Through alloying, nickel alloy showed enhancement by altering the surface roughness and intrinsic activity of materials.¹⁶⁵ With the formation of bimetallic materials, changes happen on the configuration of active sites as well as modification on electronic structure.¹⁶⁵ This would result in an enhancement in the catalytic reactivity. Herein, the electrocatalytic HER activity of various metal-doped nickel phosphide nanoparticles, including iron, cobalt, manganese, and molybdenum, which described in the previous chapter are investigated. In addition, dye-sensitized photocatalytic HER systems based on these nanoparticles are also studied to show its diverse catalytic capability.

3.2 Materials and Experimental Procedures

3.2.1 Materials

Nafion solution (5 wt.%), potassium hydroxide, eosin Y (dye content ~99%), ruthenium(III) chloride hydrate, silver perchlorate, and silver trifluoromethanesulfonate were purchased from Aldrich. Triethanolamine was purchased from Tedia. All chemicals were used as received.

3.2.2 General Procedure for Working Electrode Preparation

Catalyst ink was prepared by dissolving 2.5 mg metal-doped nickel phosphide nanoparticles in a solution containing 460 μL ethanol-water mixture (3:7) and 40 μL 5 wt.% Nafion solution. Working electrode was prepared by drop-casting 10 μL of catalyst ink on glassy carbon electrode (GCE, $d = 3 \text{ mm}$, surface area = 0.0707 cm^2). The catalyst ink was dried naturally.

3.2.3 General Procedure for Electrocatalytic HER

Electrochemical measurements were performed using a CHI potentiostat (CHI1030A). Electrocatalytic hydrogen evolution reaction was conducted in a typical three-electrode system, using Pt mesh and saturated calomel

electrode (SCE) as the counter and reference electrode, respectively, in 1 M potassium hydroxide solution (pH = 13). The electrolyte solution was purged with Ar for 30 min before the electrochemical measurements to get rid of dissolved oxygen and provide inert atmosphere. Linear sweep voltammetry (LSV) was carried out in a potential range of -1 and -1.9 V with a scan rate of 5 mV/s. The potentials measurement against saturated calomel electrode (SCE) were converted with respect to the reverse hydrogen electrode (RHE) according to the following equation:¹⁶⁶

$$E_{\text{RHE}} = E_{\text{SCE}} + 0.244 + 0.0592(\text{pH}) \quad (7)$$

3.2.4 Synthesis of Ruthenium(II) bipyridine Complexes [Ru(bpy)₃]X₂ (X = Cl, ClO₄, or CF₃SO₃)

The synthesis of Ru(bpy)₃²⁺ complexes were carried out following the reported procedures with a slight modification.¹⁶⁷

[Ru(bpy)₃]Cl₂: To a 50 mL one-necked round bottom flask containing 7 mL DMF, RuCl₃·3H₂O (1.0 g, 8.8 mmol) and 2,2'-bipyridine (1.2 g, 7.6 mmol), and LiCl (1.1 g, 25.9 mmol) were added and refluxed under nitrogen for 8 h. The resulting solution was cooled to room temperature and put into a refrigerator overnight with the addition of acetone (32 mL) for crystallization.

The crystalline solids were collected by filtration, washed with iced water and diethyl ether, and dried under vacuum overnight. The product was characterized with electrospray ionization mass spectrometry (ESI-MS) and CHN elemental analysis and compared with reported literature.

[Ru(bpy)₃](ClO₄)₂: To a 50 mL one-necked round bottom flask containing ethylene glycol (10 mL), RuCl₃·3H₂O (0.27 g, 1.3 mmol) and 2,2'-bipyridine (1.25 g, 8 mmol) were added and refluxed under nitrogen for 1 h. The resulting red solution was cooled to room temperature, followed by the addition of excess amount of KClO₄ solid. Few drops of water were added in order to facilitate the precipitation. The resulting precipitate was collected by filtration, and washed with H₂O, acetone, and diethyl ether. The solids were dried under vacuum overnight and characterized with ESI-MS and CHN elemental analysis which well-matched with reported literature.

[Ru(bpy)₃](CF₃SO₃)₂: To a 25 mL one-necked round bottom flask containing 10 mL aqueous solution of [Ru(bpy)₃]Cl₂ (0.334 mmol, 0.025 g), a solution of Ag(CF₃SO₃) in acetone (0.098 M, 6.8 mL) was added. The resulting white precipitate (AgCl) was filtered by Celite. The filtrate was collected, and solvent was removed under vacuum. The resulting solids were characterized with ESI-MS and CHN elemental analysis.

3.2.5 General Procedure for Photocatalytic HER

5 mg of catalyst and 64 mg of dye were mixed in a 55-mL quartz flask containing 20 mL TEOA-DMF (15% v/v) solution. The solution was sonicated for 15 min to achieve a good dispersion and degassed with argon for 15 min afterwards. The flask was illuminated with a 450 W Xe lamp equipped with an AM1.5 filter (Newport OPSA1000) for 2 h. Gas generated in the headspace (250 mL) was withdrawn using air-tight syringe and analyzed using gas chromatograph equipped with thermal conductivity detector (GC-TCD, Agilent 7890B) and ValcoPLOT Molesieve 5Å PLOT column (CFS-X3053-500). The amount of H₂ generated was calculated based on the calibration curve. H₂ production rate was calculated based on the metal content of the catalyst determined by energy dispersive X-ray spectroscopy.

3.2.6 Photostability Test

The stability against photo-corrosion was tested out using NiMoP nanoparticle. The preparation of solution and analysis of hydrogen produced by photocatalysis are the same as in section 3.2.5 of this chapter. The duration of one photocatalysis run was set to 5 h and five consecutive runs were conducted. After each run, NiMoP nanoparticle was collected by

centrifugation and re-suspended in a fresh DMF solution with

$[\text{Ru}(\text{bpy})_3](\text{ClO}_4)_2$ and triethanolamine.

3.3 Results and Discussion

3.3.1 Electrocatalytic Hydrogen Evolution Reaction

The effect of metal doping in nickel phosphide nanoparticles in electrocatalytic HER was studied by measuring the linear sweep voltammograms (LSVs) from 0 to -0.8 V (vs. RHE, unless stated otherwise) in 1 M KOH aqueous solution (Figure 3.2). The overpotential for electrocatalytic HER is determined as potential required to reach a current density of 10 mA cm^{-2} . At this current density, HER is being catalyzed on a considerable rate, which is relevant to compare with different catalysts. The overpotential of pristine nickel phosphide (Ni_2P) nanoparticle was measured to be 0.71 V to reach a current density of 10 mA cm^{-2} . All the metal-doped nickel phosphide (NiMP , where $\text{M} = \text{Co}, \text{Fe}, \text{Mn}, \text{and Mo}$) nanoparticles showed the cathodic shifts of HER onset potential. The determined overpotentials at 10 mA cm^{-2} for Fe, Co, Mn, and Mo-doped nickel phosphide (abbreviated as NiFeP, NiCoP, NiMnP, and NiMoP) nanoparticles are 0.69, 0.53, 0.49, and 0.4 V, respectively. These decreased overpotential values indicate that the metal doping enhances the catalytic activity of nickel phosphide by lowering the energy required to drive HER. Especially, Mo-doping has lowered the overpotential by more than

0.3 V, suggesting NiMoP nanoparticle can be an active electrocatalyst for HER.

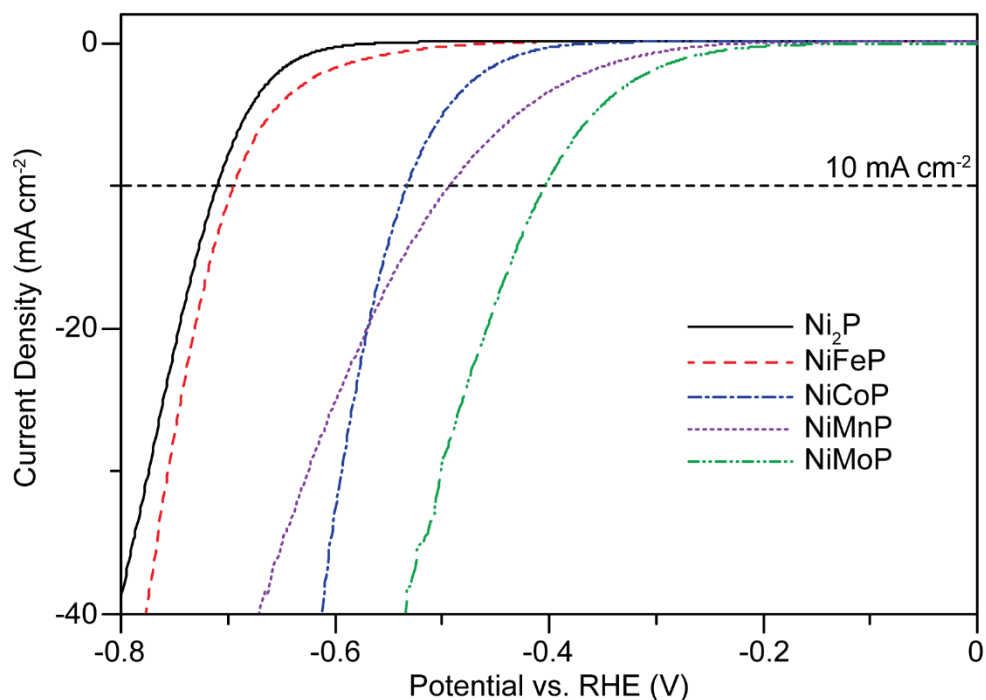


Figure 3.2. Linear sweep voltammograms of Ni₂P and various NiMP nanoparticles in 1 M KOH.

In order to gain more information on the kinetics, the corresponding Tafel plots were constructed using the LSV data and shown in Figure 3.3. All the samples investigated show relatively large Tafel slopes (>100 mV dec⁻¹). These slopes indicate the rate determining step is associated with Volmer step where the adsorption of hydrogen on catalyst surface is involved. The result is consistent with the calculations using density functional theory (DFT) by Liu and Rodriguez²⁷ in which the Ni₂P nanoparticle has a positive value of

Gibbs free energy of hydrogen adsorption ($\Delta G_H = 0.31$ eV), and its surface intrinsically favors hydrogen desorption rather than adsorption.

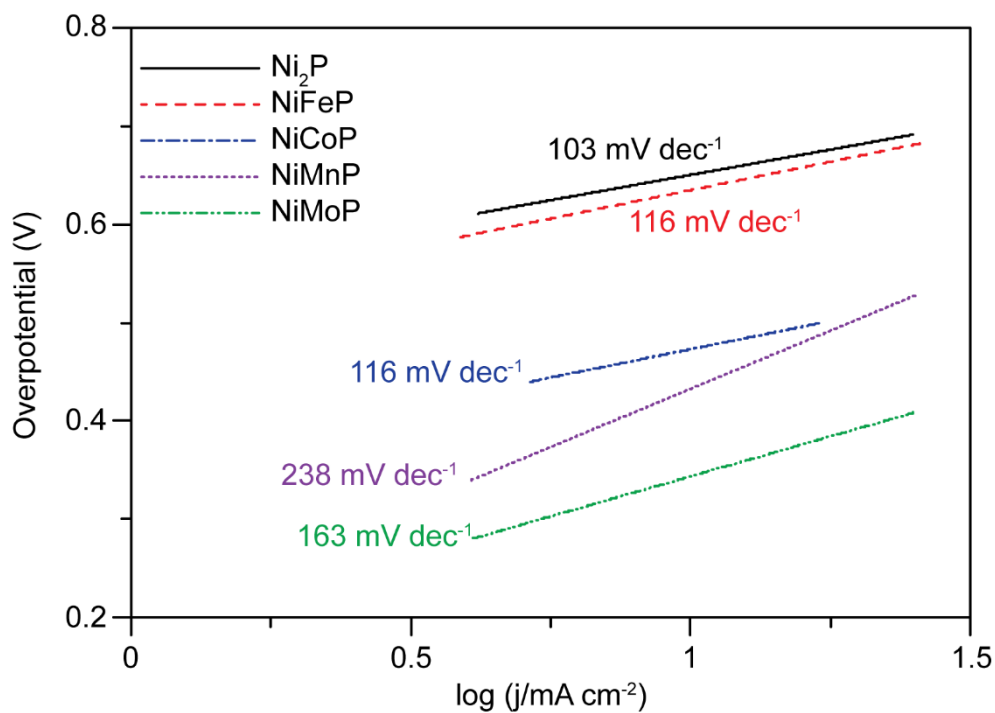


Figure 3.3. Tafel plots of Ni₂P and various NiMP nanoparticles.

In addition to the overpotential and Tafel slope, the exchange current density is also an important kinetic parameter to determine how active a catalyst is. Exchange current density (j_0) can be estimated from the Tafel plot using the following equation:

$$\eta = b \left(\log \frac{j}{j_0} \right) \quad (8)$$

where η is overpotential, b is Tafel slope, j is current density, and j_0 is exchange current density. Although Ni₂P nanoparticle has the smallest Tafel

slope which indicates more efficient hydrogen adsorption on catalyst surface compared with NiMP nanoparticles, its lowest exchange current density ($1.3 \times 10^{-6} \text{ mA cm}^{-2}$) among studied samples explains a high overpotential is required to drive HER (Table 3.1). NiFeP and NiCoP nanoparticles show slightly better electrocatalytic properties than Ni₂P nanoparticle in both overpotential and exchange current density. NiMnP and NiMoP nanoparticles, however, show much higher exchange current density, 0.08 and 0.03 mA cm⁻², respectively. Even though their Tafel slopes are higher than Ni₂P, the dramatic increases in the exchange current densities by about five orders of magnitudes make them better electrocatalysts. Based on the overpotential, Tafel slope, and exchange current density, electrocatalytic activity of nickel phosphide-based catalysts follows the order below:



Table 3.1. Summary of electrochemical parameters of Ni₂P and various NiMP nanoparticles

	Overpotential at 10 mA cm ⁻² (V)	Tafel Slope (mV dec ⁻¹)	Exchange Current Density (mA cm ⁻²)
Ni ₂ P	-0.71 (1)	103 (1)	$1.3 (1) \times 10^{-6}$
NiFeP	-0.69 (2)	116 (3)	$1.0 (1) \times 10^{-5}$
NiMnP	-0.49 (2)	237 (1)	$8 (1) \times 10^{-2}$
NiCoP	-0.53 (1)	116 (4)	$2.5 (1) \times 10^{-4}$
NiMoP	-0.40 (2)	163 (4)	$3 (1) \times 10^{-2}$

From the above electrochemical analysis, Mo doping in nickel phosphide crystal lattice largely improved the electrocatalytic property for HER. Numerous researches have employed nickel-molybdenum alloy as HER electrocatalysts.^{14, 165, 168} The enhancement in catalytic property is resulted by introducing foreign metals. Combination of metals can possibly lead to changes in bonding strength as well as the electronic configuration. Dramatic change can be achieved by alloying transition metal having empty or half-filled d-orbital (such as Mo and W) and internally paired d-electrons (such as Ni, Pd, and Pt).^{165, 169} Through combining the two, *d*-electrons from Ni can partially delocalize to *d*-electron deficient Mo. This results in intermetallic property which is beneficial in electrocatalytic HER. Mo, as the most *d*-electron deficient component among all samples, shows the largest enhancement through incorporation in nickel phosphide crystal lattice. For the other three first-row transition metals, it shows trend where the reactivity increases with decreasing number of *d*-electrons in foreign metals (Ni₂P < NiFeP < NiCoP < NiMnP).

Platinum is known to be the best hydrogen-evolving catalyst, having an extremely low Tafel slope (30 mV dec⁻¹) and high exchange current density ($\sim 1 \times 10^{-3}$ A cm⁻²) in acidic medium. Meanwhile, detailed electrochemical

measurements were carried out to study catalytic activity of noble metals towards hydrogen evolution reaction in alkaline medium.¹⁷⁰ Rate determining step using Pt in electrochemical HER under alkaline medium is changed to be Volmer step as rate determining step which will have a theoretical Tafel slope of 120 mV dec^{-1} . Comparing the best electrocatalyst prepared (NiMoP), activity is close to Pt where the exchange current densities of them are in the same magnitude and a slightly higher Tafel slope (163 mV dec^{-1}).

3.3.2 Dye-sensitized Photocatalytic Hydrogen Evolution Reaction

A catalytic system that can directly utilize sunlight to drive the HER is considered to be renewable as there is unlimited supply of solar energy. In the previous section, NiMP nanoparticles were proven to have excellent catalytic properties for HER, and this can be considered to be constructed into a photocatalytic system. However, since NiMP nanoparticles only possess metallic property according to VB-XPS analysis, they cannot absorb photons and utilize their energy for catalysis. To solve this problem, a dye-sensitized photocatalytic HER system was constructed based on the NiMP nanoparticles where either tris(2,2'-bipyridyl)ruthenium(II) perchlorate ($[\text{Ru}(\text{bpy})_3](\text{ClO}_4)_2$) or eosin Y (Figure 3.4 and Figure 3.5, respectively) are engaged as a photosensitizer. Tris(bipyridine)ruthenium(II) ions ($[\text{Ru}(\text{bpy})_3]^{2+}$) has the characteristic absorption in ultraviolet and visible region.

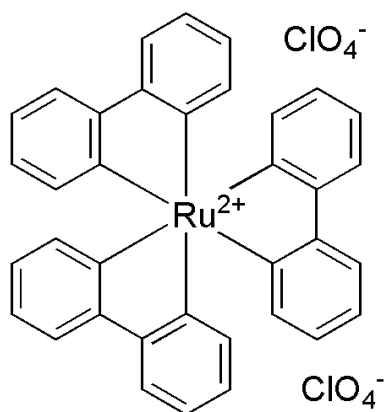


Figure 3.4. Structure of tris(2,2'-bipyridyl)ruthenium(II) perchlorate $\text{Ru}(\text{bpy})_3(\text{ClO}_4)_2$.

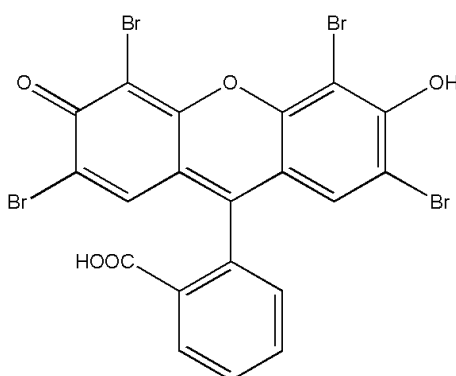


Figure 3.5. Chemical structure of eosin Y.

Researchers have employed $[\text{Ru}(\text{bpy})_3]^{2+}$ and its derivatives to carry out photocatalytic HER.¹⁷¹⁻¹⁷⁵ $[\text{Ru}(\text{bpy})_3](\text{ClO}_4)_2$ possesses different absorption peaks, including ligand-centered transition (LC), *d-d* transition (MC) and metal-to-ligand charge transfer (MLCT) (Figure 3.6). MLCT transition occurs in the visible region (455 nm) with high extinction coefficient which allows it to function as a photosensitizer in photocatalytic HER.¹⁷⁶ Similar to $[\text{Ru}(\text{bpy})_3](\text{ClO}_4)_2$, eosin Y possesses a high absorptivity in visible region at

516 nm that allows its wide application as photosensitizer (Figure 3.7).¹⁷⁷⁻¹⁷⁹

In addition, it is more soluble than $[\text{Ru}(\text{bpy})_3](\text{ClO}_4)_2$ in water which allows reaction to be carried out in water only, a greener reaction condition of photocatalytic HER.

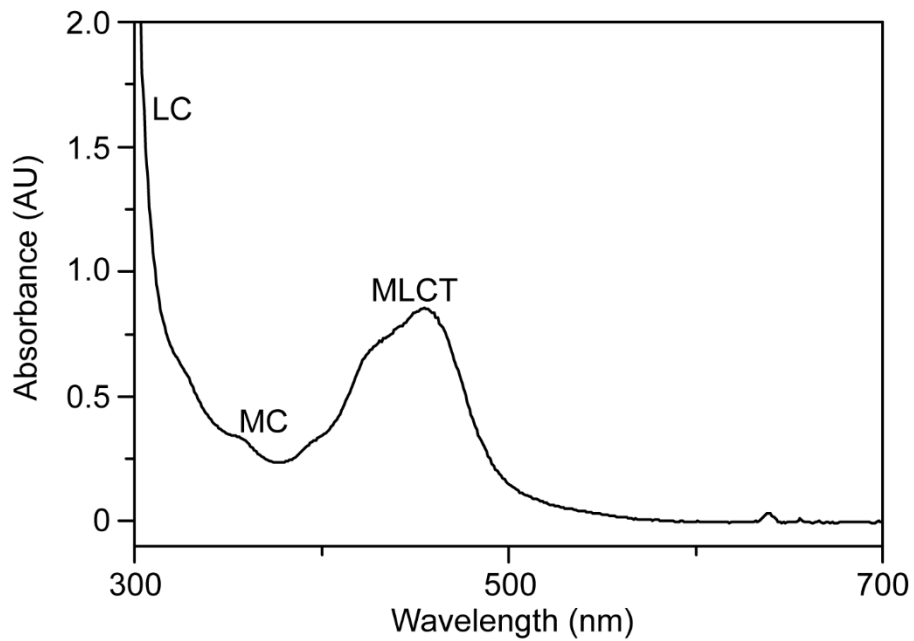


Figure 3.6. Typical UV-visible spectrum of $[\text{Ru}(\text{bpy})_3](\text{ClO}_4)_2$.

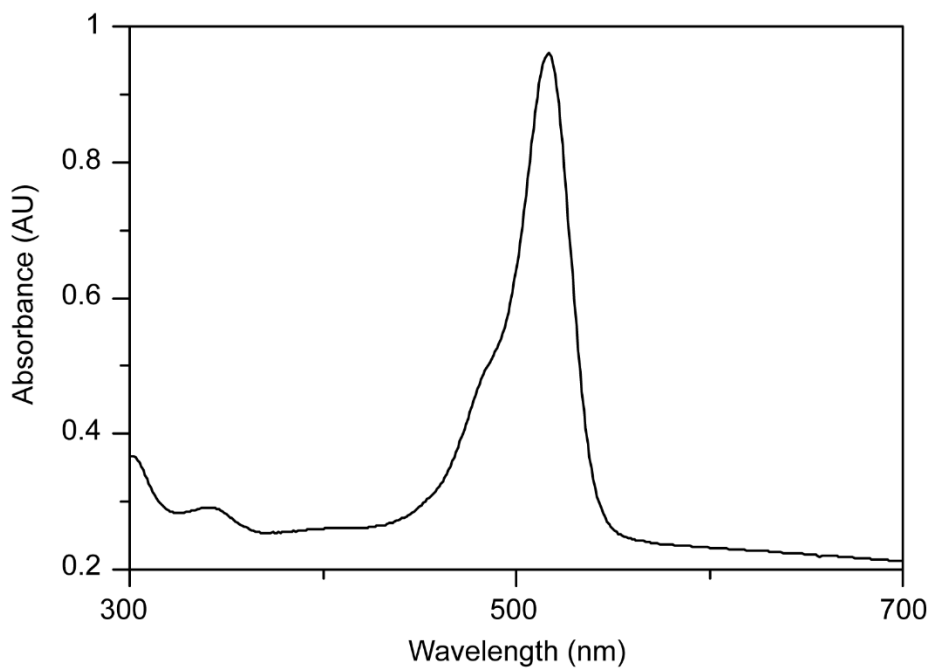


Figure 3.7. Typical UV-visible spectrum of eosin Y.

3.3.2.1 Ru(bpy)₃²⁺-sensitized Photocatalytic Hydrogen Evolution Reaction

Photocatalytic HER was carried out using [Ru(bpy)₃]²⁺-sensitized system. Triethanolamine (TEOA) was used as sacrificial agent to regenerate the ground state of [Ru(bpy)₃]²⁺ after excitation upon illumination as well as a proton source.¹⁸¹ Illumination of NiFeP nanoparticles in the presence of [Ru(bpy)₃](ClO₄)₂ in N,N'-dimethylformamide (DMF) using 450 W solar simulator with air mass 1.5 filter for one hour resulted in the formation of 486 μmol of H₂. In the two control experiments conducted under the same experimental conditions, only small amount of H₂ (24 μmol) was detected with the presence of [Ru(bpy)₃](ClO₄)₂ only, while no H₂ was detected with NiFeP nanoparticles only (Figure 3.8). These results confirm that NiFeP nanoparticles alone cannot carry out the photocatalytic HER, but they can catalyze the HER with excellent reactivity with the assistance of a light absorber, [Ru(bpy)₃](ClO₄)₂. It demonstrates that the excitons generated in [Ru(bpy)₃](ClO₄)₂ are effectively transferred to NiFeP nanoparticle, where they are used to catalyze the HER.

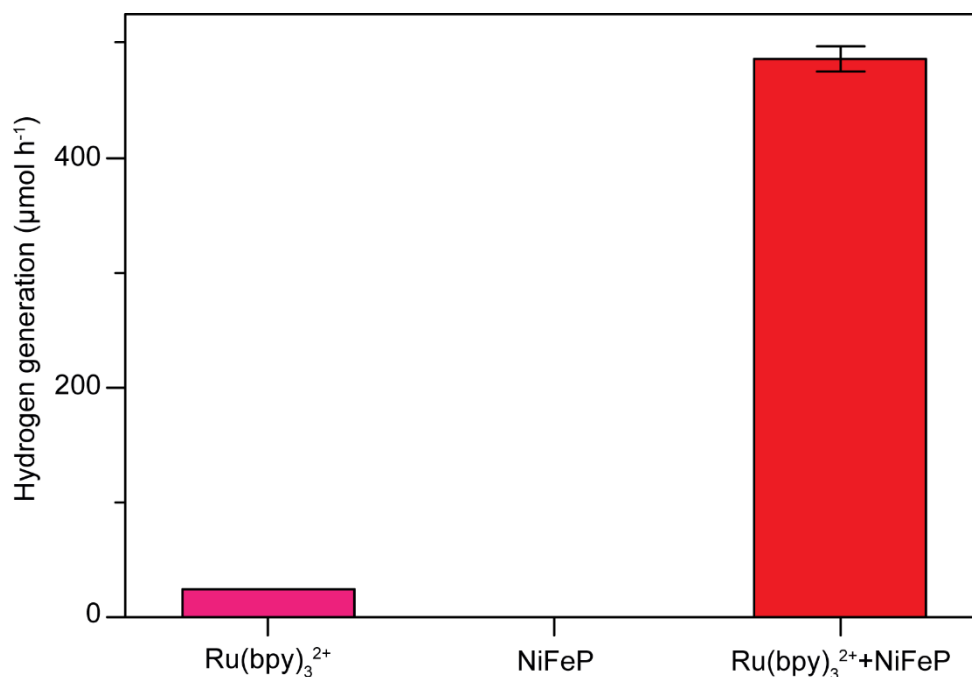


Figure 3.8. Comparison of the amount of H₂ generated in the presence of [Ru(bpy)₃](ClO₄)₂ only, NiFeP nanoparticle only, and both [Ru(bpy)₃](ClO₄)₂ and NiFeP nanoparticle.

In order to understand the effect of metal doping in nickel phosphide nanoparticles in photocatalytic HER, the reactivities of other NiMP nanoparticles were also studied (Figure 3.9). In general, metal doping in nickel phosphide nanoparticles shows a positive effect on the performance in dye-sensitized photocatalytic HER. Ni₂P nanoparticle produces H₂ at a rate of 174 mmol h⁻¹ g⁻¹, while NiFeP, NiCoP, NiMnP, and NiMoP nanoparticle all show a higher hydrogen production rate of 189, 210, 259, and 268 mmol h⁻¹ g⁻¹, respectively. The rank of photocatalytic activity is as follow:



The order of photocatalytic activity of Ni₂P and different NiMP nanoparticles is identical to the decreasing order of overpotential for electrochemical hydrogen evolution. The identical trend in HER catalytic activity is attributed to the active site on catalyst surface. NiMP nanoparticles in dye-sensitized photocatalytic system act as reaction center only. They receive electrons from excitation of dye and conduct HER. Since NiMP nanoparticles do not participate in other crucial steps for complete cycle of photocatalytic HER, activity towards HER is primarily dependent on intrinsic property of active site in catalyst which makes the trend in photocatalytic and electrocatalytic HER the same.

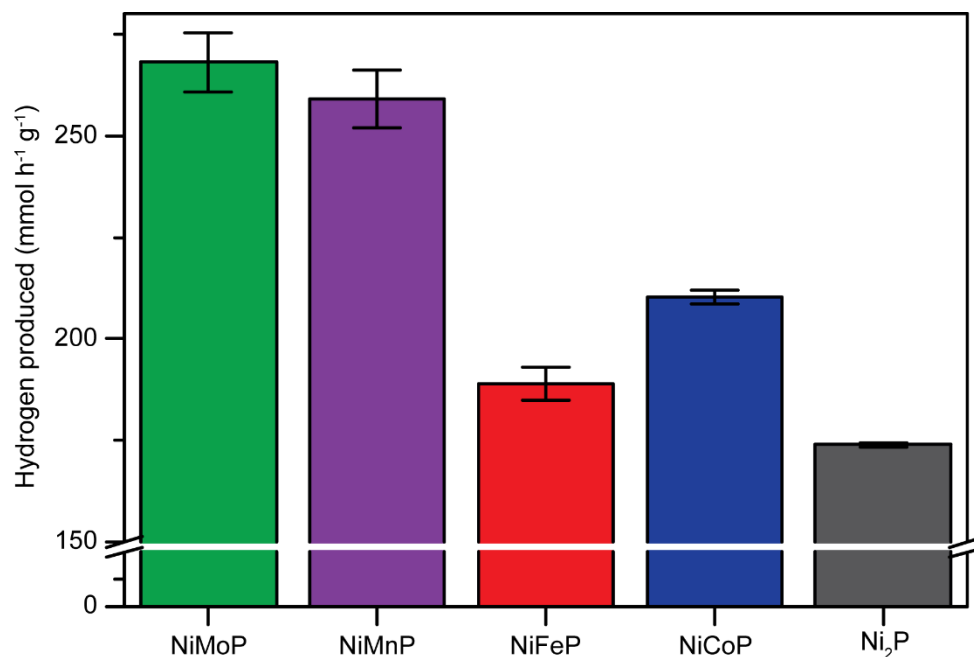


Figure 3.9. Photocatalytic activity of Ni₂P and various NiMP nanoparticles.

In order to further investigate the effect of metal doping on photocatalytic HER rate, the nickel-to-cobalt ratio has been varied. For systematic study, the nickel-to-cobalt precursor ratio was varied from 3:1 to 1:2 during the synthesis of NiCoP nanoparticles and their corresponding hydrogen production rates were measured (Figure 3.10). The optimal Ni:Co precursor ratio was found to be 1:1 which showed the largest H₂ production rate of 209 mmol h⁻¹ g⁻¹. Lowering cobalt loading led to a decrease in H₂ producing ability. NiCoP nanoparticles synthesized under Ni:Co ratio 2:1 and 3:1 (abbreviated as NiCoP21 and NiCoP31) showed the H₂ production rate of 180 and 147 mmol h⁻¹ g⁻¹, respectively. On the other hand, further increase in cobalt loading more than 1:1 did not enhance the H₂ production anymore.

NiCoP nanoparticle synthesized with 1:2 Ni:Co precursor ratio (NiCoP12) has a H_2 production rate of $140 \text{ mmol h}^{-1} \text{ g}^{-1}$ which is lower than one synthesized with 1:1 Ni:Co ratio. The hydrogen production rate is possibly related to the degree of delocalization of d -electrons as discussed previously in this chapter. NiCoP nanoparticle synthesized with 1:1 Ni:Co precursor ratio (NiCoP11) is believed to have the largest degree of d -electron delocalization and thus the highest H_2 production rate.

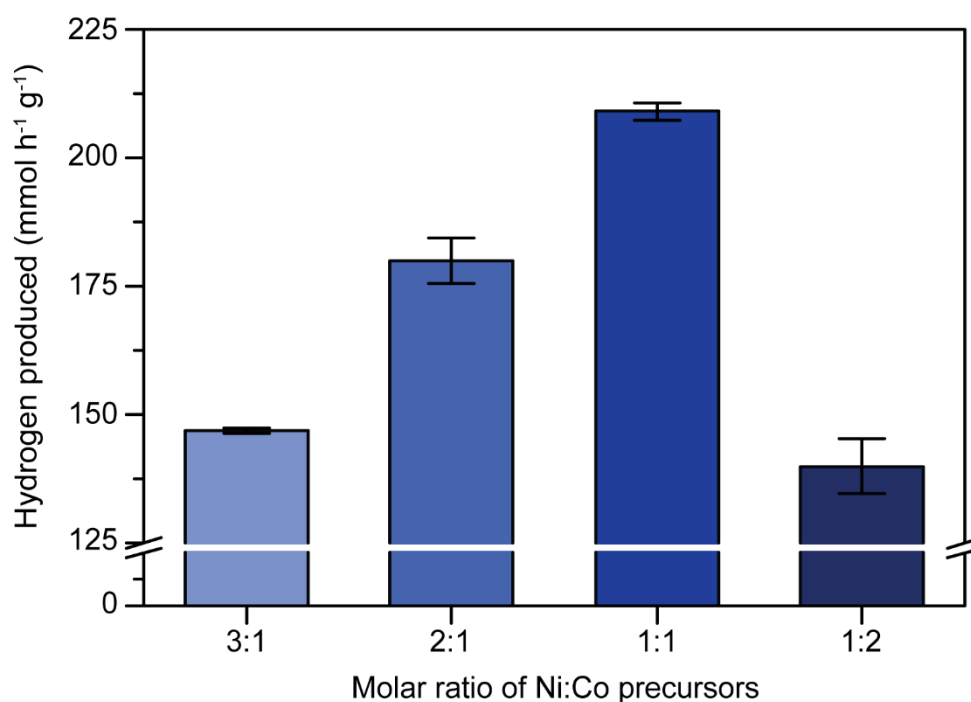


Figure 3.10. Effect of nickel-to-cobalt precursor ratio on hydrogen production.

The enhancement on photocatalytic HER by metal doping on nickel phosphide can be explained by the degree of delocalization of d -electrons

within metals. From the study of variation of nickel-to-cobalt ratio, it is clearly that there is an optimal precursor ratio between two metals which can maximize *d*-electron delocalization (1:1 in the case of NiCoP nanoparticle). Moreover, extent of metal incorporation in nickel phosphide crystal lattice through wet chemical method is highly dependent on similarity between foreign metal ion and nickel ion.

The photocatalytic system was further optimized using NiFeP nanoparticle as the catalyst. Effect of $[\text{Ru}(\text{bpy})_3]^{2+}$ concentration on H_2 production rate was investigated (Figure 3.11). The H_2 production rate initially increased with $[\text{Ru}(\text{bpy})_3]^{2+}$ concentration and reached a plateau (189 $\text{mmol h}^{-1} \text{g}^{-1}$) at the $[\text{Ru}(\text{bpy})_3]^{2+}$ concentration of 4 mmol L^{-1} . NiFeP nanoparticle is not fully engaged for HER catalysis at the $[\text{Ru}(\text{bpy})_3]^{2+}$ concentration lower than 4 mmol L^{-1} . Further increase in $[\text{Ru}(\text{bpy})_3]^{2+}$ concentration did not lead to the increase in H_2 production rate. Under such conditions, the HER rate is no longer limited by the number of excited electrons.

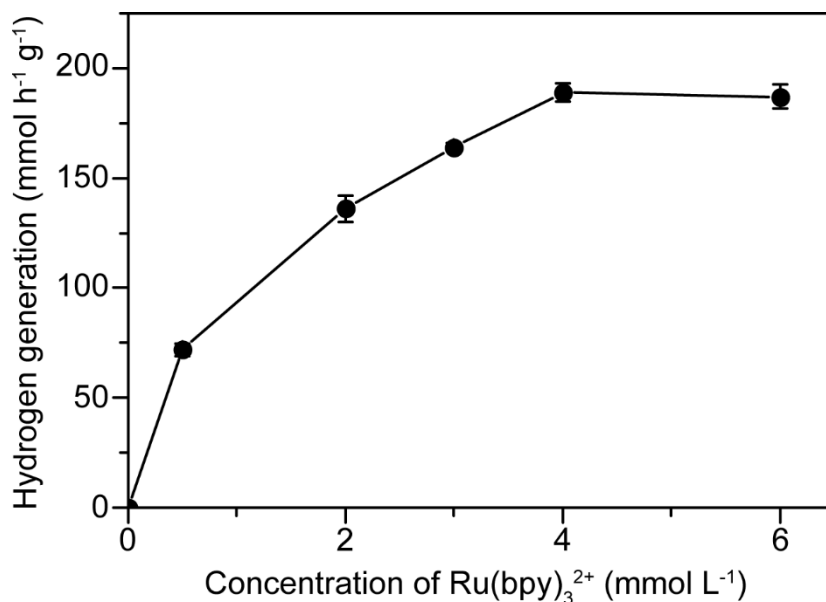


Figure 3.11. Relation between photocatalytic activity and concentration of $[\text{Ru}(\text{bpy})_3]^{2+}$ using NiFeP nanoparticle as catalyst.

The solvent used in the $[\text{Ru}(\text{bpy})_3^{2+}]$ -sensitized photocatalytic system is DMF, which has drawbacks of insufficient number of protons for reduction and environmental susceptibility. Water has been added in order to increase the number of protons and reduce the volume of organic solvent used. However, with water added into the system, the photocatalytic activity dropped. Further increase in the amount of water added into the solvent resulted in a continuous dropping in the rate of H_2 generation (Figure 3.12). This is mainly due to the perchlorate, the counter ion of $\text{Ru}(\text{bpy})_3^{2+}$, which makes photosensitizer not soluble in water. With increased addition of water, the available photosensitizer in solution diminished and thus the catalytic H_2 generation dropped to zero.

Apart from solubility, the intrinsic photochemical property of photosensitizer changes in different solvents.¹⁸² Meyer and Caspar studied the lifetime of excited $\text{Ru}(\text{bpy})_3(\text{PF}_6)_2$ in various solvents. The excited state of $\text{Ru}(\text{bpy})_3(\text{PF}_6)_2$ has a lifetime of $0.912 \mu\text{s}$ in DMF which gets shortened to $0.630 \mu\text{s}$ in water. It clearly shows the effect of solvent on the excitation of $\text{Ru}(\text{bpy})_3^{2+}$ and the lifetimes in different solvents which can lead to reduction of electron transfer from photosensitizer to catalyst for subsequent hydrogen production.

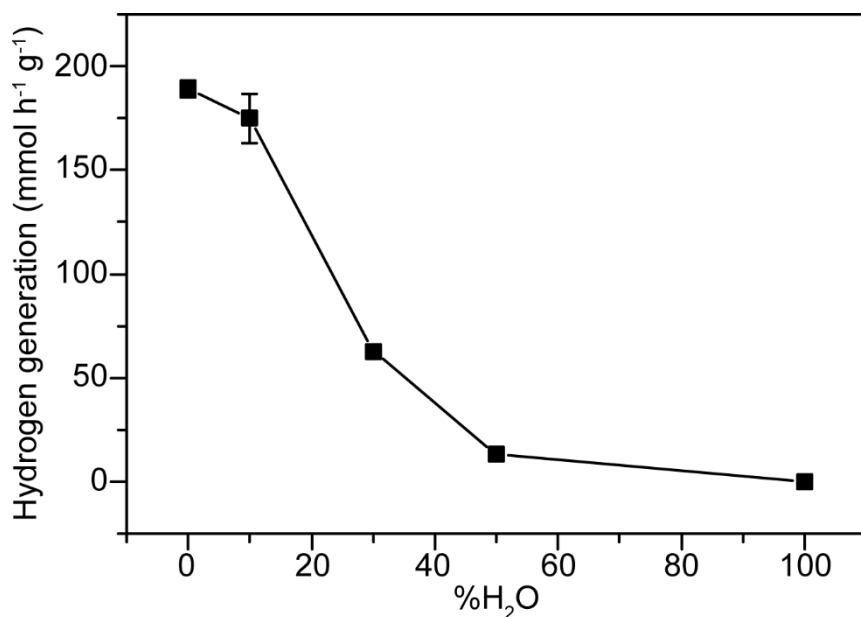


Figure 3.12. Photocatalysis in solvent with different water-to-DMF ratio using NiFeP nanoparticle as catalyst.

In order to solve the solubility problems of the Ru photosensitizer in water, the anion of $[\text{Ru}(\text{bpy})_3](\text{ClO}_4)_2$ was replaced with trifluoromethanesulfonate (triflate, OTf^-) and chloride (Cl^-) ions, both of which have higher solubility in water. The catalytic performances of NiFeP using different Ru photosensitizers in the presence of water were evaluated by conducting the reaction in a 1:1 mixture of water and DMF (Figure 3.13). Although both Cl^- and OTf^- complexes have better water solubility than the ClO_4^- complex, the rate of H_2 generation is much lower compared to the reactions in DMF ($13.4 \text{ mmol h}^{-1} \text{ g}^{-1}$), which yielded 1.8 and $4.1 \text{ mmol h}^{-1} \text{ g}^{-1}$, respectively. These results may be explained by the differences in the light absorptivity of Ru complexes. From their UV-visible absorption spectra,

[Ru(bpy)₃](ClO₄)₂ shows the highest absorption from MLCT transition band following by triflate and chloride ions (Figure 3.14). The catalytic activity of Ru complexes with different counter ions is closely correlated with absorbance in UV-visible spectrum, which indicates that the light-capturing ability depends upon the counter ions as well as solubility of photosensitizers.

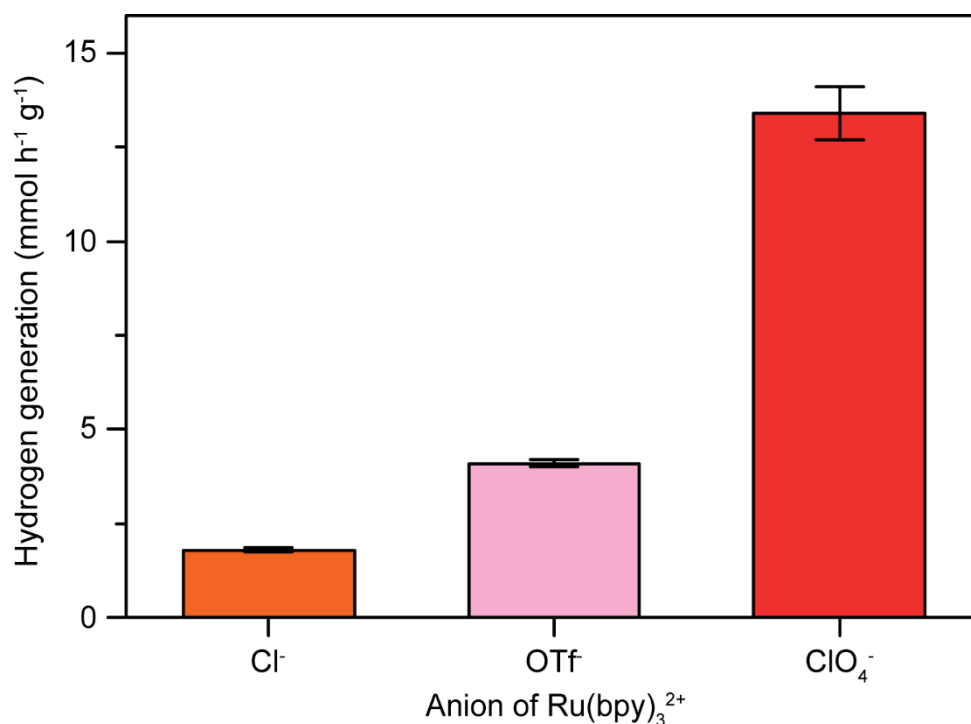


Figure 3.13. Photocatalytic HER performance of NiFeP nanoparticle using Ru(bpy)₃X₂ (X = ClO₄⁻, CF₃SO₃⁻, Cl⁻) as photosensitizers in a mixture of H₂O–DMF (1:1) using NiFeP nanoparticle as catalyst.

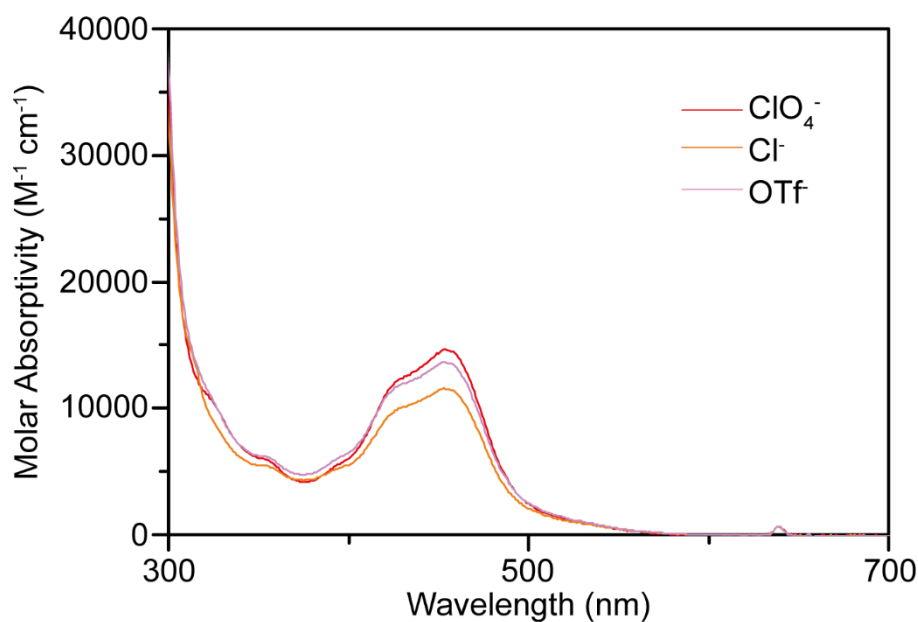


Figure 3.14. UV-Visible absorption spectra of $\text{Ru}(\text{bpy})_3\text{X}_2$ ($\text{X} = \text{ClO}_4^-$, OTf^- , Cl^-) in H_2O – DMF (1:1) solution.

In addition to efficiency and activity, stability is another important parameter for evaluating a photocatalyst. Stability test for NiMoP nanoparticle was carried out in the $\text{Ru}(\text{bpy})_3^{2+}$ -sensitized photocatalytic system (Figure 3.15). The test was done in five separate runs of 5 h for the total duration of 25 h. After each run, NiMoP nanoparticle was isolated and photosensitizer and sacrificial agent were replenished. NiMoP nanoparticle shows a good stability during the photocatalytic HER. The difference in photogenerated hydrogen from the first and fifth runs are less than 500 mmol, which indicates NiMoP nanoparticle retains nearly 80% of its activity over a 25-hour reaction.

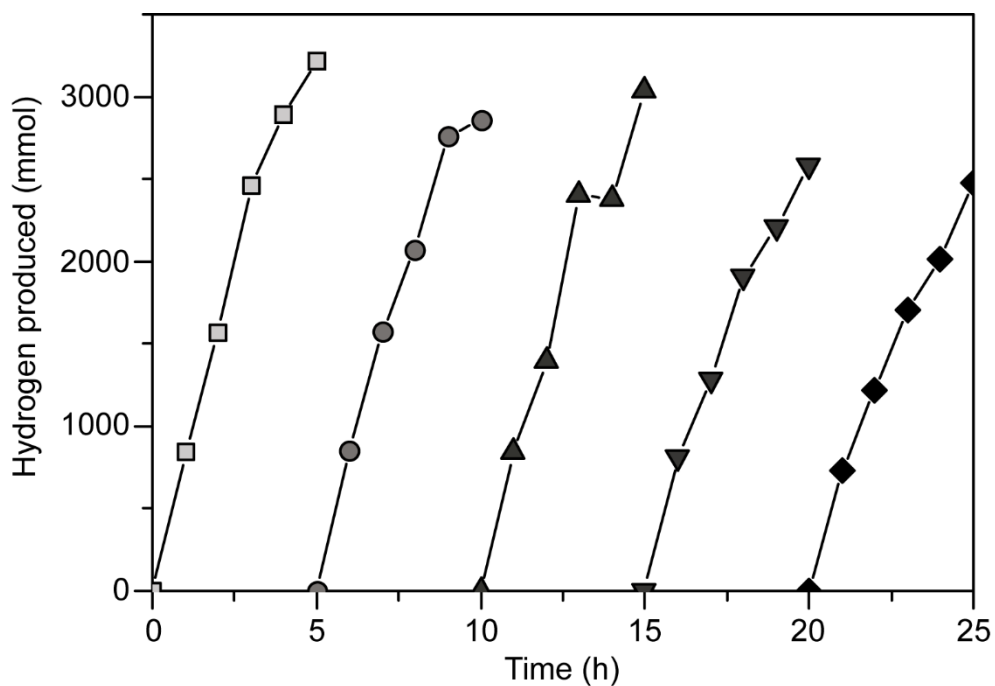


Figure 3.15. Stability test on NiMoP nanoparticle in $\text{Ru}(\text{bpy})_3^{2+}$ -sensitized photocatalytic HER. Catalysis was carried out for 5 h in each run. After a single run, catalyst was collected by centrifugation and re-dispersed in freshly-prepared TEOA-DMF solution with $\text{Ru}(\text{bpy})_3^{2+}$ photosensitizer.

3.3.2.2 Eosin Y-sensitized Photocatalytic Hydrogen Evolution Reaction

Although the $[\text{Ru}(\text{bpy})_3]^{2+}$ -sensitized NiMP systems show excellent performance in photocatalytic HER, Ru-based photosensitizers and DMF are toxic and harmful to the environment. A series of more environmental friendly photosensitizers have been tested to replace ruthenium complexes, including eosin Y,¹⁸³⁻¹⁸⁶ and fluorescein-based dyes.¹⁸⁷ Eosin Y contains carboxyl and hydroxyl functional groups that can be easily deprotonated to form an anion, and thus is highly soluble in water. Besides, it is cheaper, less toxic, and easier to handle than Ru complexes, which makes it a preferable choice as a photosensitizer.

Using the same experimental conditions except for eosin Y as a photosensitizer, the photocatalytic performance of NiFeP nanoparticle was studied and the results are shown in Figure 3.16. In the control experiments where only eosin Y or NiFeP nanoparticle was engaged, only trace amounts of H_2 ($< 1 \mu\text{mol h}^{-1}$) were generated. In contrast, in the presence of both eosin Y and NiFeP nanoparticle, the photocatalytic system generated H_2 in a rate of $44 \mu\text{mol h}^{-1}$, which is nearly 50 times higher than the control experiments. This shows that there is an efficient photo-excited electron transfer from eosin Y to NiFeP nanoparticle, giving

rise to a good catalytic activity towards HER.

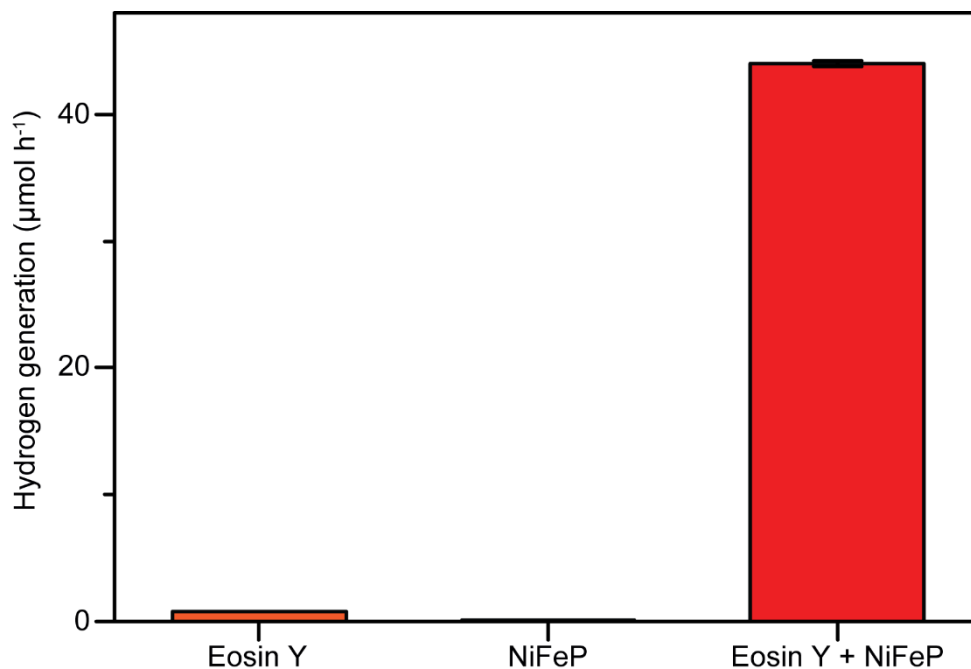


Figure 3.16. Photocatalytic HER performance of NiFeP nanoparticle using eosin Y as the photosensitizers in the system. The results of the solely presence of eosin Y, and NiFeP nanoparticle in the system are also included for comparison.

The photocatalytic performances in HER of other NiMP nanoparticles were also studied with eosin Y and the results are compared in Figure 3.17. NiCoP nanoparticle shows the best catalytic performance with the H_2 production rate of $20.4 \text{ mmol h}^{-1} \text{ g}^{-1}$.

It is of interest to note that the trend of catalytic performance amongst the NiMP nanoparticles is different from the results obtained with $[\text{Ru}(\text{bpy})_3](\text{ClO}_4)_2$ as the photosensitizers. Ru complex and eosin Y-sensitized

photocatalytic HER was carried out in DMF and water, respectively, where the proton concentration as well as hydrogen coverage on catalyst surface are different from each other. Studies were conducted on the effect of hydrogen coverage on Gibbs free energy of hydrogen adsorption (ΔG_H) show an increase in ΔG_H with increasing hydrogen coverage.¹⁸⁸⁻¹⁸⁹ ΔG_H is a thermodynamic parameter describing the affinity towards hydrogen adsorption. Since the adsorbed hydrogen on catalyst surface is the key intermediate for HER, ΔG_H is an indicator for activity estimation. HER is most favorable on catalyst with moderate ΔG_H value. The difference between two dye-sensitized photocatalytic systems possibly arises from different degree of hydrogen coverage on catalyst surface during catalysis. The change to a suitable photosensitizer allowed the use of NiMP nanoparticles for the photocatalytic hydrogen evolution reaction in aqueous medium.

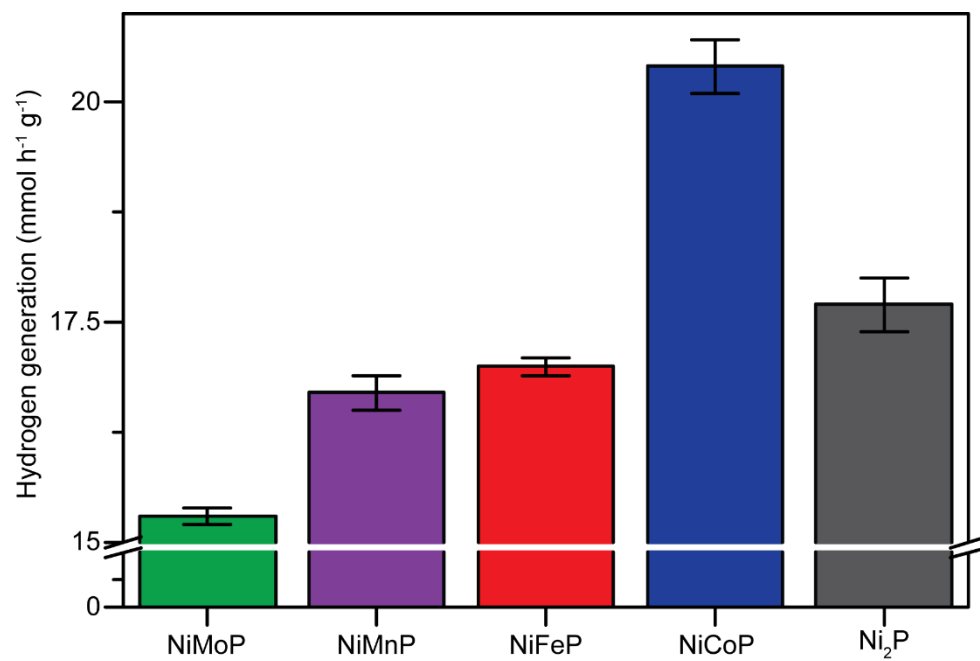


Figure 3.17. Photocatalytic HER performance of Ni₂P and different NiMP nanoparticles using eosin Y as the photosensitizer in H₂O.

3.4 Conclusion

The excellent catalytic performances of nickel phosphide nanoparticles with various metal dopants in both electro- and photochemical HER were demonstrated. In general, metal-doped nickel phosphide nanoparticles show a higher catalytic activity than pristine nickel phosphide nanoparticle. Molybdenum-doped nickel phosphide nanoparticle was found to have the lowest overpotential of 0.34 V vs. RHE and a Tafel slope of 163 mV dec⁻¹ in alkaline medium.

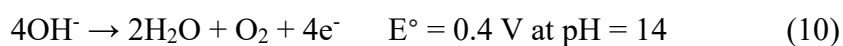
Metal-doped nickel phosphide nanoparticles also show promising activity in the dye-sensitized photocatalytic hydrogen evolution reaction. Molybdenum-doped nickel phosphide nanoparticle shows excellent activity on hydrogen production with a rate of 268 mmol h⁻¹ g⁻¹ in the presence of [Ru(bpy)₃](ClO₄)₂ in DMF. Photocatalytic hydrogen evolution reaction can also be carried out in aqueous medium using eosin Y as a photosensitizer. Cobalt-doped nickel phosphide nanoparticle exhibited the best hydrogen production rate of 20.4 mmol h⁻¹ g⁻¹ in eosin Y-sensitized photocatalytic system among the samples studied.

Chapter 4 Metal-doped Nickel Phosphide Nanoparticles in Electrocatalytic Oxygen Evolution Reaction (OER)

4.1 Introduction

Water splitting provides an attractive pathway to produce renewable and sustainable energy sources. Hydrogen and oxygen gases are produced by water reduction and oxidation, respectively. Conventionally, this can be achieved by alkaline water electrolysis where cathodic and anodic reactions occur in the separate compartments divided by an ion-permeable membrane.¹⁹⁰ Product gases, hydrogen and oxygen, are collected separately for further use in different sectors in society. Therefore, not only hydrogen evolution reaction, electrochemical oxygen evolution reaction (OER) is worthwhile being studied as another half reaction to complete the entire cycle in alkaline water electrolysis or water splitting reaction.

Electrochemical OER is a multistep reaction of which the mechanism is pH-dependent. The oxygen gas can be formed by the oxidation of water molecules and hydroxide ions in acidic and alkaline media, respectively, following the equation below.



Under both acidic and alkaline conditions, the OER involves transfer of four electrons. To accomplish this four-electron transfer, it is kinetically more favorable to conduct the OER in multiple steps, with one electron being transferred each time. From the thermodynamic aspects, these four sequential electron transfer steps require substantial amount of energy, which needs a large overpotential in electrochemical OER. Compared to the hydrogen evolution reaction (HER), OER is both kinetically and thermodynamically less favorable with sluggish kinetics and high overpotential required.¹⁹⁰⁻¹⁹²

Researchers devoted much effort to develop robust OER electrocatalysts with fast kinetics and low overpotential. The benchmark OER electrocatalysts are ruthenium dioxide (RuO_2) and iridium dioxide (IrO_2).⁸⁰⁻⁸¹ These two oxide materials provide low overpotential in electrochemical OER which makes them suitable to be OER electrocatalysts. However, their scarcity and high cost make them unfavorable for commercial uses. With the pioneering works on RuO_2 and IrO_2 , other oxide materials are explored as a class of potential OER electrocatalysts, especially for the development of robust and economic OER electrocatalysts based on transition metal oxides.¹⁹³ Various classes of oxygen-containing materials including perovskites,⁸²⁻⁸⁴ spinel family,⁸⁵⁻⁸⁸ and layered double hydroxides⁸⁹⁻⁹³ are being investigated for their

potency to carry out electrochemical OER. The search has been recently extended to non-oxide materials, such as metal chalcogenides.⁹⁴⁻⁹⁶

Recently, nickel phosphide nanoparticle has found to be an active electrocatalyst for OER. Surface nickel phosphide is *in situ* converted into the catalytically-active nickel oxyhydroxide species which shows good activity towards electrochemical OER.⁹⁷ This has opened a new era on employing transition metal phosphides as OER electrocatalysts. Metal-doped nickel phosphide nanoparticles have demonstrated their capability and excellent catalytic activity in electrocatalytic and photocatalytic HER in the previous chapter. With simple modification of catalyst surface, metal-doped nickel phosphide nanoparticles were prepared to have different surface chemistry as well as activities toward electrochemical OER. Herein, various metal-doped nickel phosphide nanoparticles are investigated for their electrocatalytic activity on OER in alkaline medium.

4.2 Material and Experimental Procedures

4.2.1 Materials

Nafion solution (5 wt.%) and potassium hydroxide were purchased from Aldrich. All chemicals were used as received.

4.2.2 General Procedure for Working Electrode Preparation

Catalyst ink was prepared by dissolving 2.5 mg metal-doped nickel phosphide nanoparticles in a solution containing 460 μL ethanol-water mixture (3:7) and 40 μL 5 wt.% Nafion solution. Working electrode was prepared by drop-casting 10 μL of catalyst ink on glassy carbon electrode (GCE, $d = 3 \text{ mm}$, surface area = 0.0707 cm^2). The catalyst ink was dried naturally.

4.2.3 General Procedure for Electrocatalytic OER

Electrochemical measurements were performed using a CHI potentiostat (CHI1030A). Electrocatalytic oxygen evolution reaction was conducted in a typical three-electrode system, using Pt mesh and saturated calomel electrode (SCE) as the counter and reference electrode, respectively, in 1 M potassium hydroxide solution ($\text{pH} = 13$). The electrolyte solution was purged with Ar

for 30 min before the electrochemical measurements to get rid of dissolved oxygen and provide inert atmosphere. Linear sweep voltammetry (LSV) was carried out in a potential range of 0.13 and 0.19 V with a scan rate of 5 mV/s. The potentials measurement against saturated calomel electrode (SCE) were converted with respect to the reverse hydrogen electrode (RHE) according to the following equation:¹⁶⁶

$$E_{\text{RHE}} = E_{\text{SCE}} + 0.244 + 0.0592(\text{pH}) \quad (11)$$

4.2.4 General Procedure for Electrochemical Impedance Spectroscopy

Electrochemical impedance spectroscopy (EIS) was carried out in 1 M KOH aqueous solution that was purged with Ar prior to measurement. Graphite rod and SCE were used as the counter and reference electrodes, respectively. The EIS was measured in the frequency range of 10 mHz and 1 MHz with an amplitude of 5 mV.

4.2.5 Stability Test and Faraday Efficiency for Electrochemical OER

The working electrode was a carbon cloth (1 x 1 cm²) coated with NiFeP nanoparticles. Platinum foil (1 x 1 cm²) and SCE were used as the counter and reference electrodes, respectively. The electrochemical cell was a gas-

sealed two-compartment cell connected with an anionic exchange membrane.

Current density was held at approximately 20 mA cm^{-2} . Oxygen gas evolved was collected by an inverted measuring cylinder under water. The stability test was carried out for 10 h.

4.3 Results and Discussion

4.3.1 Effect of Metal doping on Electrocatalytic OER

Pristine and metal-doped nickel phosphide nanoparticles were coated on glassy carbon electrode and their linear sweep voltammograms (LSVs) were obtained from 1.2 to 1.8 V (vs. RHE, unless stated otherwise) in 1 M potassium hydroxide aqueous solution (Figure 4.1). Since there are observable oxidation peaks in polarization plots, it would be misleading in overpotential estimation to use current density at 10 mA cm^{-2} which is a common level for overpotential estimation. Instead, overpotential value required to reach a current density of 20 mA cm^{-2} has been chosen for comparison to avoid any confusion with the pre-OER peak. The origin of pre-OER peak will be discussed later in this chapter. Ideally, the oxygen evolution from water occurs at 1.23 V with zero overpotential under acidic conditions. The potential difference between 1.23 V and the measured potential to reach 20 mA cm^{-2} current density is the overpotential that indicates the excess energy required for catalyst to conduct electrochemical OER at a considerable rate. The overpotential of pristine nickel phosphide (Ni_2P) nanoparticle at 20 mA cm^{-2} was determined to be 0.39 V. The as-synthesized NiMP nanoparticles (where M = Co, Fe, Mn, and Mo) showed different changes in

activity towards electrochemical OER. The onset potentials for OER shifted in a cathodic direction in the case of Co, Mn, and Mo-doped nickel phosphide (NiCoP, NiMnP, and NiMoP) nanoparticles, whereas the opposite shift of onset potential was observed from Fe-doped nickel phosphide (NiFeP) nanoparticle. Overpotential of NiCoP, NiMnP, and NiMoP nanoparticles at 20 mA cm⁻² are 0.41, 0.55, and 0.43 V, respectively, which are higher than that of Ni₂P nanoparticle. NiFeP nanoparticle shows a more promising activity than Ni₂P nanoparticle towards electrochemical OER, having an overpotential of 0.33 V at 20 mA cm⁻². Despite the different effects of metal doping on OER activity, Ni₂P and all the NiMP nanoparticles exhibited low overpotentials to drive OER electrochemically which are comparable to the benchmark OER electrocatalysts (RuO₂ and IrO₂).

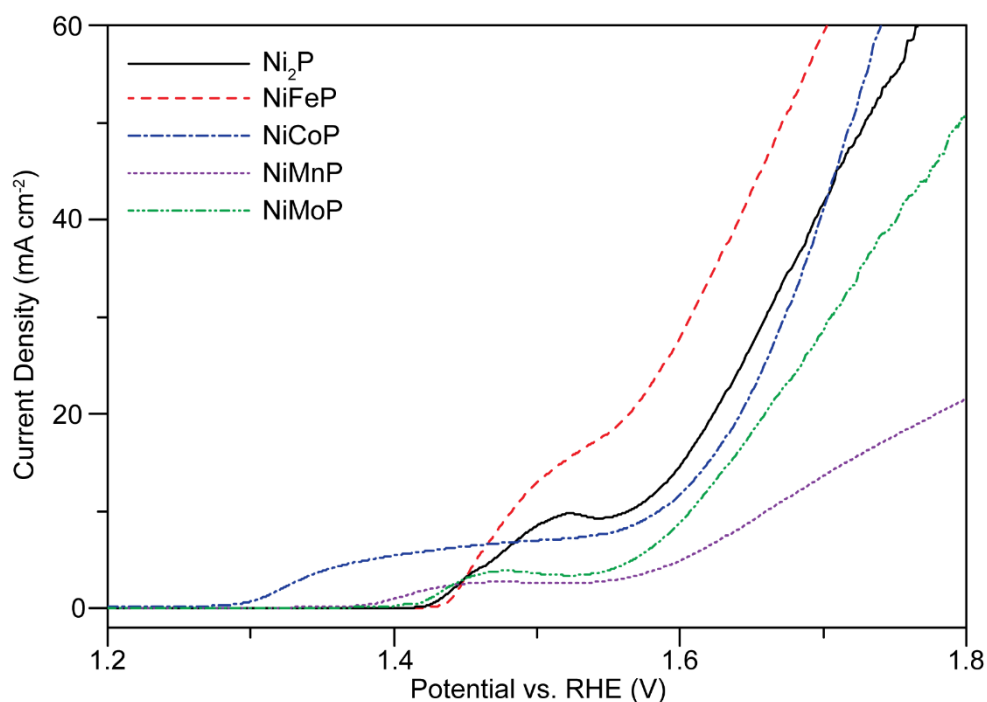
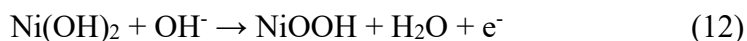


Figure 4.1. Linear sweep voltammograms of Ni_2P and various NiMP nanoparticles in 1 M KOH.

In addition to low overpotential for Ni_2P and NiMP nanoparticles, there are pre-OER oxidation peaks observed in polarization plots at potential ranging from 1.3 to 1.55 V. These pre-OER peaks are typically observed from the metal phosphide-based OER electrocatalyst under alkaline medium, which are originated from the formation of metal oxyhydroxide species (MOOH) on catalyst surface.^{97, 194} With the predominant amount of nickel from nickel phosphide-based system, all the pre-OER peak occurred at potential covering 1.5 V in all polarization plots obtained from different NiMP nanoparticles which is corresponding to conversion of surface nickel hydroxide ($\text{Ni}(\text{OH})_2$) to nickel oxyhydroxide (NiOOH) species.¹⁹⁵



Particularly, NiCoP nanoparticle has a broader oxidation peak in comparison to Ni₂P nanoparticle. The broader oxidation peak is attributed to Co²⁺/Co³⁺ oxidation which occurs at potential around 1.3 V.¹⁹⁶ With the substantial amount of Co incorporated in NiCoP nanoparticle as determined by EDX and has been discussed in Chapter 2, the corresponding oxidation peak of Co²⁺/Co³⁺ is significant and observable which merges with oxidation peak arisen from Ni(OH)₂/NiOOH oxidation reaction, resulting in a broad oxidation peak observed in polarization plot of NiCoP nanoparticle.¹⁹⁶ The pre-OER peak of NiFeP nanoparticle appears at 1.5V, which is similar to the reported value for on nickel-iron alloy.¹⁹⁷ As the water oxidation peak starts to arise at a similar potential, this pre-OER peak appears to merge with OER current. NiMnP nanoparticles showed similar peak merging as in NiCoP nanoparticles. Oxidation of Mn in NiMnP nanoparticle occurs at approximately 1.5 V and merges with that of Ni, resulting a broad pre-OER peak.¹⁹⁸⁻¹⁹⁹ For NiMoP nanoparticle, the pre-OER peak showed slight anodic shift compared to Ni₂P nanoparticle which indicates the oxidation of Mo in NiMoP nanoparticle. In addition, the current densities of oxidation peak decreases in both NiMnP and NiMoP nanoparticles indicate decrease in

amount of nickel being oxidized as compared to Ni₂P nanoparticle.

The corresponding Tafel slopes were calculated from the polarization plots of Ni₂P and various NiMP nanoparticles (Figure 4.2). Ni₂P nanoparticle has a Tafel slope of 58 mV dec⁻¹. Tafel slope of NiFeP nanoparticle is 39 mV dec⁻¹ which is smaller than Ni₂P nanoparticle and comparable to those of benchmark OER electrocatalysts (approximately 40 mV dec⁻¹). This change in Tafel slope suggests the incorporation of iron altered the kinetics of electrochemical OER to be more favorable. In contrast, NiCoP, NiMnP, and NiMoP nanoparticles show the Tafel slopes of 52, 63, and 86 mV dec⁻¹, respectively, which are similar to that of Ni₂P nanoparticle. Based on the comparisons of overpotentials and Tafel slopes among samples tested, NiFeP nanoparticle showed the most potential as an OER electrocatalyst (Table 4.1).

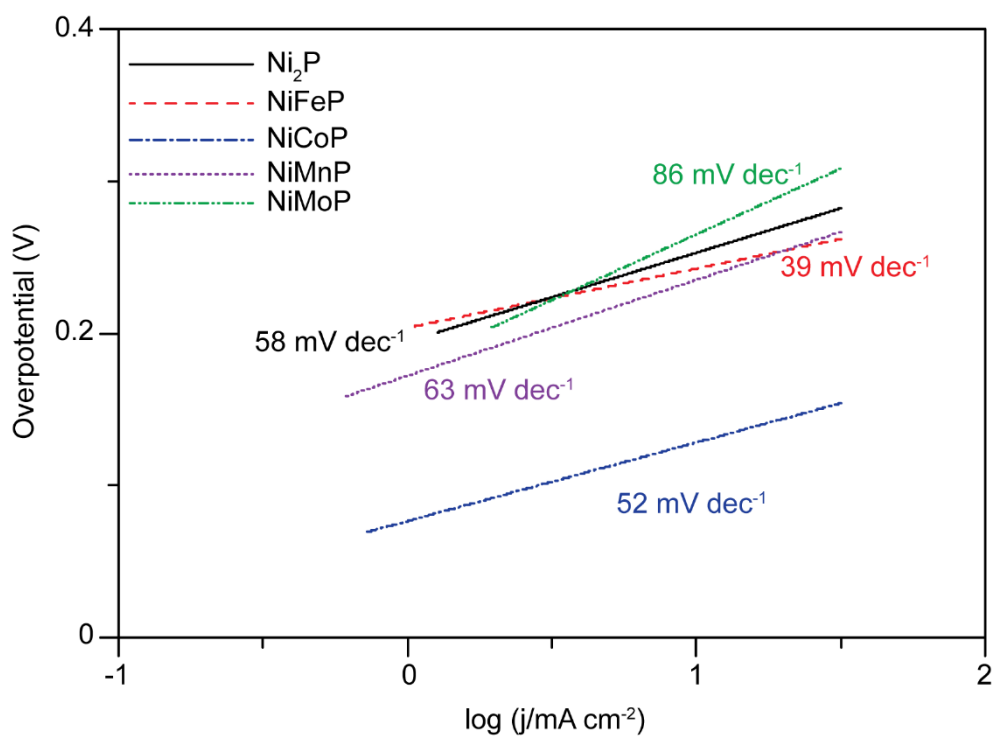


Figure 4.2. Tafel plots of Ni₂P and various NiMP nanoparticles.

Table 4.1. Summary of electrochemical parameters of Ni₂P and various NiMP nanoparticles.

	Overpotential at 20 mA cm ⁻² (V)	Tafel slope (mV dec ⁻¹)
Ni ₂ P	0.39 (2)	58 (2)
NiFeP	0.33 (2)	39 (2)
NiCoP	0.41 (2)	52 (1)
NiMnP	0.55 (3)	63 (1)
NiMoP	0.43 (3)	86 (3)

The reaction order of hydroxide ion in the NiFeP nanoparticle-catalyzed electrochemical OER was determined by carrying out cyclic voltammetry in potassium hydroxide solution of different concentrations (0.1 to 1 M). Current densities at 0.6 V vs. SCE obtained in KOH solution with different concentration are used to estimate reaction order of hydroxide ion with the following equation:²⁰⁰

$$m = \frac{\partial \ln j}{\partial \ln [\text{OH}^-]} \quad (13)$$

where m is the reaction order of hydroxide ion, and j is the current density at potential at 0.6 V vs. SCE (Figure 4.3). The slope is estimated to be 0.98 indicating that the reaction order of hydroxide ion is close to unity in the rate determining step.

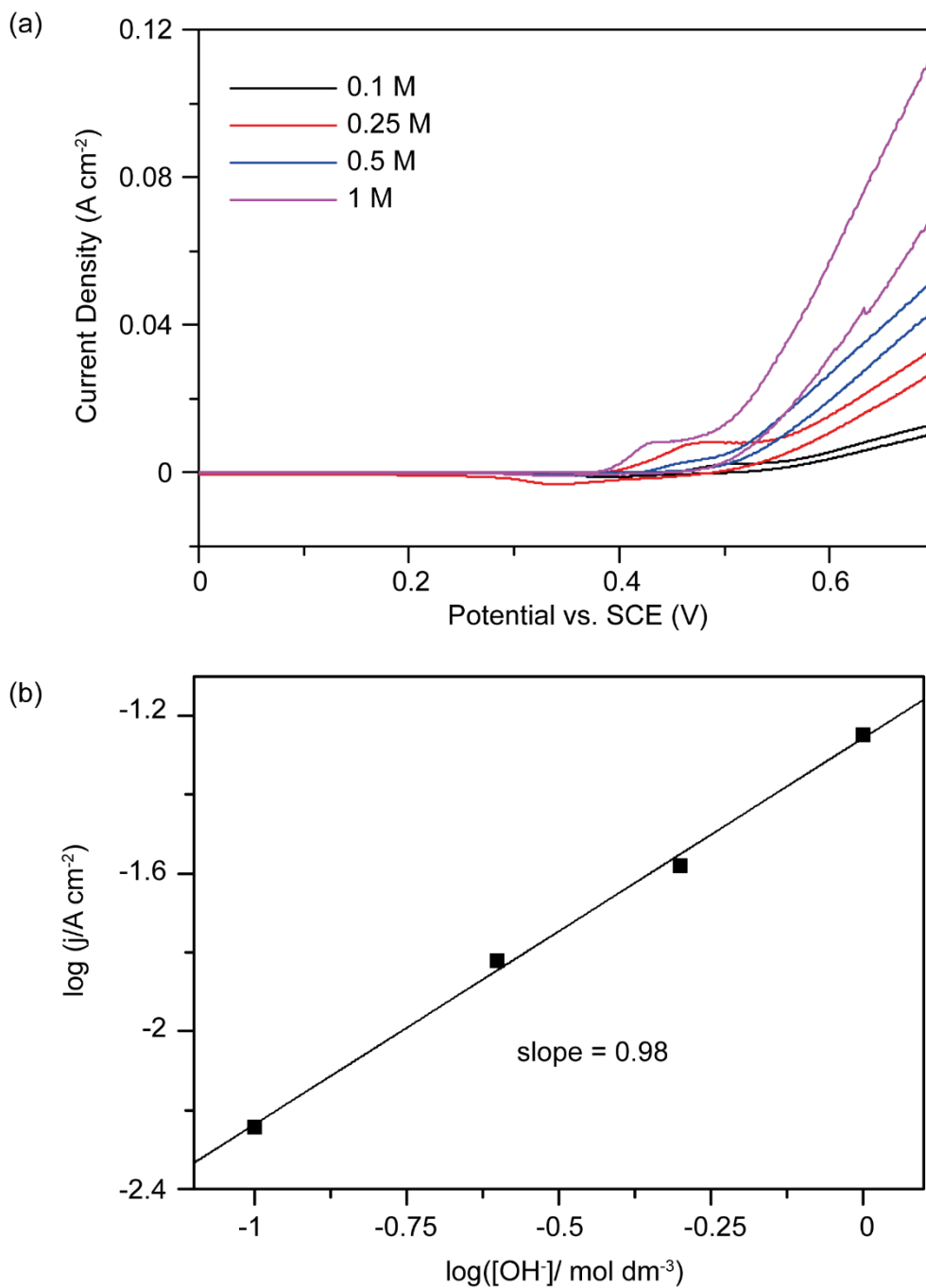
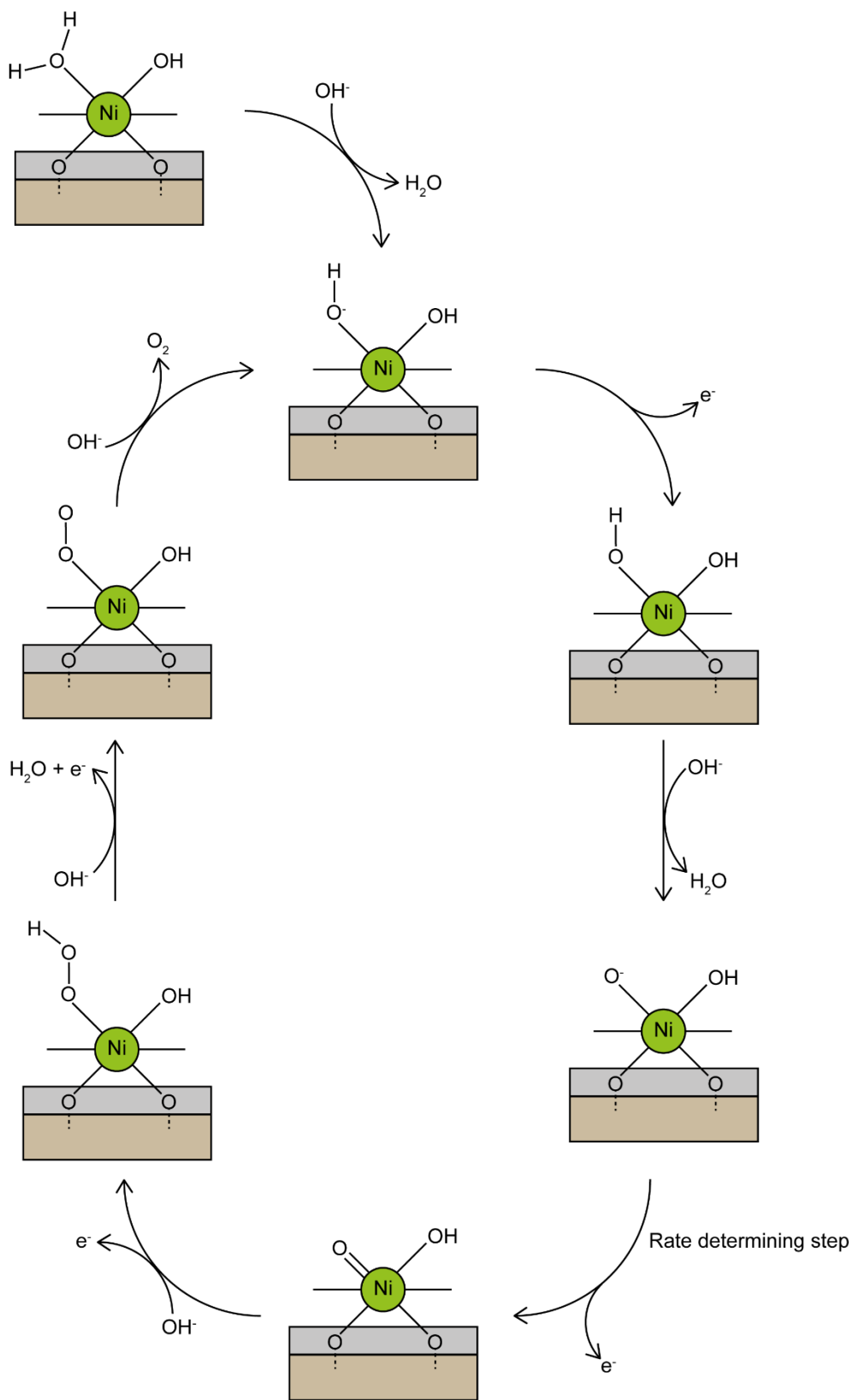


Figure 4.3. (a) Cyclic voltammograms of NiFeP nanoparticle in KOH solution with different concentrations and (b) relationship between current density at 0.6 V vs. SCE and concentration of hydroxide ion.

The mechanism of electrochemical OER can be investigated by using Tafel slope and reaction order of hydroxide ion. The Tafel slope and reaction order of hydroxide ion is $\sim 40 \text{ mV dec}^{-1}$ and 1, respectively, with the employment of NiFeP nanoparticle as OER electrocatalyst.

Numerous studies are conducted to elucidate the mechanism of electrochemical OER and various mechanisms were proposed to fit different kinetic parameters.²⁰⁰⁻²⁰¹ With *in situ* formation of oxyhydroxide as an active electrocatalyst for OER, the proposed mechanism for NiFeP nanoparticle-catalyzed electrochemical OER closely follows other reported oxyhydroxide-mediated mechanism and fits the estimated kinetic parameters discussed (Scheme 4.1).²⁰²



Scheme 4.1. Schematic diagram of proposed mechanism for electrochemical OER.

The reaction begins with the deprotonation of coordinating water molecule since the reaction is carried out in a strongly alkaline medium where water can be easily deprotonated. The hydroxide ion coordinated at the reactive nickel center is subjected to undergo consecutive oxidations, leading to the sequential formation of metal oxide ($M-O^-$) and metal oxo ($M=O$) species. It is believed that one of these intermediate formation step is rate determining. The formations of $Ni-O^-$ and $Ni=O$ intermediates in nickel-based materials are reported to give a theoretical Tafel slope of 60 and 40 $mV\ dec^{-1}$, respectively.²⁰¹ In the case of NiFeP nanoparticle, the formation of $Ni=O$ species is the rate determining step where the presence of iron inhibit the oxidation of nickel center as revealed by the shift of pre-OER peak in polarization plot. Meanwhile for Ni_2P and other NiMP nanoparticles, the rate determining step is the formation of $Ni-O^-$ species. After the formation of $Ni=O$ species, subsequent oxidation occurs on oxygen moiety with addition of another hydroxide ion and this eventually leads to the evolution of oxygen molecules and completion the whole catalytic cycle.

The surface nickel oxyhydroxide *in situ* generated from pre-OER oxidation is believed to be the active electrocatalyst for OER. Early studies of using nickel-related substances in electrochemical OER include the

employment of nickel oxides/hydroxides.^{200, 203} With similar mechanisms mentioned above, both nickel oxide and hydroxide are found to be effective electrocatalysts for OER. Nickel phosphide employed in other studies has already shown a promising catalytic activity on electrochemical OER over nickel oxide and hydroxide.⁹⁷ Such good catalytic performance of nickel phosphides can be attributed to their higher electrical conductivity which retains certain degree of metallic property of nickel. Metallic property was observed in both RuO₂ and IrO₂ which would be one of the key factors for active OER electrocatalysts.²⁰⁴

Iron incorporation is one of the common strategies for improving the activity of nickel-based catalysts.²⁰⁵⁻²⁰⁸ Incorporation of iron leads to the shift of pre-OER peak position towards higher potential, indicating that the oxidation of nickel is suppressed.¹⁹⁵ With the presence of Fe, a partial charge transfer between Fe and Ni occurs which leads to the catalytic activity enhancement.²⁰⁵ The charge transfer from Fe may stabilize the negatively charged Ni-O⁻ species. This was further confirmed by well-matched theoretical and experimental Tafel slopes (40 mV dec⁻¹) where transformation from Ni-OH to Ni-O⁻ species is easier in NiFeP nanoparticle than other nickel phosphide-base nanoparticles. Meanwhile, other NiMP nanoparticles showed

similar Tafel slopes as Ni₂P nanoparticle, indicating that the metal doping did not affect their kinetics and the formation of Ni-O⁻ remained as the rate determining step.

Transition metal M as doper or as electron ligand can alter the band position and its electron filling of the metallic nickel phosphide phase hence affecting the OER activity.^{89, 209-212} By plotting average activity (current density) versus contributed d electron (both *s* and *d* electrons) of different transition metals (Figure 4.4), it is clearly evident that Fe of group 8 gives the proper balanced electron filling to antibonding and bonding bands of modified nickel phosphide, giving the optimal bonding interaction with M-O required for OER catalytic cycle as guided by theoretical calculations.^{89, 209-212}

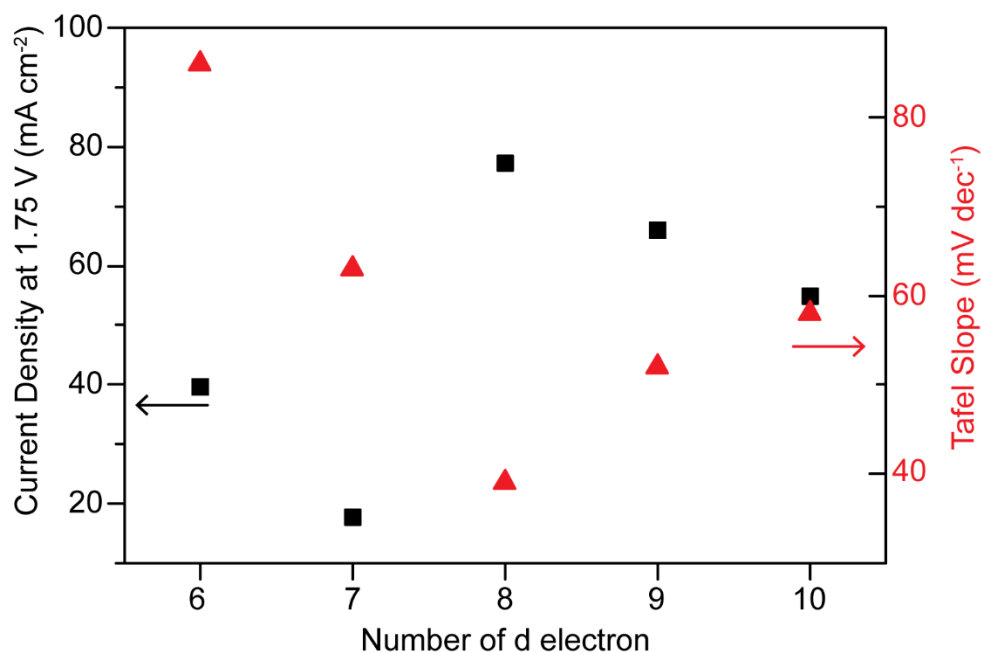


Figure 4.4 A plot of activity (current density) of NiMP versus total injected *d* electrons of transition metal M (Mo = 6, Mn = 7, Fe = 8, Co = 9 and Ni = 10) into the nickel phosphide bands (the slight higher activity of Mo with only 6 *d*-electrons contribution than expected is due to higher energy and more effective 4-*d* bands overlap with O than that of 3-*d* bands in other transition metals).

Interestingly, the anticipated less or greater degree of electrons donation of specific transition metals to the bands of nickel phosphide fall in the predicted positions from either side of the volcano, which depicts a rational approach to alter the electronic structure of this composite for OER. A small discrepancy is the use of second row transition metal, Mo where the energy of $4d$ and its ligand overlap are markedly different from that of the $3d$ transition metals. Notice that inverse average Tafel slopes also match with measured activities over different electron fillings. We have discounted any major contribution from isomorphic or lattice distortion (strain effect) since the transition metal is almost homogeneous substituted to the Ni position.^{89, 207-210} We also note that from Figure 4.1 and 4.2 that the specific activity and Tafel slope do not give the same values but dependent on the applied voltage. The specific activity shows some degree of correlation with fundamental M-O bond strength of transition metal.²¹³ Using low applied potential of 1.5 V where the higher concentration of OH^- and lower positive charged electrode (low activity), the activity is actually dependent on the M-O bonding formation as a principle rate determining step hence the stronger nature of M-O such as Fe gives excellent activity compared to other transition metals (Figure 4.5 (a)).

Thus, Fe on surface of the composite NiFeP with strong Fe-O bond will favor adsorption of OH⁻ with unit order as described in Figure 4.5 (a). Conversely, using higher applied potential of 1.8 V where the depleting concentration of OH⁻ and higher positive charged electrode (high activity) the specific activity becomes to favor more dominated of M-O bond cleavage hence the weaker nature of M-O such as Ni and Co give comparable activity to Fe (Figure 4.5 (b)). Thus, there is an apparent synergetic effect for both transition metal atoms on the surface of NiFeP to work cooperatively: the formation of oxyhydroxide may be mainly taken place on Fe to form Fe-O and then Ni catalyzes cleavage of Ni-O bond for O₂ formation to complete the OER catalytic cycle, probably involving charge-transfer through their oxygen-covered skin as that described in Ni-Fe mixed oxide.²¹² Thus, the proposed elementary mechanism for NiFeP nanoparticle follows oxyhydroxide-mediated mechanism involving both M-O bond construction and M'-O cleavage, see Scheme 4.1.^{194-195, 205-207} Hence, NiFeP with unique tunable conductive band structure and homogeneous surface composition can give optimal OER activity.

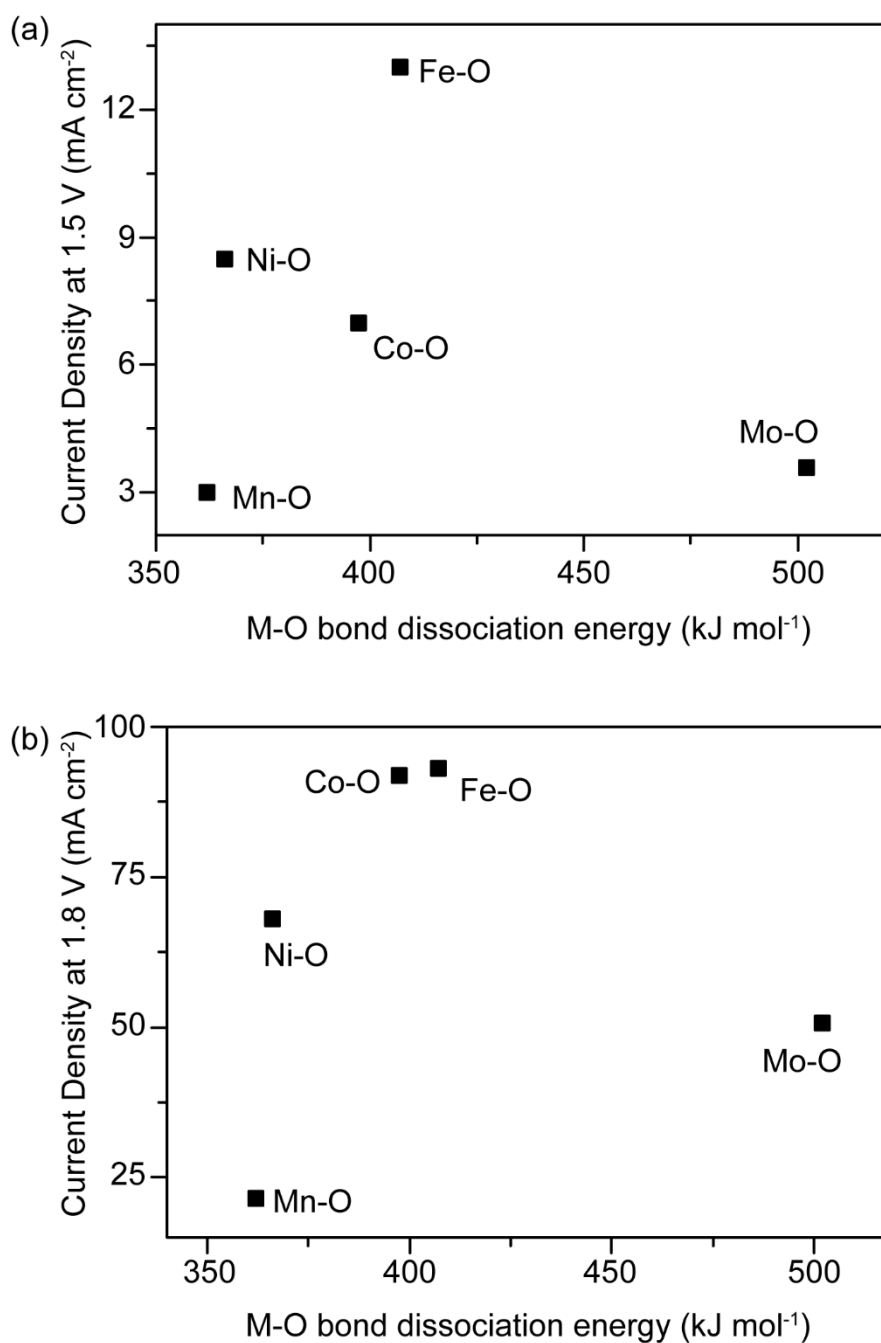


Figure 4.5 (a) Correlation of the activity (current density) of composite NiMP with M-O bond energy: low applied potential of 1.5 V where the higher concentration of OH⁻ and lower positive charged electrode (low activity) favor the M-O bonding formation as a principle rate determining step hence stronger nature of M-O i.e. Fe gives relatively good activity and (b) high applied potential of 1.8 V where the depleting concentration of OH⁻ and higher positive charged electrode (high activity) tends to favor the bond cleavage of M-O hence the weaker nature of M-O i.e. Co, Ni gives relatively high activity with reference to Fe.

In addition, electrochemical impedance spectroscopy (EIS) was carried out for both Ni₂P and NiFeP nanoparticle to investigate the effect of Fe doping on the conductivity of catalyst. The equivalent circuit was constructed to compose of three components, which represent electrolyte, *in situ* formed surface oxide layer, and phosphide layer underneath (Figure 4.6).²⁰¹ The semicircle in Nyquist plot reveals the charge transfer resistance. Nyquist plot of NiFeP nanoparticle has a smaller semicircle than that of Ni₂P nanoparticle which indicates a lower charge transfer resistance in NiFeP nanoparticle than in Ni₂P nanoparticle (Figure 4.7).

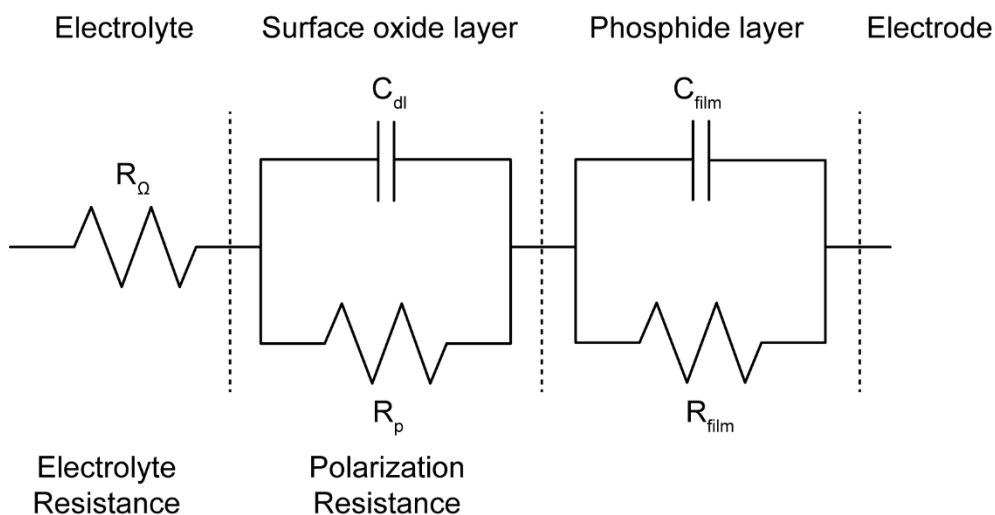


Figure 4.6. Equivalent circuit model used for iron-doped and pristine nickel phosphide nanoparticles.

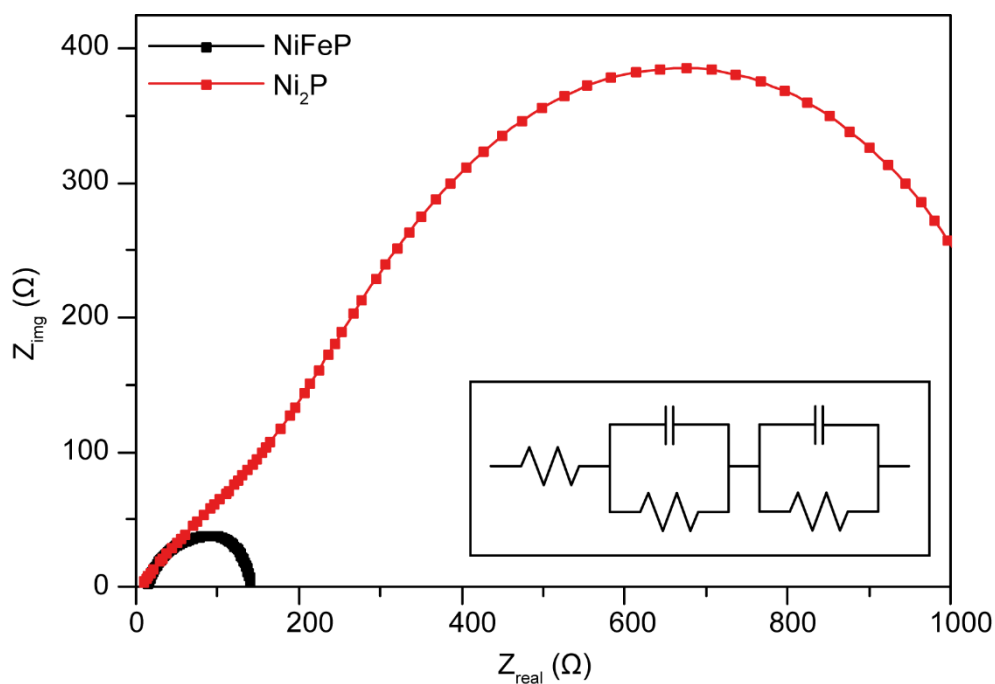


Figure 4.7. Nyquist plots obtained from electrochemical impedance spectroscopy of iron-doped and pristine nickel phosphide nanoparticles recorded in 1 M KOH solution. Inset showed the equivalent circuit model as in Figure 4.6.

Stability is an essential criterion for development of OER electrocatalyst.

Therefore, the best OER electrocatalyst, NiFeP nanoparticle, is subjected to test for stability. Oxygen evolution reaction was carried out with the current density at approximately 20 mA cm^{-2} in 1 M KOH for 10 h (Figure 4.8 (a)).

The current density was maintained for 10 h indicating NiFeP nanoparticle is a stable electrocatalyst for OER. In addition, the amount of oxygen produced every hour was determined and Faraday efficiency was calculated (Figure 4.8 (b)). The oxygen production rate is linear throughout the 10-h stability test and the Faraday efficiency is close to 100% which indicates NiFeP nanoparticle is a stable OER electrocatalyst.

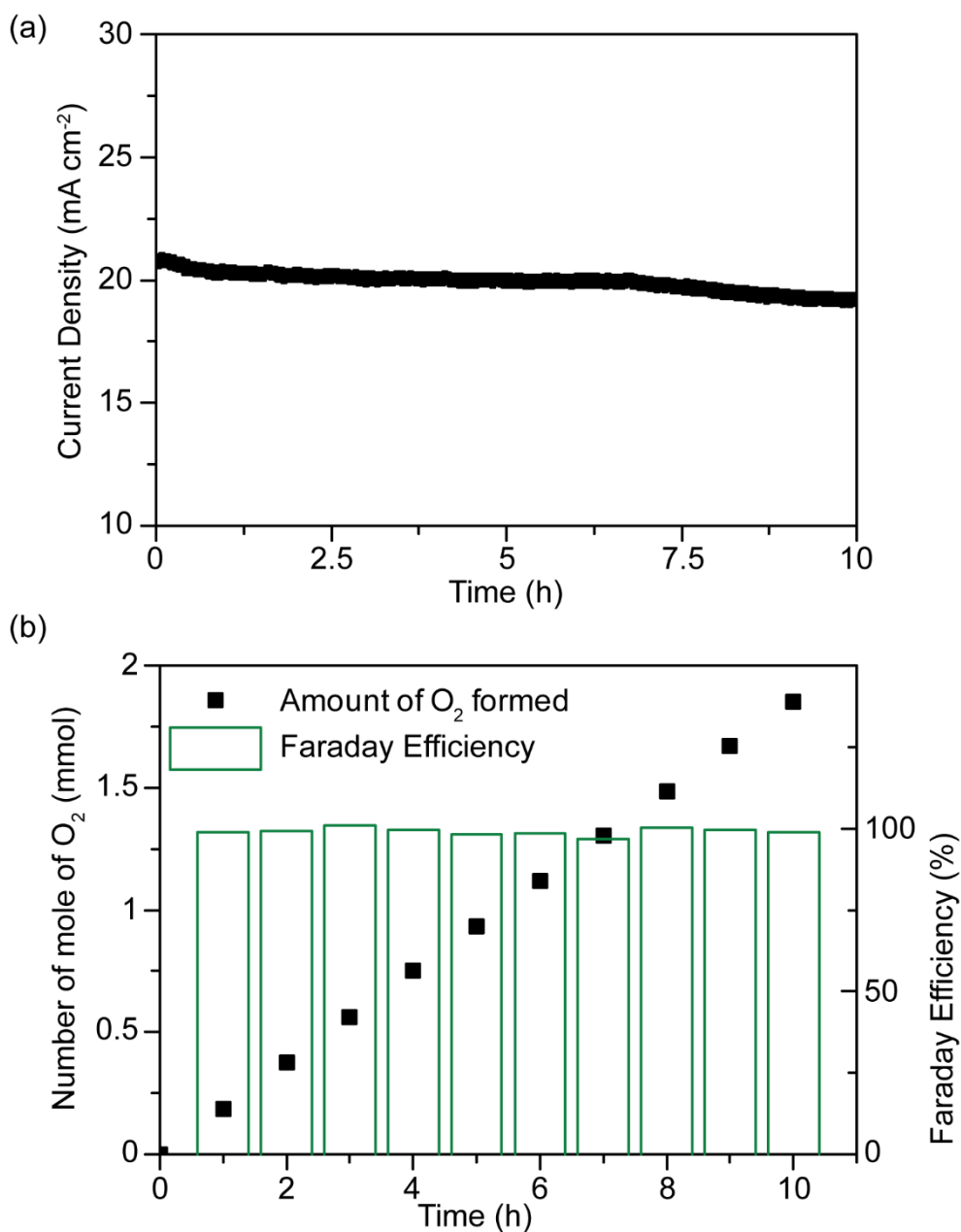


Figure 4.8. (a) Stability test of NiFeP nanoparticle at current density approximately 20 mA cm⁻² for 10 h and (b) oxygen evolution during stability test.

4.3.2 Effect of Precursor Ratio

The effect of precursor ratio was studied using NiCoP nanoparticle as a model. In Chapter 2, it was shown that the degree of cobalt incorporation in nickel phosphide crystal lattice is related with the precursor ratio. Different NiCoP nanoparticles were prepared under different nickel-to-cobalt precursor ratio and tested for the electrochemical OER activity. Similar to previous section, the LSVs were measured in the potential range of 1.2 and 1.8 V using different NiCoP nanoparticles (Figure 4.9 (a)). The overpotentials of NiCoP nanoparticle decrease initially with increasing nickel-to-cobalt precursor ratio, from 0.54 V for NiCoP31 nanoparticle, 0.48 V for NiCoP21 nanoparticle, to 0.41 V for NiCoP11 nanoparticle. Further increase of nickel-to-cobalt precursor ratio leads to the increase in overpotential, 0.47 V for NiCoP12 nanoparticle. In addition, Tafel slopes of various NiCoP nanoparticle showed identical trend as in overpotentials (Figure 4.10). The Tafel slopes decrease initially from 117, 98, to 51 mV dec^{-1} for NiCoP31, NiCoP21, and NiCoP11 nanoparticles, respectively. NiCoP12 has a higher Tafel slope of 92 mV dec^{-1} compared to NiCoP11 nanoparticle. From the overpotentials and Tafel slopes, NiCoP11 nanoparticle exhibited the best OER performance among NiCoP nanoparticles of various nickel-to-cobalt ratios. This can be related to the

formation of NiOOH species which can be revealed by the pre-OER peaks in polarization plots. The intensity of pre-OER peak increases with cobalt loading, from NiCoP31, NiCoP21, to NiCoP11 nanoparticles (Figure 4.9 (b)). The formation of NiOOH is suppressed upon further increase of cobalt loading as revealed by small pre-OER peak in polarization plot of NiCoP12 nanoparticle. The activity on electrochemical OER is related to the intensity of pre-OER peak as well as the amount of NiOOH species formed prior to oxygen production. This further proves the formation of NiOOH species is crucial to conduct OER. The amount of cobalt incorporated in nickel phosphide affects the efficiency of the formation of NiOOH. Combining the two sections, the intrinsic property and the amount on metal incorporated are shown to significantly affect the formation of active species prior to OER.

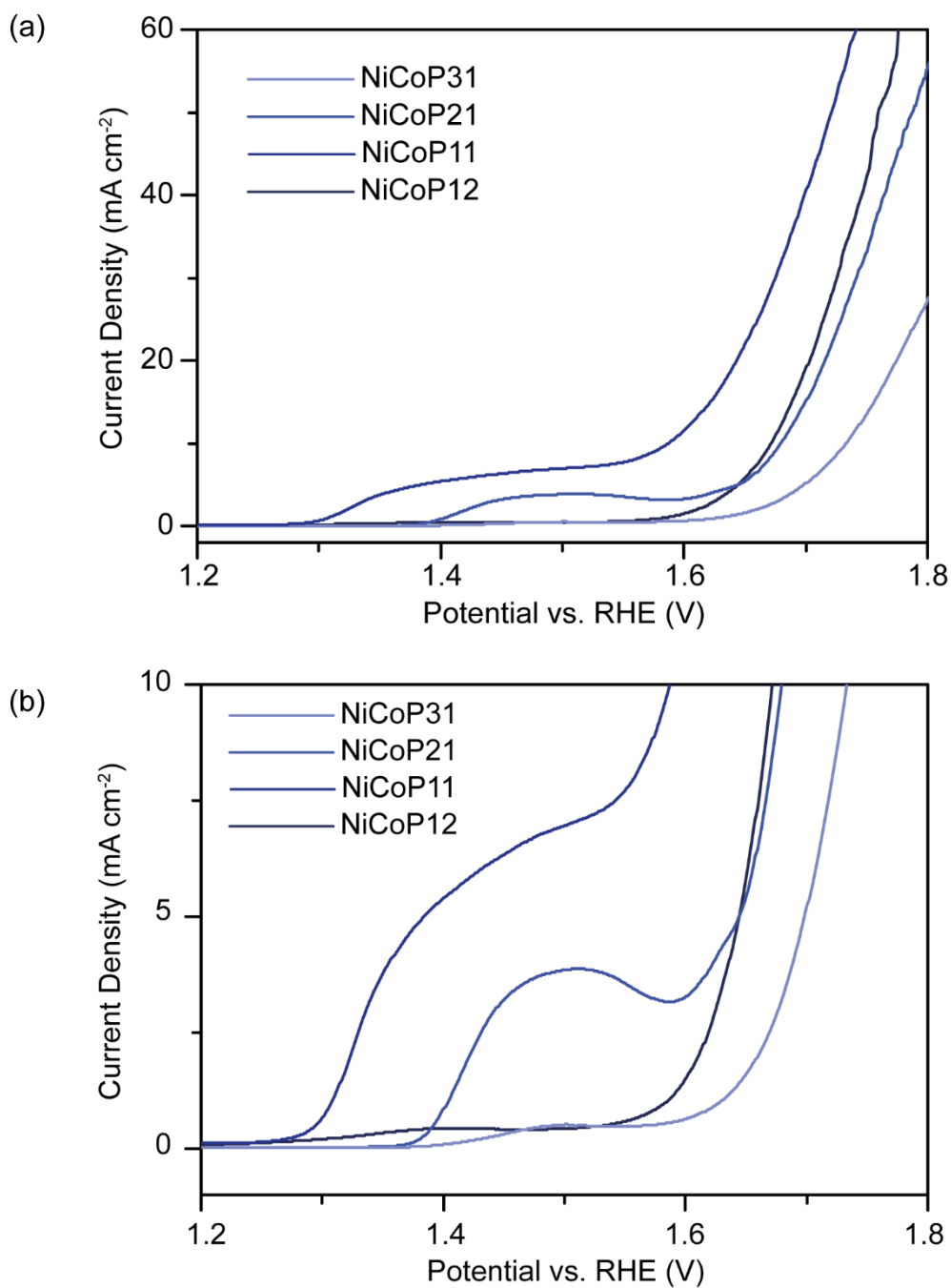


Figure 4.9. (a) Linear sweep voltammograms NiCoP nanoparticles synthesized under different nickel-to-cobalt ratio and (b) the magnified region of oxidation peaks.

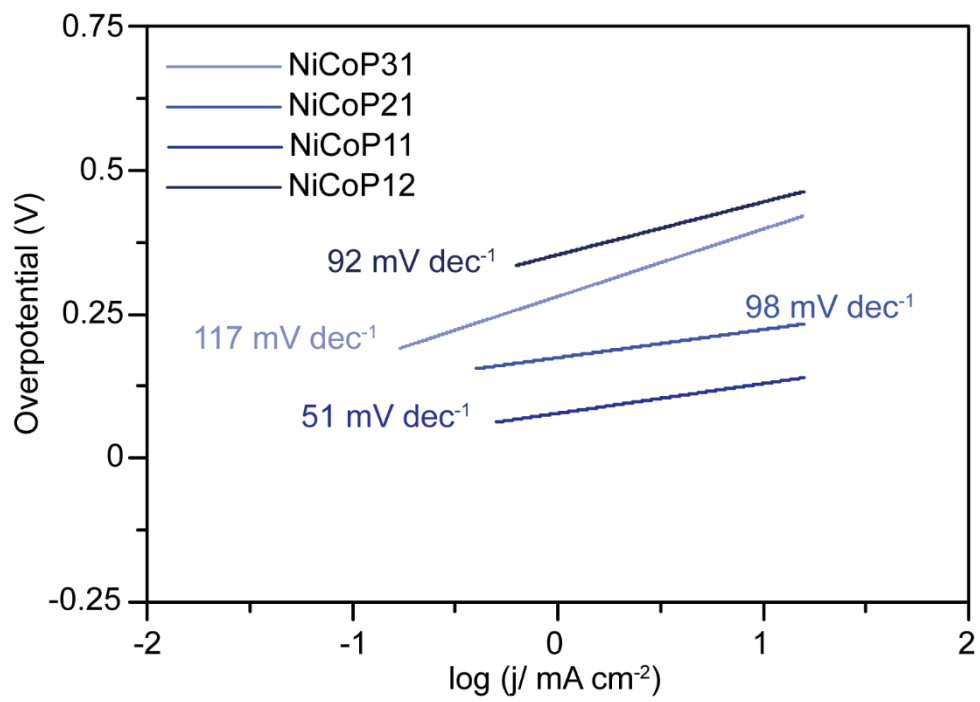


Figure 4.10. Tafel plots of NiCoP nanoparticles synthesized with various nickel-to-cobalt ratio.

4.4 Conclusion

Pristine and metal-doped nickel phosphide nanoparticles are found to be an effective electrocatalysts for OER. Iron-doped nickel phosphide nanoparticle offers an excellent electrocatalytic activity with an overpotential of 0.33 V at 20 mA cm⁻² and a low Tafel slope of 39 mV dec⁻¹. Surface nickel oxyhydroxide is formed prior to the oxygen evolution. Nickel oxyhydroxide plays a crucial role in OER evolution. A redox couple of Ni²⁺ and Ni³⁺ is involved in the adsorption of hydroxides, which are subsequently deprotonated and combined to form oxygen molecules. Phosphide phase beneath surface oxyhydroxide layer provides electric conductivity with its metallic property. This supports the transfer of electrons from surface oxidized layer to electrode which facilitates successful consequential water oxidation. In addition, charge transfer resistance is dramatically reduced by the incorporation of iron as revealed by electrochemical impedance spectroscopy.

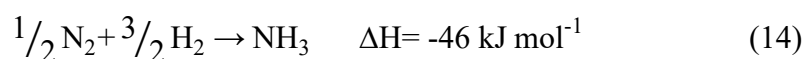
Syntheses of cobalt-doped nickel phosphide nanoparticle with different nickel-to-cobalt ratios are carried out. Intensity of pre-OER peak, an indicative of MOOH formation, and catalytic performance of OER were largely enhanced with increased loading of cobalt precursor. The optimal

nickel-to-cobalt precursor ratio is 1:1 which showed the lowest overpotential and Tafel slope. Further increase in the cobalt precursor ratio led to the suppression of oxyhydroxide species formation and resulted in the decrease of catalytic activity.

Chapter 5 Catalytic Ammonia Synthesis

5.1 Introduction

Ammonia is one of the most useful chemicals in daily basis. It can be used to produce polymers, fertilizers, and other useful chemicals including urea and hydrazine.²¹⁵ With the versatile applications, ammonia is the most produced inorganic compound among all chemical-producing industries. Haber-Bosch process is used in industry which is developed by Fritz Haber and Carl Bosch in early 1900s.²¹⁶ Fritz Haber recognized the exothermic reaction between nitrogen and hydrogen gas is not favorable in high temperature environments but under high pressure conditions. With the assist of Carl Bosch, the reactor for ammonia synthesis was built to withstand high pressure and successfully produced ammonia at a considerable rate.



In addition to high pressure conditions, iron-based catalysts are employed to facilitate the production of ammonia. The iron-based catalysts play a crucial role in cleaving N-N triple bond where iron atoms bind and stabilize the adsorbed nitrogen atoms on the catalyst surface. This step is believed to be the rate determining step in ammonia synthesis since this step release much energy from iron-nitrogen bond formation, approximately 140

kcal mol^{-1} .¹⁰⁶ To overcome the rate-determining nitrogen adsorption step, promoters are added to enhance the rate of nitrogen adsorption. Common promoters are alkali metals, such as potassium, which can help the adsorption of atomic nitrogen species by enhanced electron density at the Fe surface.^{109, 217-218} As they assist the nitrogen adsorption by enhancing charge transfer from alkali metals to catalyst, they are called electronic promoters. In addition, the activation energy for converting adsorbed nitrogen molecules to atomic nitrogen is lowered in the presence of alkali metal promoters (Figure 5.1).¹⁰⁶ There are usually structural promoters present in the system. The common structural promoters are stable oxides such as aluminum oxide and magnesium oxide.²¹⁹⁻²²¹ These oxides stabilized finely-divided particles from sintering to preserve the surface area for reaction.

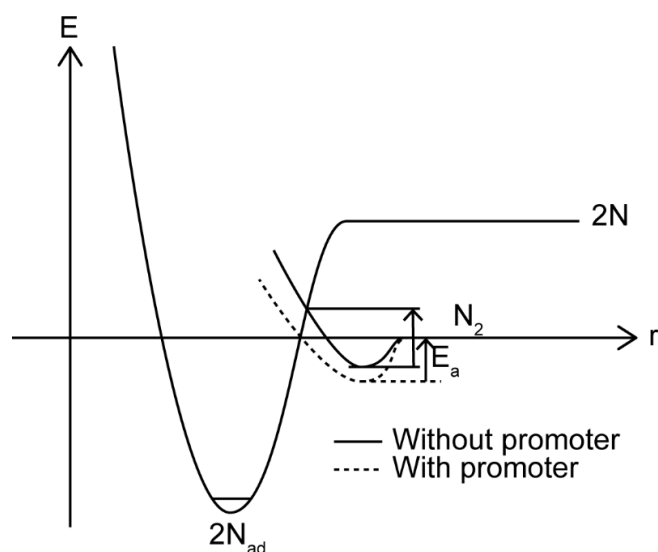


Figure 5.1. Potential energy diagram for conversion of adsorbed nitrogen molecule to atomic nitrogen. This is adapted from reference 106.

Active development is on-going by employing other materials for the catalytic ammonia synthesis. The most popular one next to the iron-based catalysts are the ruthenium-based catalysts.^{10, 222} Ruthenium offers better bonding environments towards nitrogen adsorption than iron, which is attributed to its optimal free energy of nitrogen adsorption (ΔG_N).¹⁰ Despite this advantage, ruthenium-based catalysts are facing the problems of high cost and scarcity of ruthenium. Recently, a bimetallic system composing cobalt and molybdenum has been constructed and employed in catalytic ammonia synthesis.^{117, 120, 223} The two metals possess opposite properties towards nitrogen adsorption, i.e., cobalt binds weakly and molybdenum binds strongly with nitrogen atoms. The combination of these elements allowed an optimal nitrogen adsorption energy which led to an effective catalysis towards ammonia production. Apart from combination of cobalt and molybdenum, cobalt and iron are combined and employed as an ammonia-producing catalyst.¹²¹ These combinations share the same idea that employ strongly and weakly nitrogen-binding metals together to produce ammonia. Through the analysis of descriptor for catalytic ammonia synthesis (ΔG_N), rational combination of elements possessing opposite property provides a way to look for substitute to one with optimal descriptor value.

In the previous chapters, different metal-doped nickel phosphide nanoparticles are synthesized and showed promising activities in hydrogen and oxygen evolution reactions. The same nickel phosphide nanoparticles have been studied for the application in catalytic ammonia synthesis. Iron-doped nickel phosphide nanoparticles are shown to be a potential candidate for catalytic ammonia synthesis. Iron incorporated in nickel phosphide acts as a reaction center in ammonia production similar to the conventional iron-based catalysts.

5.2 Material and Experimental Procedures

Pre-treatment of NiFeP nanoparticle for ammonia synthesis was carried out prior to catalysis. Barium promoter was incorporated with NiFeP nanoparticle during the pre-treatment process. Barium nitrate and NiFeP nanoparticle were mixed with a barium-to-nickel molar ratio of 1:1. The mixed powder was put into a furnace and heated up to 500 °C for 6 h. Nitrogen and hydrogen gas mixture with a ratio of 1:3 was blown into the furnace at the same time with flow rate of approximately 50 mL min⁻¹.

After the pre-treatment of catalyst, the Ba-promoted NiFeP was subjected to the analysis for ammonia synthesis. The catalysis was carried out under high-pressure conditions in a specialized reactor as shown in the schematic diagram below (Figure 5.2).

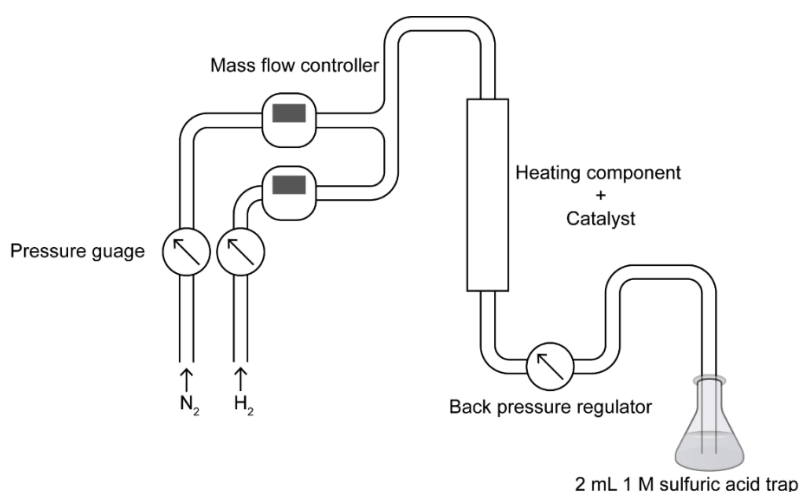


Figure 5.2. Schematic diagram of reactor for catalytic ammonia synthesis.

Nitrogen and hydrogen gases were fed into the reactor with a ratio of 1:3 at the flow rate of approximately 100 mL min^{-1} . Reaction was carried out at $470 \text{ }^{\circ}\text{C}$ and 50 bar for 4 h. Ammonia produced was collected by 2 mL 1 M sulfuric acid trap. Amount of ammonia was determined by titration using sodium hydroxide solution.

5.3 Iron-doped Nickel Phosphide Nanoparticle as Catalyst for Ammonia Synthesis

Iron-doped nickel phosphide (NiFeP) nanoparticle is employed in catalytic ammonia synthesis. The NiFeP nanoparticles were pre-treated with a promoter which provides electronic and structural supports to facilitate ammonia synthesis. Barium nitrate, with same number of moles with respect to nickel, is mixed with NiFeP nanoparticle and the solid mixture was heated up to 500 °C in a flow of the 1:3 nitrogen and hydrogen mixture. Under such conditions, barium nitrate is readily decomposed, leading to the formation of barium oxide (BaO) and possibly Ba⁰ species.²²⁴⁻²²⁵ As both structural and electronic promoters, these Ba species supports NiFeP nanoparticle in the catalytic ammonia synthesis by preventing the nanoparticles from sintering and facilitating the nitrogen adsorption. Ba⁰ is believed to be formed under the reducing environments and acts similarly as conventional alkali-metal promoters that provide electron density to facilitate nitrogen adsorption. BaO provides structural support for catalyst to maintain its structure under the reaction conditions.^{222, 225}

After the pre-treatment of NiFeP nanoparticle, a composite Ba-NiFeP was prepared and employed in catalytic ammonia synthesis. Nitrogen and

hydrogen gas were supplied with a ratio of 1:3 which is the stoichiometric ratio for ammonia synthesis. Catalysis was carried out in the elevated temperature (470 °C) and pressure (50 bar) for 4 hours. Exhausted gas was purged in a sulfuric acid trap. Ammonia produced was collected and reacted with 1 M sulfuric acid. Sodium hydroxide solution was used to determine amount of acid left after 4-hour reaction as well as ammonia produced. The rate of ammonia production by Ba-NiFeP was determined to be 7.35 mmol h⁻¹ g⁻¹ through the back-titration of sulfuric acid trap (Figure 5.3). NiFeP nanoparticle shows a better activity towards catalytic ammonia synthesis as compared to other non-iron and non-ruthenium-based catalysts including cesium promoted-cobalt molybdenum nitride (Cs-Co₃Mo₃N) and cobalt-molybdenum alloy supported by cerium dioxide (Co-Mo/CeO₂). These two materials offer an ammonia production rate of 0.986 and 0.783 mmol h⁻¹ g⁻¹, respectively.^{120, 223} However, the performance of NiFeP nanoparticle is far below that of ruthenium-based catalyst (Ba-Ru_{9.1}/C).²²⁶

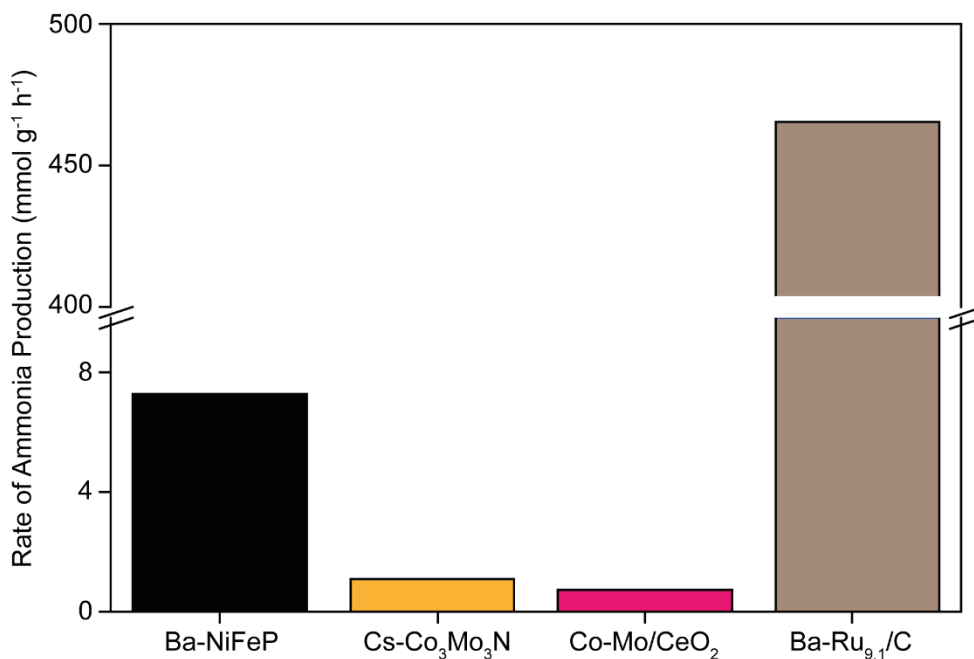


Figure 5.3. Comparison of catalytic activity towards ammonia synthesis between NiFeP nanoparticle, non-Fe and Ru-based catalysts, and typical Ru-based catalyst. The catalytic activity is adapted from reference 120, 221, and 226.

A control experiment was carried out using pristine nickel phosphide nanoparticle to elucidate the effect of iron doping in nickel phosphide crystal lattice towards catalytic ammonia synthesis. Identical promoter (Ba) and procedures were used in trial for pristine nickel phosphide nanoparticle. Ba-Ni₂P gives a rate of ammonia production with a value of 3.4 mmol h⁻¹ g⁻¹. Compared to NiFeP nanoparticle, Ba-NiFeP system give a two-fold enhancement on production of ammonia. Considering the small amount of iron doping, the effect on the catalytic enhancement is considerably large. However, other metal-doped nickel phosphide nanoparticles prepared, as

discussed in previous chapters, showed no significant reactivity on catalytic ammonia synthesis.

With the above preliminary results, further investigation is conducted on employing NiFeP nanoparticle as ammonia-producing catalyst. Nickel phosphide crystal lattice is hypothesized to not only allow iron incorporation and act as a reaction center for ammonia synthesis, but also provide electron density with metallic property of nickel phosphide base and be a support to segregate iron moiety, mimicking an alkali metal-promoted system with oxide support. To test this hypothesis, NiFeP nanoparticles were tested for catalytic ammonia synthesis without the addition of Ba-promoter.

The same pre-treatment process was carried out without adding barium nitrate salt to ensure the state of NiFeP nanoparticle is identical as in the Ba-promoted system. Analysis was carried under the same experiment conditions as before. The amount of ammonia formed was examined after the first, third and fourth hour (Figure 5.4). The production rate of ammonia dropped rapidly with time. In the first-hour reaction, the ammonia production rate is comparable to the Ba-promoted NiFeP system ($7.35 \text{ mmol h}^{-1} \text{ g}^{-1}$). It shows that the unpromoted NiFeP system possesses similar reactivity on ammonia production. However, in the third and fourth-hour measurements, the rate of

ammonia production decreases to $3.5 \text{ mmol h}^{-1} \text{ g}^{-1}$ and eventually to zero. It indicates the instability of catalyst under such circumstances.

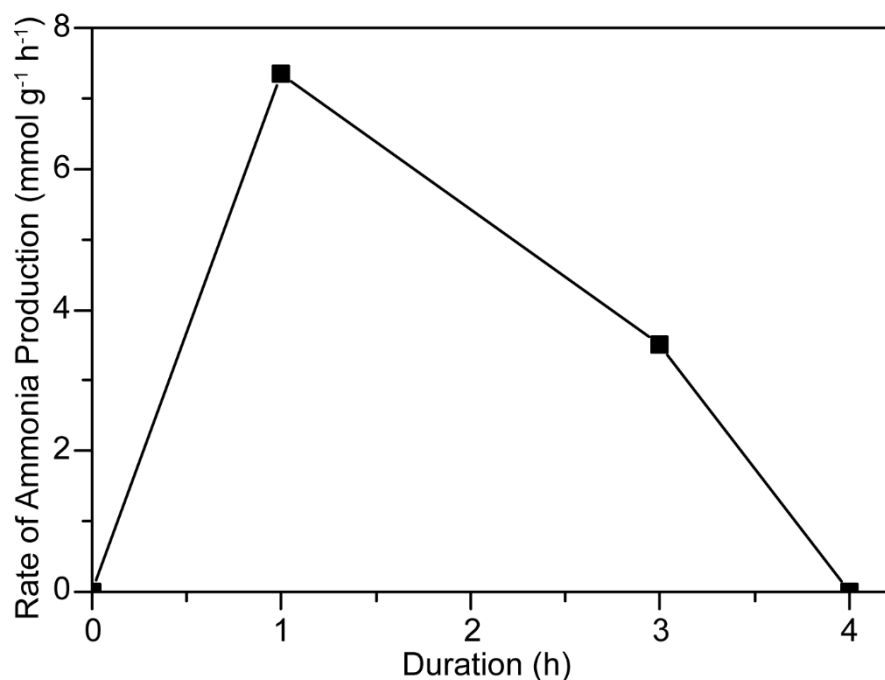


Figure 5.4. A 4-hour ammonia production by NiFeP nanoparticle without addition of promoters.

The possible reason for the unstable reactivity is due to the absence of Ba-promoter. The Ba-promoter is used to assist Ru-based catalyst to facilitate nitrogen adsorption.²²⁷ Ba-promoter is believed to be in a form of Ba^0 and BaO and acts as a bifunctional promoter, both electronic and structural, to facilitate ammonia production. Under reaction conditions for ammonia synthesis, nitrogen and hydrogen molecules are present and competing for adsorption sites on catalyst surface. Ba^0 provides a surface for hydrogen

adsorption which can prevent a high hydrogen coverage on catalytic surface.

A high hydrogen coverage on catalyst surface is detrimental for ammonia production since it prohibits nitrogen adsorption, the first elementary step for ammonia synthesis. In addition, Ba-promoter in the form of BaO provides structural support to maintain the dispersion of finely-divided Ru particles.^{222, 225} In the case of NiFeP nanoparticle, Ba-promoter is believed to act similarly as in Ru-based catalysts. Ba⁰ provides rooms for hydrogen adsorption to prevent overwhelming hydrogen coverage on NiFeP nanoparticle. Especially for nickel and iron, they possess a negative free energy for hydrogen adsorption as discussed in Chapter 3, making them highly favorable for having hydrogen adsorption.⁹ In addition, BaO from Ba-promoter can act as structural promoter which prevent aggregation of NiFeP nanoparticle upon elevated pressure and temperature during catalytic ammonia synthesis. Aggregation of nanoparticle leads to decrease in surface area of catalysts which would lead to the deterioration in catalytic activity. Therefore, Ba-promoter is believed to act as a stabilizer to maintain the nanostructure of NiFeP nanoparticle under elevated temperature and pressure and prevent excess hydrogen adsorption, which are crucial to have sustainable production rate of ammonia.

Based on these results, a pre-treatment of NiFeP nanoparticle with Ba is an essential step to apply it to the catalytic ammonia synthesis. The catalytic enhancement could be achieved by doping Fe and this NiFeP nanoparticle could be stabilized by Ba treatment. To understand the enhancement mechanism, the effects of iron incorporation into nickel phosphide crystal lattice have been investigated.

Pristine nickel phosphide has a hexagonal structure with a space group of $P\bar{6}2m$ (Figure 5.5). The crystal structure possesses the repeating Ni_3P_2 and Ni_3P layers. Therefore, there are two types of terminal groups in (0001) lattice plane of Ni_2P , including Ni_3P_2 and Ni_3P plane (Figure 5.6 (a) and (b)). Ni_3P_2 is believed to be the dominant terminal plane for Ni_2P (0001) lattice plane by calculation using density functional theory (DFT).²²⁸ With the small amount of iron incorporation, the nickel atom in Ni_3P_2 is substituted with an iron atom forming some $FeNi_2P_2$ terminal planes. This is consistent with the EXAFS measurement discussed in Chapter 2, where the bond lengths of Ni-Fe and Ni-Ni are similar, indicating a substitution of Ni with Fe to form the $FeNi_2P_2$ terminal plane. The terminal plane reveals the presence of iron in the vicinity of nickel which is important in carrying out ammonia synthesis.

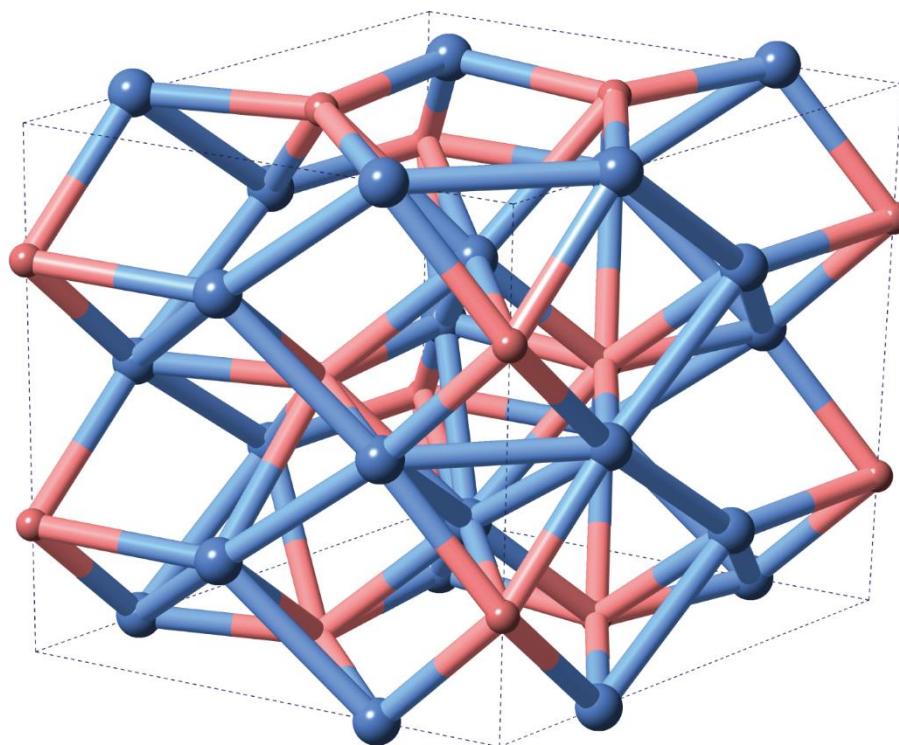


Figure 5.5. Crystal structure of Ni_2P with a space group of $\text{P}\bar{6}2\text{m}$. Blue and red atoms are nickel and phosphorus, respectively.

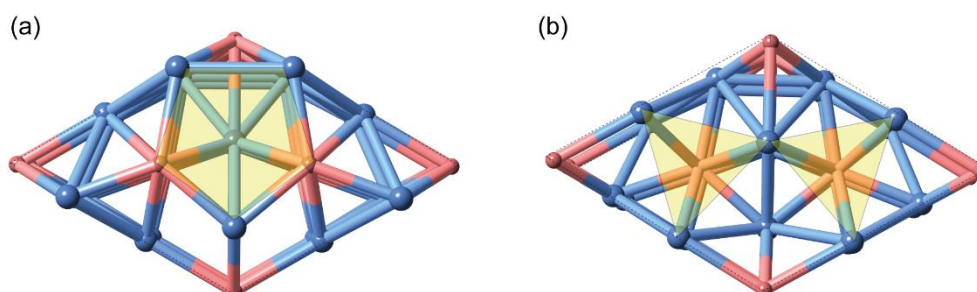


Figure 5.6. Terminal planes of Ni_2P along (0001) lattice plane: (a) Ni_3P_2 and (b) Ni_3P . Blue and red atoms are nickel and phosphorus, respectively.

The reaction mechanism on iron surface is proposed by Ertl with estimated potential energy (Figure 5.7).¹⁰⁶ From the reaction profile, ammonia synthesis is carried out in multiple steps: (1) adsorption of nitrogen on catalyst surface, (2) cleavage of N-N triple bond and H-H bonds and the

formation of adsorbed nitrogen and hydrogen species, (3) subsequent hydrogen additions on adsorbed nitrogen atom, and (4) release of adsorbed ammonia as final product. The most difficult step, according to the reaction profile, is the first addition of hydrogen to nitrogen, which requires the largest activation energy among all steps at low temperature due to its high activation energy barrier. However, under the ordinary ammonia synthesis conditions (approximately 200 atm and 450 °C), the dissociation of nitrogen is the rate determining step due to its exothermic nature in the from formation of Fe-N bond, making it not favored under high temperature conditions.

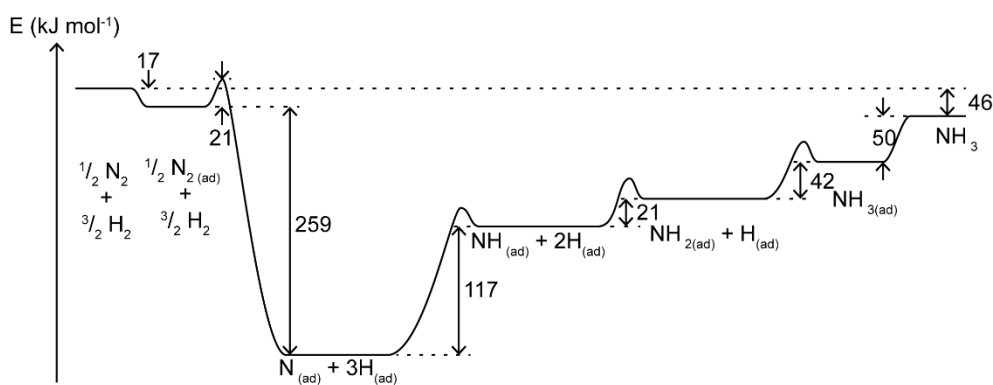


Figure 5.7. Proposed reaction mechanism of catalytic ammonia synthesis. This is adapted from reference 106. Numerical values are in unit of kJ mol^{-1} .

Iron-doped nickel phosphide nanoparticle is believed to carry out ammonia synthesis in a similar reaction mechanism as in iron-based catalysts.

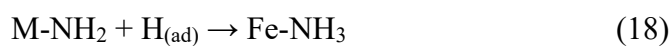
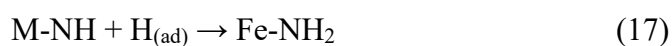
The nitrogen molecule would adsorb on the metal center, forming a Ni-N₂ or

Fe-N₂ species (or collectively M-N₂ species). The formation of adsorbed molecular nitrogen is a relatively fast and facile step, with sticking coefficient of 0.7.²²⁹



After the formation of M-N₂ species, the subsequent step is the dissociation of N-N triple bond and the formation of adsorbed atomic nitrogen species. This step happens in a much slower rate where the sticking coefficient is in an order of magnitude of 10⁻⁷.²²⁹ Similar mechanism is proposed by Zeinalipour-Yazdi and co-workers on Co₃Mo₃N for ammonia synthesis. The combination of Co and Mo is similar to that of Ni and Fe, in that one component (Mo and Fe) strongly binds to nitrogen while the other (Co and Ni) weakly binds. They proposed both dissociative (Langmuir-Hinshelwood) and associative (Eley-Rideal/Mars-van Krevelen) mechanisms based on the DFT calculations.²³⁰ In dissociative mechanism, both Co and Mo are involved in some elementary steps. Meanwhile, only Mo is involved in associative mechanism. In the case of NiFeP nanoparticle, it is believed to be carried out in dissociative mechanism since the incorporation of Fe is far less than portion of Mo in Co₃Mo₃N. Therefore, the dissociation of N-N triple bond occurs after nitrogen adsorption, forming M-N intermediate.

The subsequent steps in ammonia synthesis are three sequential hydrogen additions on the adsorbed nitrogen atom. The most difficult step among the three is the first hydrogen addition which has the largest activation energy. Under conditions for catalysis carried in this chapter, adequate energy is provided by elevated temperature to overcome high energy barrier. Therefore, these consecutive hydrogen additions can proceed in a fast rate compared to the formation of adsorbed nitrogen atoms.



After consecutive hydrogen addition, adsorbed ammonia is formed and subsequently desorbed from the catalyst surface and released to complete the whole synthesis process.



5.4 Conclusion

Iron-doped nickel phosphide nanoparticle is successfully employed as catalyst in catalytic ammonia synthesis. To facilitate sustainable ammonia production, barium is added as promoter to provide electron density and structural support to iron-doped nickel phosphide nanoparticle. In addition, barium promoter prevents formation of excess adsorbed hydrogen which may inhibit production of ammonia. This can be revealed by conducting experiment without addition of barium promoter. Barium-promoted iron-doped nickel phosphide nanoparticle offers an ammonia production rate of $7.35 \text{ mmol h}^{-1} \text{ g}^{-1}$.

Mechanism for ammonia synthesis on iron-doped nickel phosphide nanoparticle is proposed. The production of ammonia goes through four steps: (1) adsorption of nitrogen on catalyst surface, (2) cleavage of N-N triple bond and H-H bonds and formation of adsorbed nitrogen and hydrogen species, (3) subsequent hydrogen addition on nitrogen, and (4) release of adsorbed ammonia as product.

Chapter 6 Conclusion

6.1 Conclusion

Nickel phosphide nanoparticles have drawn much attention among researchers due to their versatile reactivity on different catalytic reactions. Especially, their robust physical and chemical properties extend the use in various industrial applications. From conventional industrial applications on hydroprocessing in oil refinery industry, nickel phosphide nanoparticles are nowadays employed as catalysts for both hydrogen evolution reaction and oxygen evolution reactions through electrochemical or photochemical pathways. With the preliminary studies on successful employment of nickel phosphide-based catalysts on various catalytic reactions, further improvements have been made to achieve higher activity.

In this dissertation, the studies on preparation of nickel phosphide nanoparticles doped with various transition metals are presented. The prepared catalysts were thereby employed as catalysts in three important energy conversion reactions; electro- and photochemical hydrogen evolution reactions, electrochemical oxygen evolution reaction, and ammonia synthesis.

Metal doping in nickel phosphide nanoparticle was successfully carried out with different metals including Co, Fe, Mn, and Mo. Analysis on their

crystal structure, morphology, and bonding environments were conducted and presented in Chapter 2. The crystal structure and morphology of nickel phosphide nanoparticles do not alter extensively upon metal doping. NiMP nanoparticles retained the hexagonal crystal structure and spherical shape as Ni₂P nanoparticle. Detailed studies were done to elucidate oxidation state and local structure on the NiMP nanoparticles' surface using XPS and EXAFS measurement.

In Chapter 3, NiMP nanoparticles were employed as a catalyst in electrochemical and photochemical HER. NiMoP nanoparticle was determined as the best HER electro- and photocatalyst among all the samples prepared. The overpotential required to reach 10 mA cm⁻² in alkaline medium was 0.34 V vs. RHE. Tafel slope and exchange current density of NiMoP nanoparticle were estimated as 163 mV dec⁻¹ and 0.08 mA cm⁻², respectively. NiMoP nanoparticle was also active in dye-sensitized photocatalytic HER. In the presence of Ru(bpy)₃²⁺ and triethanolamine as photosensitizer and sacrificial agent, respectively, NiMoP nanoparticle yielded a high hydrogen production rate of 268 mmol h⁻¹ g⁻¹.

The OER is a complementary reaction to HER for completing overall water splitting. In Chapter 4, the reactivity of NiMP nanoparticles towards the

electrochemical OER was demonstrated. NiFeP nanoparticle was determined as the best OER electrocatalyst. The overpotential require to reach a current density of 20 mA cm^{-2} and Tafel slope were estimated to be 0.33 V vs. RHE and 39 mV dec^{-1} , respectively. The high activity in electrochemical OER is attributed to the iron doping that induced partial charge transfer.

Chapter 5 presents the application of NiFeP nanoparticle as a catalyst for ammonia synthesis. With barium promoter, NiFeP nanoparticle was shown to be an active catalyst for ammonia synthesis. The presence of Ba promoter was critical to make NiFeP nanoparticle active for continuous production of ammonia at the rate of $7.4 \text{ } \mu\text{mol mmol h}^{-1} \text{ g}^{-1}$.

6.2 Future Research Directions

Nickel phosphide nanoparticles doped with various metals have been successfully prepared and demonstrated their promising and diverse catalytic properties on energy conversion reactions, including hydrogen and oxygen evolution reactions, and ammonia synthesis. In photocatalytic hydrogen evolution reaction, a dye-sensitized system is employed with the assist of inorganic and organic dye. Both types of dyes undergo a photo-bleaching process and eventually decompose, which make them not applicable for long duration. To maximize the catalytic ability of metal-doped nickel phosphide nanoparticles in photocatalytic HER, a stable and efficient light-absorbing material is needed to activate and provide electrons to the catalytic sites in a sustainable manner. In addition, anchoring dye molecules on the catalyst surface is another possible way to enhance the catalytic performance. This would shorten the distance of electron transfer between dye and catalyst, thereby increasing the chance of successful transfer of photo-generated electrons and eventually the catalytic performance.

NiMP nanoparticles offers an alternative pathway to catalyze the ammonia synthesis. However, the activity is still far from the practical level of conventional ammonia-producing catalysts. It is worthwhile finding the

optimal support, both electronic and structural, to assist ammonia production.

In addition, it is important to elucidate the kinetic parameters and mechanism in ammonia synthesis which would help designing and improving the ammonia production catalysis. To obtain such information, theoretical calculation using density functional theory (DFT) can be used to predict the reaction pathway and guide the catalyst design.

References

1. *International Energy Outlook 2016*; U.S. Energy Information Administration: 2016.
2. Kudo, A.; Miseki, Y., Heterogeneous Photocatalyst Materials for Water Splitting. *Chemical Society Reviews* **2009**, *38* (1), 253-278.
3. Bell, A. T., The Impact of Nanoscience on Heterogeneous Catalysis. *Science* **2003**, *299* (5613), 1688.
4. Chaubey, R.; Sahu, S.; James, O. O.; Maity, S., A Review on Development of Industrial Processes and Emerging Techniques for Production of Hydrogen from Renewable and Sustainable Sources. *Renewable and Sustainable Energy Reviews* **2013**, *23*, 443-462.
5. Zheng, Y.; Jiao, Y.; Jaroniec, M.; Qiao, S. Z., Advancing the Electrochemistry of the Hydrogen-Evolution Reaction through Combining Experiment and Theory. *Angewandte Chemie International Edition* **2015**, *54* (1), 52-65.
6. Fletcher, S., Tafel Slopes from First Principles. *Journal of Solid State Electrochemistry* **2009**, *13* (4), 537-549.
7. Li, Y.; Wang, H.; Xie, L.; Liang, Y.; Hong, G.; Dai, H., MoS₂ Nanoparticles Grown on Graphene: An Advanced Catalyst for the Hydrogen Evolution Reaction. *Journal of the American Chemical Society* **2011**, *133* (19), 7296-7299.
8. Trasatti, S., Work Function, Electronegativity, and Electrochemical Behavior of Metals: III. Electrolytic Hydrogen Evolution in Acid Solutions. *Journal of Electroanalytical Chemistry and Interfacial Electrochemistry* **1972**, *39* (1), 163-184.
9. Nørskov, J. K.; Bligaard, T.; Logadottir, A.; Kitchin, J. R.; Chen, J. G.; Pandelov, S.; Stimming, U., Trends in the Exchange Current for Hydrogen Evolution. *Journal of The Electrochemical Society* **2005**, *152* (3), J23-J26.
10. Medford, A. J.; Vojvodic, A.; Hummelshøj, J. S.; Voss, J.; Abild-Pedersen, F.; Studt, F.; Bligaard, T.; Nilsson, A.; Nørskov, J. K., From the Sabatier Principle to a Predictive Theory of Transition-metal Heterogeneous Catalysis. *Journal of Catalysis* **2015**, *328*, 36-42.
11. Greeley, J.; Jaramillo, T. F.; Bonde, J.; Chorkendorff, I.; Nørskov, J. K., Computational High-throughput Screening of Electrocatalytic Materials for Hydrogen Evolution. *Nature Materials* **2006**, *5*, 909-13.
12. Zeng, M.; Li, Y., Recent Advances in Heterogeneous Electrocatalysts for

- the Hydrogen Evolution Reaction. *Journal of Materials Chemistry A* **2015**, *3* (29), 14942-14962.
13. Raj, I. A.; Vasu, K. I., Transition Metal-based Hydrogen Electrodes in Alkaline Solution - Electrocatalysis on Nickel Based Binary Alloy Coatings. *Journal of Applied Electrochemistry* **1990**, *20* (1), 32-38.
 14. McKone, J. R.; Sadtler, B. F.; Werlang, C. A.; Lewis, N. S.; Gray, H. B., Ni-Mo Nanopowders for Efficient Electrochemical Hydrogen Evolution. *ACS Catalysis* **2013**, *3* (2), 166-169.
 15. Eijsbouts, S.; Heinerma, J. J. L.; Elzerman, H. J. W., MoS₂ Structures in High Activity Hydrotreating Catalysts. II. Evolution of the Active Phase During the Catalyst Life Cycle. Deactivation Model. *Applied Catalysis A: General* **1993**, *105* (1), 69-82.
 16. Payen, E.; Hubaut, R.; Kasztelan, S.; Poulet, O.; Grimblot, J., Morphology Study of MoS₂- and WS₂-Based Hydrotreating Catalysts by High-Resolution Electron Microscopy. *Journal of Catalysis* **1994**, *147* (1), 123-132.
 17. Vrinat, M.; Breyse, M.; Geantet, C.; Ramirez, J.; Massoth, F., Effect of MoS₂ Morphology on the HDS Activity of Hydrotreating Catalysts. *Catalysis Letters* **1994**, *26* (1-2), 25-35.
 18. Hinnemann, B.; Moses, P. G.; Bonde, J.; Jørgensen, K. P.; Nielsen, J. H.; Horch, S.; Chorkendorff, I.; Nørskov, J. K., Biomimetic Hydrogen Evolution: MoS₂ Nanoparticles as Catalyst for Hydrogen Evolution. *Journal of the American Chemical Society* **2005**, *127* (15), 5308-5309.
 19. Jaramillo, T. F.; Jørgensen, K. P.; Bonde, J.; Nielsen, J. H.; Horch, S.; Chorkendorff, I., Identification of Active Edge Sites for Electrochemical H₂ Evolution from MoS₂ Nanocatalysts. *Science* **2007**, *317* (5834), 100-102.
 20. Kibsgaard, J.; Chen, Z.; Reinecke, B. N.; Jaramillo, T. F., Engineering the Surface Structure of MoS₂ to Preferentially Expose Active Edge Sites for Electrocatalysis. *Nature Materials* **2012**, *11*, 963-969.
 21. Xie, J.; Zhang, H.; Li, S.; Wang, R.; Sun, X.; Zhou, M.; Zhou, J.; Lou, X. W.; Xie, Y., Defect-Rich MoS₂ Ultrathin Nanosheets with Additional Active Edge Sites for Enhanced Electrocatalytic Hydrogen Evolution. *Advanced Materials* **2013**, *25* (40), 5807-5813.
 22. Kong, D.; Wang, H.; Cha, J. J.; Pasta, M.; Koski, K. J.; Yao, J.; Cui, Y., Synthesis of MoS₂ and MoSe₂ Films with Vertically Aligned Layers. *Nano Letters* **2013**, *13* (3), 1341-1347.
 23. Bonde, J.; Moses, P. G.; Jaramillo, T. F.; Nørskov, J. K.; Chorkendorff,

- I., Hydrogen Evolution on Nano-particulate Transition Metal Sulfides. *Faraday Discussions* **2009**, *140*, 219-231.
24. Stinner, C.; Prins, R.; Weber, T., Binary and Ternary Transition-Metal Phosphides as HDN Catalysts. *Journal of Catalysis* **2001**, *202* (1), 187-194.
 25. Sawhill, S. J.; Phillips, D. C.; Bussell, M. E., Thiophene Hydrodesulfurization over Supported Nickel Phosphide Catalysts. *Journal of Catalysis* **2003**, *215* (2), 208-219.
 26. Sawhill, S. J.; Layman, K. A.; Van Wyk, D. R.; Engelhard, M. H.; Wang, C.; Bussell, M. E., Thiophene Hydrodesulfurization over Nickel Phosphide Catalysts: Effect of the Precursor Composition and Support. *Journal of Catalysis* **2005**, *231* (2), 300-313.
 27. Liu, P.; Rodriguez, J. A., Catalysts for Hydrogen Evolution from the [NiFe] Hydrogenase to the Ni₂P(001) Surface: The Importance of Ensemble Effect. *Journal of the American Chemical Society* **2005**, *127* (42), 14871-14878.
 28. Popczun, E. J.; McKone, J. R.; Read, C. G.; Biacchi, A. J.; Wiltrout, A. M.; Lewis, N. S.; Schaak, R. E., Nanostructured Nickel Phosphide as an Electrocatalyst for the Hydrogen Evolution Reaction. *Journal of the American Chemical Society* **2013**, *135* (25), 9267-9270.
 29. Carencu, S.; Portehault, D.; Boissière, C. d.; Mézailles, N.; Sanchez, C. m., Nanoscaled Metal Borides and Phosphides: Recent Developments and Perspectives. *Chemical Reviews* **2013**, *113* (10), 7981-8065.
 30. Shi, Y.; Zhang, B., Recent Advances in Transition Metal Phosphide Nanomaterials: Synthesis and Applications in Hydrogen Evolution Reaction. *Chemical Society Reviews* **2016**, *45* (6), 1529-41.
 31. Huang, Z.; Chen, Z.; Chen, Z.; Lv, C.; Meng, H.; Zhang, C., Ni₁₂P₅ Nanoparticles as an Efficient Catalyst for Hydrogen Generation via Electrolysis and Photoelectrolysis. *ACS Nano* **2014**, *8* (8), 8121-8129.
 32. Ledendecker, M.; Calderón, S. K.; Papp, C.; Steinruck, H.-P.; Antonietti, M.; Shalom, M., The Synthesis of Nanostructured Ni₅P₄ Films and their Use as a Non-Noble Bifunctional Electrocatalyst for Full Water Splitting. *Angewandte Chemie International Edition* **2015**, *54* (42), 12361-12365.
 33. Pan, Y.; Liu, Y.; Zhao, J.; Yang, K.; Liang, J.; Liu, D.; Hu, W.; Liu, D.; Liu, Y.; Liu, C., Monodispersed Nickel Phosphide Nanocrystals with Different Phases: Synthesis, Characterization and Electrocatalytic Properties for Hydrogen Evolution. *Journal of Materials Chemistry A* **2015**, *3* (4), 1656-1665.

34. Pan, Y.; Hu, W. H.; Liu, D. P.; Liu, Y. Q.; Liu, C. G., Carbon Nanotubes Decorated with Nickel Phosphide Nanoparticles as Efficient Nanohybrid Electrocatalysts for the Hydrogen Evolution Reaction. *Journal of Materials Chemistry A* **2015**, *3* (24), 13087-13094.
35. Bai, Y.; Zhang, H.; Li, X.; Liu, L.; Xu, H.; Qiu, H.; Wang, Y., Novel Peapod-like Ni₂P Nanoparticles with Improved Electrochemical Properties for Hydrogen Evolution and Lithium Storage. *Nanoscale* **2015**, *7* (4), 1446-1453.
36. Han, A.; Jin, S.; Chen, H. L.; Ji, H. X.; Sun, Z. J.; Du, P. W., A Robust Hydrogen Evolution Catalyst Based on Crystalline Nickel Phosphide Nanoflakes on Three-dimensional Graphene/nickel Foam: High Performance for Electrocatalytic Hydrogen Production from pH 0-14. *Journal of Materials Chemistry A* **2015**, *3* (5), 1941-1946.
37. Kibsgaard, J.; Tsai, C.; Chan, K.; Benck, J. D.; Norskov, J. K.; Abild-Pedersen, F.; Jaramillo, T. F., Designing an Improved Transition Metal Phosphide Catalyst for Hydrogen Evolution Using Experimental and Theoretical Trends. *Energy & Environmental Science* **2015**, *8* (10), 3022-3029.
38. Yu, J.; Li, Q.; Li, Y.; Xu, C.-Y.; Zhen, L.; Dravid, V. P.; Wu, J., Ternary Metal Phosphide with Triple-Layered Structure as a Low-Cost and Efficient Electrocatalyst for Bifunctional Water Splitting. *Advanced Functional Materials* **2016**, *26* (42), 7644-7651.
39. Zhang, R.; Wang, X.; Yu, S.; Wen, T.; Zhu, X.; Yang, F.; Sun, X.; Wang, X.; Hu, W., Ternary NiCo₂P_x Nanowires as pH-universal Electrocatalysts for Highly Efficient Hydrogen Evolution Reaction. *Advanced Materials* **2017**, *29* (9), 1605502.
40. Han, A.; Chen, H.; Zhang, H.; Sun, Z.; Du, P., Ternary Metal Phosphide Nanosheets as a Highly Efficient Electrocatalyst for Water Reduction to Hydrogen over a Wide pH Range from 0 to 14. *Journal of Materials Chemistry A* **2016**, *4* (26), 10195-10202.
41. Pei, Y.; Yang, Y.; Zhang, F.; Dong, P.; Baines, R.; Ge, Y.; Chu, H.; Ajayan, P. M.; Shen, J.; Ye, M., Controlled Electrodeposition Synthesis of Co–Ni–P Film as a Flexible and Inexpensive Electrode for Efficient Overall Water Splitting. *ACS Applied Materials & Interfaces* **2017**, *9* (37), 31887-31896.
42. Liang, Q.; Huang, K.; Wu, X.; Wang, X.; Ma, W.; Feng, S., Composition-Controlled Synthesis of Ni_{2-x}Co_xP Nanocrystals as Bifunctional Catalysts for Water Splitting. *RSC Advances* **2017**, *7* (13), 7906-7913.

43. Zhang, X.; Gu, W.; Wang, E., Wire-on-flake Heterostructured Ternary $\text{Co}_{0.5}\text{Ni}_{0.5}\text{P}/\text{CC}$: an Efficient Hydrogen Evolution Electrocatalyst. *Journal of Materials Chemistry A* **2017**, *5* (3), 982-987.
44. Tang, C.; Gan, L.; Zhang, R.; Lu, W.; Jiang, X.; Asiri, A. M.; Sun, X.; Wang, J.; Chen, L., Ternary $\text{Fe}_x\text{Co}_{1-x}\text{P}$ Nanowire Array as a Robust Hydrogen Evolution Reaction Electrocatalyst with Pt-like Activity: Experimental and Theoretical Insight. *Nano Letters* **2016**, *16* (10), 6617-6621.
45. Tan, Y.; Wang, H.; Liu, P.; Shen, Y.; Cheng, C.; Hirata, A.; Fujita, T.; Tang, Z.; Chen, M., Versatile Nanoporous Bimetallic Phosphides towards Electrochemical Water Splitting. *Energy & Environmental Science* **2016**, *9* (7), 2257-2261.
46. Xiao, C.; Zhang, B.; Li, D., Partial-sacrificial-template Synthesis of Fe/Ni Phosphides on Ni Foam: a Strongly Stabilized and Efficient Catalyst for Electrochemical Water Splitting. *Electrochimica Acta* **2017**, *242*, 260-267.
47. Xuan, C.; Wang, J.; Xia, W.; Peng, Z.; Wu, Z.; Lei, W.; Xia, K.; Xin, H. L.; Wang, D., Porous Structured Ni-Fe-P Nanocubes Derived from a Prussian Blue Analogue as an Electrocatalyst for Efficient Overall Water Splitting. *ACS Applied Materials & Interfaces* **2017**, *9* (31), 26134-26142.
48. Ahn, S. H.; Manthiram, A., Direct Growth of Ternary Ni-Fe-P Porous Nanorods onto Nickel Foam as a Highly Active, Robust Bi-functional Electrocatalyst for Overall Water Splitting. *Journal of Materials Chemistry A* **2017**, *5* (6), 2496-2503.
49. Huang, H.; Yu, C.; Zhao, C.; Han, X.; Yang, J.; Liu, Z.; Li, S.; Zhang, M.; Qiu, J., Iron-tuned Super Nickel Phosphide Microstructures with High Activity for Electrochemical Overall Water Splitting. *Nano Energy* **2017**, *34*, 472-480.
50. Leitner, A. P.; Schipper, D. E.; Chen, J.-H.; Colson, A. C.; Rusakova, I.; Rai, B. K.; Morosan, E.; Whitmire, K. H., Synthesis of Hexagonal FeMnP Thin Films from a Single-Source Molecular Precursor. *Chemistry – A European Journal* **2017**, *23* (23), 5565-5572.
51. Zhao, Z.; Schipper, D. E.; Leitner, A. P.; Thirumalai, H.; Chen, J.-H.; Xie, L.; Qin, F.; Alam, M. K.; Grabow, L. C.; Chen, S.; Wang, D.; Ren, Z.; Wang, Z.; Whitmire, K. H.; Bao, J., Bifunctional Metal Phosphide FeMnP Films from Single Source Metal Organic Chemical Vapor Deposition for Efficient Overall Water Splitting. *Nano Energy* **2017**, *39*, 444-453.

52. Zhang, Y.; Liu, Y.; Ma, M.; Ren, X.; Liu, Z.; Du, G.; Asiri, A. M.; Sun, X., A Mn-doped Ni₂P Nanosheet Array: an Efficient and Durable Hydrogen Evolution Reaction Electrocatalyst in Alkaline Media. *Chemical Communications* **2017**, *53* (80), 11048-11051.
53. Liu, T.; Ma, X.; Liu, D.; Hao, S.; Du, G.; Ma, Y.; Asiri, A. M.; Sun, X.; Chen, L., Mn Doping of CoP Nanosheets Array: An Efficient Electrocatalyst for Hydrogen Evolution Reaction with Enhanced Activity at All pH Values. *ACS Catalysis* **2017**, *7* (1), 98-102.
54. Zhang, X.; Gu, W.; Wang, E., Self-supported Ternary Co_{0.5}Mn_{0.5}P/Carbon Cloth (CC) as a High-performance Hydrogen Evolution Electrocatalyst. *Nano Research* **2017**, *10* (3), 1001-1009.
55. Du, H.; Zhang, X.; Tan, Q.; Kong, R.; Qu, F., A Cu₃P-CoP Hybrid Nanowire Array: a Superior Electrocatalyst for Acidic Hydrogen Evolution Reactions. *Chemical Communications* **2017**, *53* (88), 12012-12015.
56. Ma, Y.-Y.; Wu, C.-X.; Feng, X.-J.; Tan, H.-Q.; Yan, L.-K.; Liu, Y.; Kang, Z.-H.; Wang, E.-B.; Li, Y.-G., Highly Efficient Hydrogen Evolution from Seawater by a Low-cost and Stable CoMoP@C Electrocatalyst Superior to Pt/C. *Energy & Environmental Science* **2017**, *10* (3), 788-798.
57. Teng, Y.; Wang, X.-D.; Chen, H.-Y.; Liao, J.-F.; Li, W.-G.; Kuang, D.-B., Iron-assisted Engineering of Molybdenum Phosphide Nanowires on Carbon Cloth for Efficient Hydrogen Evolution in a Wide pH Range. *Journal of Materials Chemistry A* **2017**, *5* (43), 22790-22796.
58. Wang, X.-D.; Xu, Y.-F.; Rao, H.-S.; Xu, W.-J.; Chen, H.-Y.; Zhang, W.-X.; Kuang, D.-B.; Su, C.-Y., Novel Porous Molybdenum Tungsten Phosphide Hybrid Nanosheets on Carbon Cloth for Efficient Hydrogen Evolution. *Energy & Environmental Science* **2016**, *9* (4), 1468-1475.
59. Fujishima, A.; Honda, K., Electrochemical Photolysis of Water at a Semiconductor Electrode. *Nature* **1972**, *238* (5358), 37-38.
60. Matsumura, M.; Saho, Y.; Tsubomura, H., Photocatalytic Hydrogen Production from Solutions of Sulfite Using Platinized Cadmium Sulfide Powder. *The Journal of Physical Chemistry* **1983**, *87* (20), 3807-3808.
61. Reber, J. F.; Rusek, M., Photochemical Hydrogen Production with Platinized Suspensions of Cadmium Sulfide and Cadmium Zinc Sulfide Modified by Silver Sulfide. *The Journal of Physical Chemistry* **1986**, *90* (5), 824-834.
62. Koca, A.; Şahin, M., Photocatalytic Hydrogen Production by Direct Sun Light from Sulfide/sulfite Solution. *International Journal of Hydrogen*

- Energy* **2002**, *27* (4), 363-367.
63. Zhang, X.; Peng, T.; Song, S., Recent Advances in Dye-sensitized Semiconductor Systems for Photocatalytic Hydrogen Production. *Journal of Materials Chemistry A* **2016**, *4* (7), 2365-2402.
 64. Willkomm, J.; Orchard, K. L.; Reynal, A.; Pastor, E.; Durrant, J. R.; Reisner, E., Dye-sensitized Semiconductors Modified with Molecular Catalysts for Light-driven H₂ Production. *Chemical Society Reviews* **2016**, *45* (1), 9-23.
 65. Zong, X.; Na, Y.; Wen, F.; Ma, G.; Yang, J.; Wang, D.; Ma, Y.; Wang, M.; Sun, L.; Li, C., Visible Light Driven H₂ Production in Molecular Systems Employing Colloidal MoS₂ Nanoparticles as Catalyst. *Chemical Communications* **2009**, (30), 4536-4538.
 66. Zheng, J.; Zhang, H.; Dong, S.; Liu, Y.; Tai Nai, C.; Suk Shin, H.; Young Jeong, H.; Liu, B.; Ping Loh, K., High Yield Exfoliation of Two-dimensional Chalcogenides Using Sodium Naphthalenide. *Nature Communications* **2014**, *5*, 2995.
 67. Jia, T.; Li, M. M. J.; Ye, L.; Wiseman, S.; Liu, G.; Qu, J.; Nakagawa, K.; Tsang, S. C. E., The Remarkable Activity and Stability of a Dye-sensitized Single Molecular Layer MoS₂ Ensemble for Photocatalytic Hydrogen Production. *Chemical Communications* **2015**, *51* (70), 13496-13499.
 68. Cao, S.; Chen, Y.; Wang, C.-J.; He, P.; Fu, W.-F., Highly Efficient Photocatalytic Hydrogen Evolution by Nickel Phosphide Nanoparticles from Aqueous Solution. *Chemical Communications* **2014**, *50* (72), 10427-10429.
 69. Sun, Z.; Zheng, H.; Li, J.; Du, P., Extraordinarily Efficient Photocatalytic Hydrogen Evolution in Water Using Semiconductor Nanorods Integrated with Crystalline Ni₂P Cocatalysts. *Energy & Environmental Science* **2015**, *8* (9), 2668-2676.
 70. Zeng, D.; Ong, W.-J.; Zheng, H.; Wu, M.; Chen, Y.; Peng, D.-L.; Han, M.-Y., Ni₁₂P₅ Nanoparticles Embedded into Porous g-C₃N₄ Nanosheets as a Noble-metal-free Hetero-structure Photocatalyst for Efficient H₂ Production under Visible Light. *Journal of Materials Chemistry A* **2017**, *5* (31), 16171-16178.
 71. Wen, J.; Xie, J.; Shen, R.; Li, X.; Luo, X.; Zhang, H.; Zhang, A.; Bi, G., Markedly Enhanced Visible-light Photocatalytic H₂ Generation over g-C₃N₄ Nanosheets Decorated by Robust Nickel Phosphide (Ni₁₂P₅) Cocatalysts. *Dalton Transactions* **2017**, *46* (6), 1794-1802.

72. Indra, A.; Acharjya, A.; Menezes, P. W.; Merschjann, C.; Hollmann, D.; Schwarze, M.; Aktas, M.; Friedrich, A.; Lochbrunner, S.; Thomas, A.; Driess, M., Boosting Visible-Light-Driven Photocatalytic Hydrogen Evolution with an Integrated Nickel Phosphide–Carbon Nitride System. *Angewandte Chemie International Edition* **2017**, *56* (6), 1653-1657.
73. Zhao, H.; Sun, S.; Jiang, P.; Xu, Z. J., Graphitic C₃N₄ Modified by Ni₂P Cocatalyst: An Efficient, Robust and Low Cost Photocatalyst for Visible-light-driven H₂ Evolution from Water. *Chemical Engineering Journal* **2017**, *315*, 296-303.
74. Dong, Y.; Kong, L.; Jiang, P.; Wang, G.; Zhao, N.; Zhang, H.; Tang, B., A General Strategy To Fabricate Ni_xP as Highly Efficient Cocatalyst via Photoreduction Deposition for Hydrogen Evolution. *ACS Sustainable Chemistry & Engineering* **2017**, *5* (8), 6845-6853.
75. Sun, Z.; Zhu, M.; Fujitsuka, M.; Wang, A.; Shi, C.; Majima, T., Phase Effect of Ni_xP_y Hybridized with g-C₃N₄ for Photocatalytic Hydrogen Generation. *ACS Applied Materials & Interfaces* **2017**, *9* (36), 30583-30590.
76. Wang, W.; An, T.; Li, G.; Xia, D.; Zhao, H.; Yu, J. C.; Wong, P. K., Earth-abundant Ni₂P/g-C₃N₄ Lamellar Nanohybrids for Enhanced Photocatalytic Hydrogen Evolution and Bacterial Inactivation under Visible Light Irradiation. *Applied Catalysis B: Environmental* **2017**, *217*, 570-580.
77. Zeng, D.; Xu, W.; Ong, W.-J.; Xu, J.; Ren, H.; Chen, Y.; Zheng, H.; Peng, D.-L., Toward Noble-metal-free Visible-light-driven Photocatalytic Hydrogen Evolution: Monodisperse Sub-15 nm Ni₂P Nanoparticles Anchored on Porous g-C₃N₄ Nanosheets to Engineer 0D-2D Heterojunction Interfaces. *Applied Catalysis B: Environmental* **2018**, *221*, 47-55.
78. Wu, W.; Yue, X.; Wu, X.-Y.; Lu, C.-Z., Efficient Visible-light-induced Hydrogen Evolution from Water Splitting using a Nanocrystalline Nickel Phosphide Catalyst. *RSC Advances* **2016**, *6* (29), 24361-24365.
79. Suen, N.-T.; Hung, S.-F.; Quan, Q.; Zhang, N.; Xu, Y.-J.; Chen, H. M., Electrocatalysis for the Oxygen Evolution Reaction: Recent Development and Future Perspectives. *Chemical Society Reviews* **2017**, *46* (2), 337-365.
80. Frydendal, R.; Paoli, E. A.; Knudsen, B. P.; Wickman, B.; Malacrida, P.; Stephens, I. E. L.; Chorkendorff, I., Benchmarking the Stability of Oxygen Evolution Reaction Catalysts: The Importance of Monitoring

- Mass Losses. *ChemElectroChem* **2014**, *1* (12), 2075-2081.
81. Lee, Y.; Suntivich, J.; May, K. J.; Perry, E. E.; Shao-Horn, Y., Synthesis and Activities of Rutile IrO₂ and RuO₂ Nanoparticles for Oxygen Evolution in Acid and Alkaline Solutions. *The Journal of Physical Chemistry Letters* **2012**, *3* (3), 399-404.
 82. Bockris, J. O. M.; Otagawa, T., The Electrocatalysis of Oxygen Evolution on Perovskites. *Journal of The Electrochemical Society* **1984**, *131* (2), 290-302.
 83. Grimaud, A.; May, K. J.; Carlton, C. E.; Lee, Y.-L.; Risch, M.; Hong, W. T.; Zhou, J.; Shao-Horn, Y., Double Perovskites as a Family of Highly Active Catalysts for Oxygen Evolution in Alkaline Solution. *Nature Communications* **2013**, *4*, 2439.
 84. Lee, J. G.; Hwang, J.; Hwang, H. J.; Jeon, O. S.; Jang, J.; Kwon, O.; Lee, Y.; Han, B.; Shul, Y.-G., A New Family of Perovskite Catalysts for Oxygen-Evolution Reaction in Alkaline Media: BaNiO₃ and BaNi_{0.83}O_{2.5}. *Journal of the American Chemical Society* **2016**, *138* (10), 3541-3547.
 85. Nikolov, I.; Darkaoui, R.; Zhecheva, E.; Stoyanova, R.; Dimitrov, N.; Vitanov, T., Electrocatalytic Activity of Spinel Related Cobalties M_xCo_{3-x}O₄ (M = Li, Ni, Cu) in the Oxygen Evolution Reaction. *Journal of Electroanalytical Chemistry* **1997**, *429* (1-2), 157-168.
 86. Li, Y.; Hasin, P.; Wu, Y., Ni_xCo_{3-x}O₄ Nanowire Arrays for Electrocatalytic Oxygen Evolution. *Advanced Materials* **2010**, *22* (17), 1926-1929.
 87. Cheng, F.; Shen, J.; Peng, B.; Pan, Y.; Tao, Z.; Chen, J., Rapid Room-temperature Synthesis of Nanocrystalline Spinels as Oxygen Reduction and Evolution Electrocatalysts. *Nature Chemistry* **2011**, *3*, 79-84.
 88. Maiyalagan, T.; Jarvis, K. A.; Therese, S.; Ferreira, P. J.; Manthiram, A., Spinel-type Lithium Cobalt Oxide as a Bifunctional Electrocatalyst for the Oxygen Evolution and Oxygen Reduction Reactions. *Nature Communications* **2014**, *5*, 3949.
 89. Gong, M.; Li, Y.; Wang, H.; Liang, Y.; Wu, J. Z.; Zhou, J.; Wang, J.; Regier, T.; Wei, F.; Dai, H., An Advanced Ni-Fe Layered Double Hydroxide Electrocatalyst for Water Oxidation. *Journal of the American Chemical Society* **2013**, *135* (23), 8452-8455.
 90. Lu, Z.; Xu, W.; Zhu, W.; Yang, Q.; Lei, X.; Liu, J.; Li, Y.; Sun, X.; Duan, X., Three-dimensional NiFe Layered Double Hydroxide Film for High-efficiency Oxygen Evolution Reaction. *Chemical Communications* **2014**, *50* (49), 6479-6482.

91. Song, F.; Hu, X., Exfoliation of Layered Double Hydroxides for Enhanced Oxygen Evolution Catalysis. *Nature Communications* **2014**, *5*, 4477.
92. Song, F.; Hu, X., Ultrathin Cobalt–Manganese Layered Double Hydroxide is an Efficient Oxygen Evolution Catalyst. *Journal of the American Chemical Society* **2014**, *136* (47), 16481-16484.
93. Liang, H.; Meng, F.; Cabán-Acevedo, M.; Li, L.; Forticaux, A.; Xiu, L.; Wang, Z.; Jin, S., Hydrothermal Continuous Flow Synthesis and Exfoliation of NiCo Layered Double Hydroxide Nanosheets for Enhanced Oxygen Evolution Catalysis. *Nano Letters* **2015**, *15* (2), 1421-1427.
94. Liu, Q.; Jin, J.; Zhang, J., NiCo₂S₄@graphene as a Bifunctional Electrocatalyst for Oxygen Reduction and Evolution Reactions. *ACS Applied Materials & Interfaces* **2013**, *5* (11), 5002-5008.
95. Ganesan, P.; Prabu, M.; Sanetuntikul, J.; Shanmugam, S., Cobalt Sulfide Nanoparticles Grown on Nitrogen and Sulfur Codoped Graphene Oxide: An Efficient Electrocatalyst for Oxygen Reduction and Evolution Reactions. *ACS Catalysis* **2015**, *5* (6), 3625-3637.
96. Swesi, A. T.; Masud, J.; Nath, M., Nickel Selenide as a High-efficiency Catalyst for Oxygen Evolution Reaction. *Energy & Environmental Science* **2016**, *9* (5), 1771-1782.
97. Stern, L.-A.; Feng, L.; Song, F.; Hu, X., Ni₂P as a Janus Catalyst for Water Splitting: the Oxygen Evolution Activity of Ni₂P Nanoparticles. *Energy & Environmental Science* **2015**, *8* (8), 2347-2351.
98. Han, A.; Chen, H.; Sun, Z.; Xu, J.; Du, P., High Catalytic Activity for Water Oxidation Based on Nanostructured Nickel Phosphide Precursors. *Chemical Communications* **2015**, *51* (58), 11626-11629.
99. Yu, X.-Y.; Feng, Y.; Guan, B.; Lou, X. W.; Paik, U., Carbon Coated Porous Nickel Phosphides Nanoplates for Highly Efficient Oxygen Evolution Reaction. *Energy & Environmental Science* **2016**, *9* (4), 1246-1250.
100. Wang, C.; Jiang, J.; Ding, T.; Chen, G.; Xu, W.; Yang, Q., Monodisperse Ternary NiCoP Nanostructures as a Bifunctional Electrocatalyst for Both Hydrogen and Oxygen Evolution Reactions with Excellent Performance. *Advanced Materials Interfaces* **2016**, *3* (4), 1500454.
101. He, P.; Yu, X.-Y.; Lou, X. W., Carbon-Incorporated Nickel–Cobalt Mixed Metal Phosphide Nanoboxes with Enhanced Electrocatalytic Activity for Oxygen Evolution. *Angewandte Chemie* **2017**, *129* (14),

3955-3958.

102. Mendoza-Garcia, A.; Su, D.; Sun, S., Sea Urchin-like Cobalt-iron Phosphide as an Active Catalyst for Oxygen Evolution Reaction. *Nanoscale* **2016**, *8* (6), 3244-3247.
103. Li, D.; Baydoun, H.; Verani, C. N.; Brock, S. L., Efficient Water Oxidation Using CoMnP Nanoparticles. *Journal of the American Chemical Society* **2016**, *138* (12), 4006-4009.
104. Liu, H., Ammonia Synthesis Catalyst 100 years: Practice, Enlightenment and Challenge. *Chinese Journal of Catalysis* **2014**, *35* (10), 1619-1640.
105. van der Ham, C. J. M.; Koper, M. T. M.; Hetterscheid, D. G. H., Challenges in Reduction of Dinitrogen by Proton and Electron Transfer. *Chemical Society Reviews* **2014**, *43* (15), 5183-5191.
106. Ertl, G., Surface Science and Catalysis—Studies on the Mechanism of Ammonia Synthesis: The P. H. Emmett Award Address. *Catalysis Reviews - Science and Engineering* **1980**, *21* (2), 201-223.
107. Spencer, N. D.; Schoonmaker, R. C.; Somorjai, G. A., Iron Single Crystals as Ammonia Synthesis Catalysts: Effect of Surface Structure on Catalyst Activity. *Journal of Catalysis* **1982**, *74* (1), 129-135.
108. Bare, S. R.; Strongin, D. R.; Somorjai, G. A., Ammonia Synthesis over Iron Single-crystal Catalysts: the Effects of Alumina and Potassium. *The Journal of Physical Chemistry* **1986**, *90* (20), 4726-4729.
109. Strongin, D. R.; Somorjai, G. A., The Effects of Potassium on Ammonia Synthesis Over Iron Single-crystal Surfaces. *Journal of Catalysis* **1988**, *109* (1), 51-60.
110. Nørskov, J. K., Electronic Factors in Catalysis. *Progress in Surface Science* **1991**, *38* (2), 103-144.
111. Skúlason, E.; Bligaard, T.; Gudmundsdóttir, S.; Studt, F.; Rossmeisl, J.; Abild-Pedersen, F.; Vegge, T.; Jónsson, H.; Nørskov, J. K., A Theoretical Evaluation of Possible Transition Metal Electro-catalysts for N₂ Reduction. *Physical Chemistry Chemical Physics* **2012**, *14* (3), 1235-1245.
112. Yang, Z.; Guo, W.; Lin, J.; Liao, D., Supported Catalysts with Ru-M (M = Fe, Co, Ni, Mo) Bimetallic Active Centers for Ammonia Synthesis. *Chinese Journal of Catalysis* **2006**, *27* (5), 378-380.
113. Miyazaki, A.; Balint, I.; Aika, K.-i.; Nakano, Y., Preparation of Ru Nanoparticles Supported on γ -Al₂O₃ and Its Novel Catalytic Activity for Ammonia Synthesis. *Journal of Catalysis* **2001**, *204* (2), 364-371.
114. Aika, K.-i.; Hori, H.; Ozaki, A., Activation of Nitrogen by Alkali Metal

- Promoted Transition Metal I. Ammonia Synthesis over Ruthenium Promoted by Alkali Metal. *Journal of Catalysis* **1972**, 27 (3), 424-431.
115. Aika, K.-i., Role of Alkali Promoter in Ammonia Synthesis over Ruthenium Catalysts-Effect on Reaction Mechanism. *Catalysis Today* **2017**, 286, 14-20.
116. Mortensen, J. J.; Hansen, L. B.; Hammer, B.; Nørskov, J. K., Nitrogen Adsorption and Dissociation on Fe(111). *Journal of Catalysis* **1999**, 182 (2), 479-488.
117. Jacobsen, C. J. H., Novel Class of Ammonia Synthesis Catalysts. *Chemical Communications* **2000**, (12), 1057-1058.
118. Jacobsen, C. J. H.; Dahl, S.; Clausen, B. S.; Bahn, S.; Logadottir, A.; Nørskov, J. K., Catalyst Design by Interpolation in the Periodic Table: Bimetallic Ammonia Synthesis Catalysts. *Journal of the American Chemical Society* **2001**, 123 (34), 8404-8405.
119. Ryoichi, K.; Ken-ichi, A., Cobalt Molybdenum Bimetallic Nitride Catalysts for Ammonia Synthesis. *Chemistry Letters* **2000**, 29 (5), 514-515.
120. Tsuji, Y.; Kitano, M.; Kishida, K.; Sasase, M.; Yokoyama, T.; Hara, M.; Hosono, H., Ammonia Synthesis over Co-Mo Alloy Nanoparticle Catalyst Prepared via Sodium Naphthalenide-driven Reduction. *Chemical Communications* **2016**, 52 (100), 14369-14372.
121. Raróg-Pilecka, W.; Jedynak-Koczek, A.; Petryk, J.; Miśkiewicz, E.; Jodzis, S.; Kaszkur, Z.; Kowalczyk, Z., Carbon-supported Cobalt-iron Catalysts for Ammonia Synthesis. *Applied Catalysis A: General* **2006**, 300 (2), 181-185.
122. Brock, S. L.; Senevirathne, K., Recent Developments in Synthetic Approaches to Transition Metal Phosphide Nanoparticles for Magnetic and Catalytic Applications. *Journal of Solid State Chemistry* **2008**, 181(7), 1552-1559.
123. Xiao, P.; Chen, W.; Wang, X., A Review of Phosphide-Based Materials for Electrocatalytic Hydrogen Evolution. *Advanced Energy Materials* **2015**, 5(24), 1500985.
124. Henkes, A. E.; Vasquez, Y.; Schaak, R. E., Converting Metals into Phosphides: A General Strategy for the Synthesis of Metal Phosphide Nanocrystals. *Journal of the American Chemical Society* **2007**, 129 (7), 1896-1897.
125. Park, J.; Koo, B.; Yoon, K. Y.; Hwang, Y.; Kang, M.; Park, J.-G.; Hyeon, T., Generalized Synthesis of Metal Phosphide Nanorods via Thermal

- Decomposition of Continuously Delivered Metal–Phosphine Complexes Using a Syringe Pump. *Journal of the American Chemical Society* **2005**, *127* (23), 8433-8440.
126. Mandale, A. B.; Badrinarayanan, S.; Date, S. K.; Sinha, A. P. B., Photoelectron-Spectroscopic Study of Nickel, Manganese and Cobalt Selenides. *Journal of Electron Spectroscopy and Related Phenomena* **1984**, *33* (1), 61-72.
127. Li, J.; Chai, Y.; Liu, B.; Wu, Y.; Li, X.; Tang, Z.; Liu, Y.; Liu, C., The Catalytic Performance of Ni₂P/Al₂O₃ Catalyst in Comparison with Ni/Al₂O₃ Catalyst in Dehydrogenation of Cyclohexane. *Applied Catalysis A: General* **2014**, *469*, 434-441.
128. Zhao, Y.; Zhao, Y.; Feng, H.; Shen, J., Synthesis of Nickel Phosphide Nano-particles in a Eutectic Mixture for Hydrotreating Reactions. *Journal of Materials Chemistry* **2011**, *21* (22), 8137-8145.
129. Myers, C. E.; Franzen, H. F.; Anderegg, J. W., X-Ray Photoelectron-Spectra and Bonding in Transition-Metal Phosphides. *Inorganic Chemistry* **1985**, *24* (12), 1822-1824.
130. Yan, Y.; Xia, B. Y.; Ge, X.; Liu, Z.; Fisher, A.; Wang, X., A Flexible Electrode Based on Iron Phosphide Nanotubes for Overall Water Splitting. *Chemistry - A European Journal* **2015**, *21* (50), 18062-18067.
131. Masud, J.; Umapathi, S.; Ashokaan, N.; Nath, M., Iron Phosphide Nanoparticles as an Efficient Electrocatalyst for the OER in Alkaline Solution. *Journal of Materials Chemistry A* **2016**, *4* (25), 9750-9754.
132. Seo, H.-R.; Cho, K.-S.; Kim, S.-H.; Lee, Y.-K., Effects of a Phosphorus Precursor on Structure and Activity of Ni₂P/SiO₂ Hydrotreating Catalysts: EXAFS Studies. *Journal of the Korean Physical Society* **2010**, *56* (6), 2083-2087.
133. Yoon, K. Y.; Jang, Y.; Park, J.; Hwang, Y.; Koo, B.; Park, J.-G.; Hyeon, T., Synthesis of Uniform-sized Bimetallic Iron–nickel Phosphide Nanorods. *Journal of Solid State Chemistry* **2008**, *181* (7), 1609-1613.
134. Muthuswamy, E.; Kharel, P. R.; Lawes, G.; Brock, S. L., Control of Phase in Phosphide Nanoparticles Produced by Metal Nanoparticle Transformation: Fe₂P and FeP. *ACS Nano* **2009**, *3* (8), 2383-2393.
135. Muthuswamy, E.; Savithra, G. H. L.; Brock, S. L., Synthetic Levers Enabling Independent Control of Phase, Size, and Morphology in Nickel Phosphide Nanoparticles. *ACS Nano* **2011**, *5* (3), 2402-2411.
136. Hitihami-Mudiyanselage, A.; Senevirathne, K.; Brock, S. L., Bottom-Up Assembly of Ni₂P Nanoparticles into Three-Dimensional Architectures:

- An Alternative Mechanism for Phosphide Gelation. *Chemistry of Materials* **2014**, *26* (21), 6251-6256.
137. Liyanage, D. R.; Danforth, S. J.; Liu, Y.; Bussell, M. E.; Brock, S. L., Simultaneous Control of Composition, Size, and Morphology in Discrete Ni_{2-x}Co_xP Nanoparticles. *Chemistry of Materials* **2015**, *27* (12), 4349-4357.
 138. Li, D.; Senevirathne, K.; Aquilina, L.; Brock, S. L., Effect of Synthetic Levers on Nickel Phosphide Nanoparticle Formation: Ni₅P₄ and NiP₂. *Inorganic Chemistry* **2015**, *54* (16), 7968-7975.
 139. Hitihami-Mudiyanselage, A.; Arachchige, M. P.; Seda, T.; Lawes, G.; Brock, S. L., Synthesis and Characterization of Discrete Fe_xNi_{2-x}P Nanocrystals (0 < x < 2): Compositional Effects on Magnetic Properties. *Chemistry of Materials* **2015**, *27* (19), 6592-6600.
 140. Pradhan, B.; Kumar, G. S.; Dalui, A.; Khan, A. H.; Satpati, B.; Ji, Q.; Shrestha, L. K.; Ariga, K.; Acharya, S., Shape-controlled Cobalt Phosphide Nanoparticles as Volatile Organic Solvent Sensor. *Journal of Materials Chemistry C* **2016**, *4* (22), 4967-4977.
 141. Huang, Z.; Chen, Z.; Chen, Z.; Lv, C.; Humphrey, M. G.; Zhang, C., Cobalt Phosphide Nanorods as an Efficient Electrocatalyst for the Hydrogen Evolution Reaction. *Nano Energy* **2014**, *9*, 373-382.
 142. Phillips, D. C.; Sawhill, S. J.; Self, R.; Bussell, M. E., Synthesis, Characterization, and Hydrodesulfurization Properties of Silica-supported Molybdenum Phosphide Catalysts. *Journal of Catalysis* **2002**, *207* (2), 266-273.
 143. Xiao, P.; Sk, M. A.; Thia, L.; Ge, X.; Lim, R. J.; Wang, J.-Y.; Lim, K. H.; Wang, X., Molybdenum Phosphide as an Efficient Electrocatalyst for the Hydrogen Evolution Reaction. *Energy & Environmental Science* **2014**, *7* (8), 2624-2629.
 144. *Hydrogen Storage*; U.S. Department of Energy: 2017.
 145. Hydrogen Fact Sheet, *New York State Energy Research and Development Authority, New York*, 2005.
 146. Zeng, K.; Zhang, D., Recent Progress in Alkaline Water Electrolysis for Hydrogen Production and Applications. *Progress in Energy and Combustion Science* **2010**, *36* (3), 307-326.
 147. Turner, J.; Sverdrup, G.; Mann, M. K.; Maness, P.-C.; Kroposki, B.; Ghirardi, M.; Evans, R. J.; Blake, D., Renewable Hydrogen Production. *International Journal of Energy Research* **2008**, *32* (5), 379-407.
 148. Morales-Guio, C. G.; Stern, L. A.; Hu, X., Nanostructured Hydrotreating

- Catalysts for Electrochemical Hydrogen Evolution. *Chemical Society Reviews* **2014**, *43* (18), 6555-69.
149. Linsebigler, A. L.; Lu, G.; Yates, J. T., Photocatalysis on TiO₂ Surfaces: Principles, Mechanisms, and Selected Results. *Chemical Reviews* **1995**, *95* (3), 735-758.
150. Thompson, T. L.; Yates, J. T., Surface Science Studies of the Photoactivation of TiO₂ - New Photochemical Processes. *Chemical Reviews* **2006**, *106* (10), 4428-4453.
151. Kumar, S. G.; Devi, L. G., Review on Modified TiO₂ Photocatalysis under UV/Visible Light: Selected Results and Related Mechanisms on Interfacial Charge Carrier Transfer Dynamics. *The Journal of Physical Chemistry A* **2011**, *115* (46), 13211-13241.
152. Shen, Y.; Ren, X.; Qi, X.; Zhou, J.; Huang, Z.; Zhong, J., MoS₂ Nanosheet Loaded with TiO₂ Nanoparticles: An Efficient Electrocatalyst for Hydrogen Evolution Reaction. *Journal of The Electrochemical Society* **2016**, *163* (13), H1087-H1090.
153. Ding, Q.; Song, B.; Xu, P.; Jin, S., Efficient Electrocatalytic and Photoelectrochemical Hydrogen Generation Using MoS₂ and Related Compounds. *Chem* **2016**, *1* (5), 699-726.
154. Feng, J.-X.; Xu, H.; Dong, Y.-T.; Lu, X.-F.; Tong, Y.-X.; Li, G.-R., Efficient Hydrogen Evolution Electrocatalysis Using Cobalt Nanotubes Decorated with Titanium Dioxide Nanodots. *Angewandte Chemie International Edition* **2017**, *56* (11), 2960-2964.
155. Duonghong, D.; Borgarello, E.; Graetzel, M., Dynamics of Light-induced Water Cleavage in Colloidal Systems. *Journal of the American Chemical Society* **1981**, *103* (16), 4685-4690.
156. Sayama, K.; Arakawa, H., Effect of Carbonate Salt Addition on the Photocatalytic Decomposition of Liquid Water over Pt-TiO₂ Catalyst. *Journal of the Chemical Society, Faraday Transactions* **1997**, *93* (8), 1647-1654.
157. Merki, D.; Hu, X. L., Recent Developments of Molybdenum and Tungsten Sulfides as Hydrogen Evolution Catalysts. *Energy & Environmental Science* **2011**, *4* (10), 3878-3888.
158. Brown, D. E.; Mahmood, M. N.; Man, M. C. M.; Turner, A. K., Preparation and Characterization of Low Overvoltage Transition-Metal Alloy Electrocatalysts for Hydrogen Evolution in Alkaline-Solutions. *Electrochimica Acta* **1984**, *29* (11), 1551-1556.
159. Paseka, I., Evolution of Hydrogen and Its Sorption on Remarkable

- Active Amorphous Smooth Ni-P(X) Electrodes. *Electrochimica Acta* **1995**, *40* (11), 1633-1640.
160. Amara, P.; Volbeda, A.; Fontecilla-Camps, J. C.; Field, M. J., A Hybrid Density Functional Theory/Molecular Mechanics Study of Nickel–Iron Hydrogenase: Investigation of the Active Site Redox States. *Journal of the American Chemical Society* **1999**, *121* (18), 4468-4477.
161. Burchardt, T., Hydrogen evolution on NiP_x Alloys: the Influence of Sorbed Hydrogen. *International Journal of Hydrogen Energy* **2001**, *26* (11), 1193-1198.
162. Das, A.; Han, Z.; Brennessel, W. W.; Holland, P. L.; Eisenberg, R., Nickel Complexes for Robust Light-Driven and Electrocatalytic Hydrogen Production from Water. *ACS Catalysis* **2015**, *5* (3), 1397-1406.
163. Chen, X.; Shen, S.; Guo, L.; Mao, S. S., Semiconductor-based Photocatalytic Hydrogen Generation. *Chemical Reviews* **2010**, *110* (11), 6503-70.
164. Kershaw, S. V.; Susha, A. S.; Rogach, A. L., Narrow Bandgap Colloidal Metal Chalcogenide Quantum Dots: Synthetic Methods, Heterostructures, Assemblies, Electronic and Infrared Optical Properties. *Chemical Society Reviews* **2013**, *42* (7), 3033-3087.
165. Navarro-Flores, E.; Chong, Z.; Omanovic, S., Characterization of Ni, NiMo, NiW and NiFe Electroactive Coatings as Electrocatalysts for Hydrogen Evolution in an Acidic Medium. *Journal of Molecular Catalysis A: Chemical* **2005**, *226* (2), 179-197.
166. Lyu, F.; Bai, Y.; Wang, Q.; Wang, L.; Zhang, X.; Yin, Y., Phase-controllable Synthesis of Cobalt Hydroxide for Electrocatalytic Oxygen Evolution. *Dalton Transactions* **2017**, *46* (32), 10545-10548.
167. Luo, Z.; Yu, L.; Yang, F.; Zhao, Z.; Yu, B.; Lai, H.; Wong, K. H.; Ngai, S. M.; Zheng, W.; Chen, T., Ruthenium Polypyridyl Complexes as Inducer of ROS-mediated Apoptosis in Cancer Cells by Targeting Thioredoxin Reductase. *Metallomics* **2014**, *6* (8), 1480-1490.
168. Schalenbach, M.; Speck, F. D.; Ledendecker, M.; Kasian, O.; Goehl, D.; Mingers, A. M.; Breitbach, B.; Springer, H.; Cherevko, S.; Mayrhofer, K. J. J., Nickel-molybdenum alloy catalysts for the hydrogen evolution reaction: Activity and stability revised. *Electrochimica Acta* **2018**, *259*, 1154-1161.
169. Jaksic, M. M., Hypo–hyper-d-electronic Interactive Nature of Interionic Synergism in Catalysis and Electrocatalysis for Hydrogen Reactions. *International Journal of Hydrogen Energy* **2001**, *26* (6), 559-578.

170. Durst, J.; Siebel, A.; Simon, C.; Hasche, F.; Herranz, J.; Gasteiger, H. A., New Insights into the Electrochemical Hydrogen Oxidation and Evolution Reaction Mechanism. *Energy & Environmental Science* **2014**, *7* (7), 2255-2260.
171. Kiwi, J.; Grätzel, M., Hydrogen Evolution from Water Induced by Visible Light Mediated by Redox Catalysis. *Nature* **1979**, *281*, 657.
172. Brown, G. M.; Brunshwig, B. S.; Creutz, C.; Endicott, J. F.; Sutin, N., Homogeneous Catalysis of the Photoreduction of Water by Visible Light. Mediation by a Tris(2,2'-bipyridine)ruthenium(II)-cobalt(II) Macrocyclic System. *Journal of the American Chemical Society* **1979**, *101* (5), 1298-1300.
173. Hirano, K.; Suzuki, E.; Ishikawa, A.; Moroi, T.; Shiroishi, H.; Kaneko, M., Sensitization of TiO₂ Particles by Dyes to Achieve H₂ Evolution by Visible Light. *Journal of Photochemistry and Photobiology A: Chemistry* **2000**, *136* (3), 157-161.
174. Ozawa, H.; Haga, M.-a.; Sakai, K., A Photo-Hydrogen-Evolving Molecular Device Driving Visible-Light-Induced EDTA-Reduction of Water into Molecular Hydrogen. *Journal of the American Chemical Society* **2006**, *128* (15), 4926-4927.
175. Deponti, E.; Natali, M., Photocatalytic Hydrogen Evolution with Ruthenium Polypyridine Sensitizers: Unveiling the Key Factors to Improve Efficiencies. *Dalton Transactions* **2016**, *45* (22), 9136-9147.
176. Kalyanasundaram, K., Photophysics, Photochemistry and Solar-Energy Conversion with Tris(Bipyridyl)Ruthenium(II) and Its Analogs. *Coordination Chemistry Reviews* **1982**, *46*, 159-244.
177. Abe, R.; Hara, K.; Sayama, K.; Domen, K.; Arakawa, H., Steady Hydrogen Evolution from Water on Eosin Y-fixed TiO₂ Photocatalyst using a Silane-coupling Reagent under Visible Light Irradiation. *Journal of Photochemistry and Photobiology A: Chemistry* **2000**, *137* (1), 63-69.
178. Li, Y.; Xie, C.; Peng, S.; Lu, G.; Li, S., Eosin Y-sensitized Nitrogen-doped TiO₂ for Efficient Visible Light Photocatalytic Hydrogen Evolution. *Journal of Molecular Catalysis A: Chemical* **2008**, *282* (1), 117-123.
179. Jin, Z.; Zhang, X.; Li, Y.; Li, S.; Lu, G., 5.1% Apparent Quantum Efficiency for Stable Hydrogen Generation over Eosin-sensitized CuO/TiO₂ Photocatalyst under Visible Light Irradiation. *Catalysis Communications* **2007**, *8* (8), 1267-1273.
180. Sreethawong, T.; Junbua, C.; Chavadej, S., Photocatalytic H₂ Production

- from Water Splitting under Visible Light Irradiation using Eosin Y-sensitized Mesoporous-assembled Pt/TiO₂ Nanocrystal Photocatalyst. *Journal of Power Sources* **2009**, *190* (2), 513-524.
181. Maeda, K.; Kuriki, R.; Zhang, M.; Wang, X.; Ishitani, O., The Effect of the Pore-wall Structure of Carbon Nitride on Photocatalytic CO₂ Reduction under Visible Light. *Journal of Materials Chemistry A* **2014**, *2* (36), 15146-15151.
182. Caspar, J. V.; Meyer, T. J., Photochemistry of Tris(2,2'-bipyridine)ruthenium(2+) ion (Ru(bpy)₃²⁺). Solvent effects. *Journal of the American Chemical Society* **1983**, *105* (17), 5583-5590.
183. Shen, M.; Yan, Z.; Yang, L.; Du, P.; Zhang, J.; Xiang, B., MoS₂ nanosheet/TiO₂ Nanowire Hybrid Nanostructures for Enhanced Visible-light Photocatalytic Activities. *Chemical Communications* **2014**, *50* (97), 15447-15449.
184. Li, Z.; Wu, Y.; Lu, G., Highly Efficient Hydrogen Evolution over Co(OH)₂ Nanoparticles Modified g-C₃N₄ Co-sensitized by Eosin Y and Rose Bengal under Visible Light Irradiation. *Applied Catalysis B: Environmental* **2016**, *188*, 56-64.
185. Yin, M.; Wu, C.; Jia, F.; Wang, L.; Zheng, P.; Fan, Y., Efficient Photocatalytic Hydrogen Production over Eosin Y-sensitized MoS₂. *RSC Advances* **2016**, *6* (79), 75618-75625.
186. Liu, X.; Zhao, L.; Lai, H.; Wei, Y.; Yang, G.; Yin, S.; Yi, Z., Graphene Decorated MoS₂ for Eosin Y-sensitized Hydrogen Evolution from Water under Visible Light. *RSC Advances* **2017**, *7* (74), 46738-46744.
187. Tian, J.; Cheng, N.; Liu, Q.; Xing, W.; Sun, X., Cobalt Phosphide Nanowires: Efficient Nanostructures for Fluorescence Sensing of Biomolecules and Photocatalytic Evolution of Dihydrogen from Water under Visible Light. *Angewandte Chemie International Edition* **2015**, *54* (18), 5493-5497.
188. Tsai, C.; Chan, K.; Nørskov, J. K.; Abild-Pedersen, F., Theoretical Insights into the Hydrogen Evolution Activity of Layered Transition Metal Dichalcogenides. *Surface Science* **2015**, *640*, 133-140.
189. Fan, X.; Wang, S.; An, Y.; Lau, W., Catalytic Activity of MS₂ Monolayer for Electrochemical Hydrogen Evolution. *The Journal of Physical Chemistry C* **2016**, *120* (3), 1623-1632.
190. Chen, L.; Dong, X.; Wang, Y.; Xia, Y., Separating Hydrogen and Oxygen Evolution in Alkaline Water Electrolysis using Nickel Hydroxide. *Nature Communications* **2016**, *7*, 11741.

191. Cheng, Y.; Jiang, S. P., Advances in Electrocatalysts for Oxygen Evolution Reaction of Water Electrolysis-from Metal oxides to Carbon Nanotubes. *Progress in Natural Science: Materials International* **2015**, 25 (6), 545-553.
192. Sapountzi, F. M.; Gracia, J. M.; Weststrate, C. J.; Fredriksson, H. O. A.; Niemantsverdriet, J. W., Electrocatalysts for the Generation of Hydrogen, Oxygen and Synthesis gas. *Progress in Energy and Combustion Science* **2017**, 58, 1-35.
193. Gottesfeld, S.; Srinivasan, S., Electrochemical and Optical Studies of Thick Oxide Layers on Iridium and Their Electrocatalytic Activities for the Oxygen Evolution Reaction. *Journal of Electroanalytical Chemistry and Interfacial Electrochemistry* **1978**, 86 (1), 89-104.
194. Zhang, B. W.; Lui, Y. H.; Zhou, L.; Tang, X. H.; Hu, S., An Alkaline Electro-activated Fe-Ni Phosphide Nanoparticle-stack Array for High-performance Oxygen Evolution under Alkaline and Neutral Conditions. *Journal of Materials Chemistry A* **2017**, 5 (26), 13329-13335.
195. Louie, M. W.; Bell, A. T., An Investigation of Thin-Film Ni-Fe Oxide Catalysts for the Electrochemical Evolution of Oxygen. *Journal of the American Chemical Society* **2013**, 135 (33), 12329-12337.
196. Zhu, Y.-P.; Liu, Y.-P.; Ren, T.-Z.; Yuan, Z.-Y., Self-Supported Cobalt Phosphide Mesoporous Nanorod Arrays: A Flexible and Bifunctional Electrode for Highly Active Electrocatalytic Water Reduction and Oxidation. *Advanced Functional Materials* **2015**, 25 (47), 7337-7347.
197. Lu, X.; Zhao, C., Electrodeposition of Hierarchically Structured Three-dimensional Nickel-iron Electrodes for Efficient Oxygen Evolution at High Current Densities. *Nature Communications* **2015**, 6, 6616.
198. Davies, G., Some Aspects of the Chemistry of Manganese(III) in Aqueous Solution. *Coordination Chemistry Reviews* **1969**, 4 (2), 199-224.
199. Takashima, T.; Hashimoto, K.; Nakamura, R., Mechanisms of pH-Dependent Activity for Water Oxidation to Molecular Oxygen by MnO₂ Electrocatalysts. *Journal of the American Chemical Society* **2012**, 134 (3), 1519-1527.
200. Lyons, M. E. G.; Brandon, M. P., The Oxygen Evolution Reaction on Passive Oxide Covered Transition Metal Electrodes in Aqueous Alkaline Solution. Part 1-nickel. *International Journal of Electrochemical Science* **2008**, 3 (12), 1386-1424.
201. Doyle, R. L.; Godwin, I. J.; Brandon, M. P.; Lyons, M. E. G., Redox and

- Electrochemical Water Splitting Catalytic Properties of Hydrated Metal Oxide Modified Electrodes. *Physical Chemistry Chemical Physics* **2013**, *15* (33), 13737-13783.
202. Lyons, M. E. G.; Doyle, R. L.; Godwin, I.; O'Brien, M.; Russell, L., Hydrous Nickel Oxide: Redox Switching and the Oxygen Evolution Reaction in Aqueous Alkaline Solution. *Journal of The Electrochemical Society* **2012**, *159* (12), H932-H944.
203. Mellsoy, S. R.; Gardiner, A.; Marshall, A. T., Electrocatalytic Oxygen Evolution on Nickel Oxy-hydroxide Anodes: Improvement through Rejuvenation. *Electrochimica Acta* **2015**, *180*, 501-506.
204. Ryden, W. D.; Lawson, A. W.; Sartain, C. C., Temperature Dependence of the Resistivity of RuO₂ and IrO₂. *Physics Letters A* **1968**, *26* (5), 209-210.
205. Trotochaud, L.; Young, S. L.; Ranney, J. K.; Boettcher, S. W., Nickel–Iron Oxyhydroxide Oxygen-Evolution Electrocatalysts: The Role of Intentional and Incidental Iron Incorporation. *Journal of the American Chemical Society* **2014**, *136* (18), 6744-6753.
206. Bau, J. A.; Lubner, E. J.; Buriak, J. M., Oxygen Evolution Catalyzed by Nickel–Iron Oxide Nanocrystals with a Nonequilibrium Phase. *ACS Applied Materials & Interfaces* **2015**, *7* (35), 19755-19763.
207. Han, N.; Zhao, F.; Li, Y., Ultrathin Nickel-iron Layered Double Hydroxide Nanosheets Intercalated with Molybdate Anions for Electrocatalytic Water Oxidation. *Journal of Materials Chemistry A* **2015**, *3* (31), 16348-16353.
208. Qi, J.; Zhang, W.; Xiang, R.; Liu, K.; Wang, H.-Y.; Chen, M.; Han, Y.; Cao, R., Porous Nickel–Iron Oxide as a Highly Efficient Electrocatalyst for Oxygen Evolution Reaction. *Advanced Science* **2015**, *2* (10), 1500199-n/a.
209. Młynarek, G.; Paszkiewicz, M.; Radniecka, A., The effect of ferric ions on the behaviour of a nickelous hydroxide electrode. *Journal of Applied Electrochemistry* **1984**, *14* (2), 145-149.
210. Corrigan, D. A., The Catalysis of the Oxygen Evolution Reaction by Iron Impurities in Thin Film Nickel Oxide Electrodes. *Journal of The Electrochemical Society* **1987**, *134* (2), 377-384.
211. Miller, E. L.; Rocheleau, R. E., Electrochemical Behavior of Reactively Sputtered Iron-Doped Nickel Oxide. *Journal of The Electrochemical Society* **1997**, *144* (9), 3072-3077.
212. Li, X.; Walsh, F. C.; Pletcher, D., Nickel Based Electrocatalysts for

- Oxygen Evolution in High Current Density, Alkaline Water E. *Physical Chemistry Chemical Physics* **2011**, *13*, 1162-1167.
213. Cox, J. D.; Wagman, D. D.; Medvedev, V. A., *CODATA Key Values for Thermodynamics*, Hemisphere Publishing Corporation, New York, 1989.
214. Bates, M. K.; Jia, Q.; Doan, H.; Laing, W.; Mukerjee, S., Charge-Transfer Effects in Ni–Fe and Ni–Fe–Co Mixed-Metal Oxides for the Alkaline Oxygen Evolution Reaction. *ACS Catalysis* **2016**, *6* (1), 155-161.
215. Erisman, J. W.; Sutton, M. A.; Galloway, J.; Klimont, Z.; Winiwarter, W., How a Century of Ammonia Synthesis Changed the World. *Nature Geoscience* **2008**, *1*, 636.
216. Jennings, J. R., *Catalytic Ammonia Synthesis : Fundamentals and Practice*. New York : Plenum Press: New York, 1991.
217. Ertl, G.; Weiss, M.; Lee, S. B., The Role of Potassium in the Catalytic Synthesis of Ammonia. *Chemical Physics Letters* **1979**, *60* (3), 391-394.
218. Kowalczyk, Z.; Jodzis, S.; Raróg, W.; Zieliński, J.; Pielaszek, J., Effect of Potassium and Barium on the Stability of a Carbon-supported Ruthenium Catalyst for the Synthesis of Ammonia. *Applied Catalysis A: General* **1998**, *173* (2), 153-160.
219. Murata, S.; Aika, K.-i., Preparation and Characterization of Chlorine-Free Ruthenium Catalysts and the Promoter Effect in Ammonia Synthesis.: 1. An Alumina-Supported Ruthenium Catalyst. *Journal of Catalysis* **1992**, *136* (1), 110-117.
220. Kadowaki, Y.; Aika, K.-i., Promoter Effect of Sm₂O₃ on Ru/Al₂O₃ in Ammonia Synthesis. *Journal of Catalysis* **1996**, *161* (1), 178-185.
221. Larichev, Y. V.; Moroz, B. L.; Zaikovskii, V. I.; Yunusov, S. M.; Kalyuzhnaya, E. S.; Shur, V. B.; Bukhtiyarov, V. I., XPS and TEM Studies on the Role of the Support and Alkali Promoter in Ru/MgO and Ru–Cs⁺/MgO Catalysts for Ammonia Synthesis. *The Journal of Physical Chemistry C* **2007**, *111* (26), 9427-9436.
222. Saadatjou, N.; Jafari, A.; Sahebdehfar, S., Ruthenium Nanocatalysts for Ammonia Synthesis: A Review. *Chemical Engineering Communications* **2015**, *202* (4), 420-448.
223. Kojima, R.; Aika, K.-i., Cobalt Molybdenum Bimetallic Nitride Catalysts for Ammonia Synthesis: Part 1. Preparation and Characterization. *Applied Catalysis A: General* **2001**, *215* (1), 149-160.
224. Zeng, H. S.; Inazu, K.; Aika, K.-i., The Working State of the Barium Promoter in Ammonia Synthesis over an Active-Carbon-Supported

- Ruthenium Catalyst Using Barium Nitrate as the Promoter Precursor. *Journal of Catalysis* **2002**, *211* (1), 33-41.
225. Truskiewicz, E.; Raróg-Pilecka, W.; Schmidt-Szałowski, K.; Jodzis, S.; Wilczkowska, E.; Łomot, D.; Kaszkur, Z.; Karpiński, Z.; Kowalczyk, Z., Barium-promoted Ru/carbon Catalyst for Ammonia Synthesis: State of the System when Operating. *Journal of Catalysis* **2009**, *265* (2), 181-190.
226. Raróg-Pilecka, W.; Miśkiewicz, E.; Szmigiel, D.; Kowalczyk, Z., Structure Sensitivity of Ammonia Synthesis over Promoted Ruthenium Catalysts Supported on Graphitised Carbon. *Journal of Catalysis* **2005**, *231* (1), 11-19.
227. Kowalczyk, Z.; Krukowski, M.; Raróg-Pilecka, W.; Szmigiel, D.; Zielinski, J., Carbon-based Ruthenium Catalyst for Ammonia Synthesis: Role of the Barium and Caesium Promoters and Carbon Support. *Applied Catalysis A: General* **2003**, *248* (1), 67-73.
228. Li, Q.; Hu, X., First-principles Study of Ni₂P (0001) Surfaces. *Physical Review B: Condensed Matter and Materials Physics* **2006**, *74* (3), 035414/1-035414/5.
229. Schlögl, R.; Wagner, E.; Fetzer, T.; Wagner, J.; Nehb, W.; Adlkofer, J.; Pachaly, B.; Keim, W., Inorganic Reactions. In *Handbook of Heterogeneous Catalysis*, Wiley-VCH Verlag GmbH: 2008; pp 1697-1799.
230. Zeinalipour-Yazdi, C. D.; Hargreaves, J. S. J.; Catlow, C. R. A., Low-T Mechanisms of Ammonia Synthesis on Co₃Mo₃N. *The Journal of Physical Chemistry C* **2018**, *122* (11), 6078-6082.